Rational Design of Loss-of-Function Phospholamban Mutants to Tune SERCA Function

A DISSERTATION
SUBMITTED TO THE FACULTY OF THE GRADUATE SCHOOL
OF THE UNIVERSITY OF MINNESOTA
BY

Kim Ngoc Ha

IN PARTIAL FULFILLMENT OF THE REQUIREMENTS
FOR THE DEGREE OF
DOCTOR OF PHILOSOPHY

Gianluigi Veglia

April 2012

ACKNOWLEDGEMENTS

I want to acknowledge many people for helping me achieve this accomplishment, but first and foremost I want to especially thank my advisor, Gianluigi Veglia. His scientific creativity, fearlessness, and willingness to pursue difficult challenge continue to be an inspiration for me. From working with him, I really learned what it means to be a good scientist and also to believe in myself, even in the more difficult times. I am thankful to him that he has continued to always be supportive of me, and I am glad to have him as my advisor and as my friend.

I also want to thank all the members of the Veglia Lab, past and present for their unending support and friendship through all these years. It is our camaraderie and willingness to teach and learn from each other that has made doing research such a wonderful experience. I am lucky to have had the opportunity to work with such exceptional scientists. I'd like to especially thank Dr. Larry R. Masterson, Dr. Lei Shi, Emily Metcalfe, Martin Gustavsson, Dr. Nathaniel Traaseth, Dr. Raffaello Verardi, Dr. Alessandro Mascioni, Dr. Bethany Buck-Koehntop, Dr. Gopinath Tata, Kaustubh Mote, Frank Chao, Jonggul Kim, Dr. Vitaly Vostrikov, Dr. Atul Srivastava, Geoffrey Li, Naomi Walsh, and Hope Steinke.

I want to extend thanks to the members of the Thomas group for their collaboration. Their contribution to field has been critical to the work in this thesis: Dr. David D. Thomas, Dr. Christine B. Karim, Dr. Florentin Nitu, Dr. Razvan Cornea, Tyler Miller, Dr. Elizabeth Lockamy, Sarah Blakely, and Octavian Cornea.

I would like to also acknowledge Dr. Alessandro Cembran for his contribution to Chapter 4 of the thesis and helpful discussions. I also would like to thank Dr. Seth Robia for his collaboration on Chapter 5 and helpful discussions.

I am thankful for the support of the members of the Biochemistry, Molecular Biology, and Biophysics and Chemistry Department. I especially want to thank Dr. Kylie Walters for serving as the chair of my thesis committee and for her mentorship and constant support and encouragement, and also Dr. Edgar Arriaga for his support.

Lastly I want to thank my family and friends for their love and support during this long journey: my parents Minh Le Ha and Lung Van Ha; my siblings: Dr. Chau Ha, Dr. Martin Newcomb, Luan Ha, Tammy Ha, Phong Ha, Michele Ha, Thanh Ha, Sophia Ha, and Long Ha; Ruth and Joe Robelia; the Robelia family; WK; the Pogue-Brady family; the Remes-Riach family; Ela J. Rausch and my Radio K family, and Noah Harmon. Last, but not least, I want to thank Peter Robelia for his love and heroic efforts in keeping me sane through all these years.

DEDICATION

To my parents, Minh Le Ha and Lung Van Ha and my sister, Minh Chau Thi Ha. It is your strength and determination that inspire me every day to improve the world.

Abstract

Unphosphorylated phospholamban (PLN) is the endogenous inhibitor of the sarco(endo)plasmic reticulum Ca2+ ATPase (SERCA), the enzyme that regulates cardiac muscle relaxation in humans. In its phosphorylated state, PLN (pS16-PLN, pT17-PLN, and pS16pT17-PLN) does not inhibit SERCA. Dysfunctions in SERCA:PLN interactions and in the PLN phosphorylation mechanism have been implicated in cardiac disease and targeting PLN is becoming a viable avenue for treating heart disease. Specifically, innovative genetic treatments using recombinant adeno-associated virus (rAAV) with S16E-PLN, a pseudo-phosphorylated form of PLN, have shown a remarkable efficacy in reducing the progression of cardiac failure in both small and large animals. The following thesis summarizes efforts to rationally design PLN mutants to tune SERCA function. Using a combination of NMR spectroscopy and biochemical assays, we have built a structure-dynamics-function correlation that shows PLN can be tuned to augment SERCA function by acting on the conformational coupling between the cytoplasmic and transmembrane domain and by pseudo-phosphorylation. Additionally, to better understand the role of mutation in PLN:SERCA interactions, we also investigated a mutant of PLN (R9C) known to be linked to hereditary dilated cardiomyopathy, showing that the mutation disrupts the pentamer-monomer equilibrium, and that these effects are exacerbated under oxidizing conditions. Insights to these issues will provide better paradigms with which to design therapeutic mutants of PLN for treatment of heart failure.

CONTENTS

3 What Can We Learn From a Small Regulatory Membrane Protein?

LIST OF TABLES

LIST OF FIGURES

CHAPTER 1

CHAPTER 2

CHAPTER 3

CHAPTER 4

CHAPTER 5

CHAPTER 6

LIST OF ABBREVIATIONS

Carr-Purcell-Meiboom-Gill – CPMG

Chemical Shift Anisotropy – CSA

Dioleoyl-sn-Glycero-3-Phosphocholine – DOPC

Dioleoyl-sn-Glycero-3-Phosphoethanolamine – DOPE

Dipolar Coupling – DC

Dodecylphosphocholine – DPC

Loss-of-function – LOF (Note: loss of function in this thesis is defined as reduction of SERCA inhibition)

Gain-of-function – GOF (Note: gain of function in this thesis is defined as increase of SERCA inhibition)

Monomeric phospholamban – AFA-PLN

Nuclear magnetic resonance - NMR

Phospholamban – PLN

Sarco(endo)plasmic Reticulum Calcium ATPase – SERCA

Sarcolipin – SLN

Wild-type PLN – wt-PLN

Chapter 1

Background and Significance

Preface

1.1 Structural Biology of Membrane Proteins

Membrane proteins associate with biomembranes (1). The two main classes of membrane proteins are peripheral membrane proteins, those which are associated with the phospholipid bilayer, and integral membrane proteins, which have components thoroughly embedded in the bilayer. Although constituting 30% of the eukaryotic and prokaryotic genomes and 60% of drug targets, only ~1,000 of the over greater than 60,000 deposited structures in the PDB (Protein Data Bank) are classified as membrane proteins, and about 300 of those structures are unique membrane proteins or peptides. Despite the relatively small number of structures, membrane proteins are crucial to physiological function via cell signaling across lipid membranes, ion transport, and pore-channel formation(1) . Membrane proteins are also a major target for the pharmaceutical industry due to their critical roles in signal transduction and disease, so their structure determination has become a major scientific pursuit.

Membrane protein structure elucidation is an intriguing problem for scientists due to the challenges they present which stems mostly from their high level of hydrophobicity. Generally, for a protein to be amenable to structural studies, it needs to be soluble at high concentrations, monodisperse, conformationally homogeneous, and stable for time periods that allow for experimental measurements. These conditions are difficult to achieve for membrane proteins, particularly channels which are large in molecular weight (2). Sample preparation for membrane proteins is also complicated by the necessity of lipids or detergents to keep them soluble, a

difficulty for the conventional methods of x-ray crystallography and solution-state NMR (nuclear magnetic resonance) spectroscopy. High-resolution crystals for x-ray studies are very difficult to grow in the presences of lipids and detergents (3). Moreover, lipids and detergents decrease molecular tumbling in solution, which results in broad signals that are difficult to detect by NMR (2).

Advances in methodologies in the past two decades have made studying membrane proteins an exciting horizon in structural biology. The use of detergent micelles, novel lipid preparations, advances in hardware and pulse sequences, especially in the field of solid-state NMR, all make NMR spectroscopy amenable to tackle this difficult problem. Advances combining solution and solid state NMR spectroscopy are addressing these issues (4, 5, 6).

1.2 RELATIONSHIP BETWEEN STRUCTURAL DYNAMICS AND PROTEIN FUNCTION

The scope of structural biology is to investigate the relationship of protein structure to its function, and dynamics play a significant role in this scheme (7). Proteins are not static constructions, but rather very dynamic molecules that "undergo conformational changes while performing their specific functions, such as an enzyme reaction or ligand binding" (8). Local flexibility within a protein can be altered upon binding and promote changes in conformation and lead to allostery (8). Considering that the crux of most biological activity lies in intermolecular interactions, molecular motions are the means by which nature navigates protein function (9). Therefore, by understanding the structure and dynamics of a protein, it is possible to control its function by modifying the structural dynamics.

NMR is an elegant tool to study protein dynamics due to its ability to probe motions at various timescales (**Fig 1.1**) (10). Fluctuations in chemical bond vectors induce relaxation which affects the observable NMR signal, and give us detailed information about molecular motions. Fast protein dynamics (on the ps-ns timescale) are conventionally characterized by the order parameter, S^2, while slow protein dynamics (on the μs-ms timescale) are typically determined by $R_{1\rho}$ or Carr-Purcell-Meiboom-Gill (CPMG) type experiments (**Fig 1.1**) (10). Although chemical processes and protein interactions generally undergo changes on the slow timescale, fast dynamics often underlie these slower molecular motions (11).

Chapter 4 and 5 of this thesis aims to correlate the contribution of structural dynamics of mutants of a membrane protein inhibitor, phospholamban, to the function of its enzymatic target, SR Ca^{2+}-ATPase (SERCA). As a result of understanding how the structure and dynamics of

phospholamban leads to SERCA's function, the goal is to control the protein function of an enzyme by rationally altering the structural dynamics of its inhibitor. This type of approach is a novel innovation for studying membrane-embedded ion channels and introduces a new paradigm to controlling enzyme function, through "*tuning allosteric regulation*."

1.3 MOLECULAR PROFILE TO CARDIAC RELAXATION: SERCA & PHOSPHOLAMBAN

The primary driving force of cardiac contraction is the cyclic transport of Ca^{2+} through the cytosol of cardiac muscle cells by membrane proteins (12). The mechanism of contraction and relaxation by the cardiomyocyte is often referred as the "calcium induced calcium release" cycle. Contraction is initiated through extracellular Ca^{2+} transported into the cytosol through voltage-dependent L-type calcium channels, which increases the intracellular Ca^{2+} concentration. The increase in intracellular Ca^{2+} triggers the ryanodine receptors to begin releasing Ca^{2+} from its storehouse, the sarcoplasmic reticulum (SR). The influx of free Ca^{2+} in the cytosol can bind to myofilament protein troponin C, and the mechanism of contraction begins. For relaxation to occur, troponin C is phosphorylated and undergoes a conformational change in order release Ca^{2+}. After release from the myofilaments, Ca^{2+} is removed from the cytosol through the cell membrane by the sarcolemmal Na^{+}/Ca^{2+} exchanger and the sarcolemmal Ca^{2+}-ATPase, however the bulk (70%) of this Ca^{2+} is channeled back into the SR by the sarco(endo)plasmic reticulum Ca^{2+}-ATPase (SERCA) (12).

SERCA is a 110 kDa membrane-imbedded enzyme composed of a nucleotide binding domain, a phosphorylation domain, an actuator domain, and a transmembrane domain comprised of 10 transmembrane helices which serves as the calcium channel (**Fig 1.2**). SERCA is driven by ATP hydrolysis, transporting 2 Ca^{2+} ions for every ATP molecule converted to ADP. SERCA is mediated by two endogenous transmembrane protein inhibitors: phospholamban (PLN) (13), which is 52 amino acids in length, and sarcolipin (SLN) which is 31 amino acids in length (**Fig 1.3**) (14). While SLN is mostly expressed in skeletal muscle, PLN is located in cardiac myocytes. SLN and the transmembrane domain of PLN share much sequential and structural homology (15). PLN's inhibitory power is dictated by its phosphorylation state. PLN has two primary phosphorylation sites: serine 16, by cAMP-dependent protein kinase A (PKA), and threonine 17, by calmodulin/Ca^{2+}-dependent protein kinase II (CamKII) (16). SLN is predicted to have a CamKII phosphorylation site at threonine 5 (17). The mechanism for phosphorylation is stimulated by the β-adrenergic cascade, which leads to increased contractility of cardiac myocytes, and physiologically activates cardiac contraction and relaxation rates by relieving

PLN inhibition of SERCA. Phosphorylation of PLN at Ser 16 leads to several structural and dynamic transitions, which will be further elaborated in Chapter 2 and 3.

SERCA is regulated by PLN and SLN by an allosteric mechanism involving the transition between energetic states. PLN is stored in a pentameric reservoir, and the active monomer de-oligomerizes to bind and inhibit SERCA (18, 19). The PLN monomer exchanges between four different conformational states (20, 21, 22) with the most stable ground (T) state arranged in an L-shaped topology (5) with the amphipathic domain Ia helix absorbed on the surface of the bilayer, and the most excited R-state membrane detached and unfolded (20, 23). The excited R-state has been shown to be the state preferably selected both by SERCA and PKA (23, 24). Additionally, promotion of the R-state is able to tune SERCA function (20, 23, 25).

Cardiac disease and heart failure are the leading cause of mortality and morbidity in developed nations (26), with the last treatment for cardiomyopathy-related heart failure available being heart transplantation. The intracellular handling of Ca^{2+} is a major component of proper muscle contraction and relaxation, so dysfunctions in SERCA and PLN interactions in particular have been implicated as having a role in cardiac disease (27). Naturally occurring mutations in PLN which have been discovered and found to be related to familial forms of cardiomyopathy include: R9C (28), R9L and R9H (29), R14del (30), and L39stop (31).

The pathway to innovating genetic treatments to dysfunctions of PLN:SERCA interactions has recently become a new interest in the field, particularly since the success of S16E, a pseudo-phosphorylated form of PLN which was introduced to mice with a cardiomyopathy phenotype via recombinant adeno-associated virus gene therapy, effectively reduced the progression of the cardiac failure (32). This approach has recently been introduced into large animal models with success (33). The work on mutations of PLN performed by MacLennan's group offered invaluable insight to functionally relevant areas of PLN and identified residues crucial to PLN's inhibitory power(34), but the mutation studies often did not identify the contribution of structural dynamics or binding surface to the functional effect of the mutation. There have also been attempts at rationally designing inhibitors to SERCA based on mutation data collected over the past 15 years, however results from these studies have not yielded very promising targets for development into animal models (35).

To date, the Protein Data Bank yields 11 structures of PLN. The genesis of PLN structures spans from early structures that only included single domains solved in organic solvents (36) to structures of the entire PLN pentamer in detergent and lipid preparations (6, 37). The quality and physiological relevance for the structures of PLN has advanced and has now opened up to an era

where we can begin to image the SERCA:PLN complex in native SR lipid preparations. Much of our new structural developments have been due to biophysical characterization of the SERCA:PLN complex (38, 39, 40) and the hybrid solution and solid-state NMR structure determination method pioneered by the Veglia Lab (4, 5, 6). These types of studies (41) have made immense contributions to our understanding of PLN in its different inhibitory states, and in the absence and in the presence of SERCA. Further advances in solid-state and solution-state NMR technologies continue, and will facilitate the search for answers to the structure and function of PLN. In this respect, the current state of the field will be reviewed in Chapters 2 and 3.

1.4 REVEALING MEMBRANE PROTEIN STRUCTURE, DYNAMICS, AND PROTEIN-PROTEIN INTERACTIONS BY NUCLEAR MAGNETIC RESONANCE SPECTROSCOPY

Membrane proteins provide a significant challenge to structural biologists for a number of reasons. Primarily, sample preparation makes it difficult to crystallize membrane proteins, and the significance of topology for membrane protein function leads to many solution methods, which measure an average structure tumbling isotropically in solution, making it difficult to analyze in the context of protein function. Much information can still be garnered from solution state NMR techniques, such as structure determination, elucidation of structural dynamics, and most intriguingly, the ability to probe protein-protein interactions at atomic resolution. Paired with other techniques which give us information regarding the function of the protein, NMR becomes an extremely powerful tool for protein science.

In Chapter 4 and Chapter 6, several single-residue and multi-residue mutants of PLN were studied by NMR to determine secondary structural elements through H_α chemical shifts, probe fast backbone dynamics by heteronuclear NOE experiments, and characterize the protein-protein interactions between PLN and SERCA.

1.4.1 Chemical Shift Index as a Secondary Structure Probe

The chemical shift has long been recognized as a sensitive measure of electronic environment, and thus molecular conformation and composition (42, 43). The chemical shift index (CSI) is a useful measure to determine secondary structural elements of proteins (44). Empirically, the chemical shift can be described as

$$\nu_i(Hz) = \gamma B_0 (1-\sigma_i)/2\pi \qquad [1]$$

where σ_i is the shielding constant, which is dependent on electronic structure. The H_α CSI is taken as the difference of the H_α chemical shifts of the protein of interest and that of random coil values (45). A pattern of upfield shifts is indicative of an alpha-helical secondary structure, while a downfield shift is indicative of a beta-sheet conformation. Randomized upfield and downfield shifts are representative of a random coil. The H_α CSI is a particularly good probe of conformation since it is less likely to be affected by experimental perturbations such pH and temperature.

For these studies, a pair of three-dimensional experiments was used: a ^{15}N-edited total correlation spectroscopy (^{15}N TOCSY-HSQC), which measures through-bond correlations, and a ^{15}N-edited NOE spectroscopy (^{15}N NOESY-HSQC), which measures through-space correlations (46, 47, 48, 49, 50, 51). H_α chemical shifts were obtained by using these experiments to assign the ^1H and ^{15}N resonances for each PLN mutant. Resonance assignments were then transferred to the two-dimensional ^{15}N heteronuclear single-quantum correlation (HSQC) spectra (48) for each of the PLN species. This pair of three-dimensional experiments was complementary. Although the TOCSY experiments are useful for side-chain and backbone chemical shift assignments and identification of the type of amino acid present in the spin system, they are highly sensitive to transverse relaxation (T_2). This becomes an issue when dealing with membrane proteins embedded in large, slowly-tumbling, micelles (52). However, ^{15}N TOCSY-HSQC experiments are useful in combination with NOESY experiments, which in addition to not being as sensitive to transverse relaxation also show inter-residue correlations. While the ^{15}N TOCSY-HSQC identifies the amino acid type of residue, the ^{15}N NOESY-HSQC facilitates sequential resonance assignment, making it possible to fully assign the ^{15}N HSQC fingerprints and H_α chemical shifts for the mutant PLN species studied (44, 53).

The three-dimensional ^{15}N TOCSY-HSQC pulse sequence used in these studies correlates the ^1H-^1H TOCSY plane with the ^{15}N shifts to form a ^1H-^{15}N HSQC dimension (**Fig 1.4**). The detection of TOCSY type correlations is achieved through a “spin lock” mixing period where the Hartmann-Hahn condition (54) is met. During this mixing period, magnetization can be exchanged between the amide proton and those of the H_α and side-chain protons within the same spin-system. The Hartmann-Hahn condition is described as

$$\gamma_1 B_1 = \gamma_2 B_2 \qquad [2]$$

Where γ describes the gyromagnetic ratio and B is the local magnetic field (55). This type of magnetization transfer is often referred to as homonuclear cross-polarization (56) (**Fig 1.5**). A mixing time of 70 ms was found to be optimal to detect the cross-peak intensities of the aliphatic protons for the range of residues in the samples studied (52) (**Fig 1.6**).

The ^{15}N-edited 3D NOESY-HSQC pulse sequence (**Fig 1.7**) was utilized along with the TOCSY spectra by identifying residues in proximity with one another. Typically these types of experiments are used for structure calculations since they measure through space dipole-dipole interactions and the mixing times (τ_M) are set to lengths of 150-200 ms to allow for the buildup of (*i, i+4*) NOEs crosspeaks. However, considering the structure of PLN-AFA in DPC micelles was already determined in 2003 (57) and the main focus was not to use the correlations for structure determination, but rather to use the NOESY-HSQC to identify inter-residue correlations, the experiment was optimized to with a short τ_M (70 ms) in order to observe sequential NOEs. However, through-space NOEs are still observed. The resulting spectra are similar to that of the ^{15}N TOCSY-HSQC, but with the added presence of i+1 NOEs to facilitate resonance assignment (**Fig 1.9**).

1.4.2 Fast (ps-ns) Backbone Dynamics Elucidated by NOE Enhancement

The Nuclear Overhauser Effect (NOE) (58) is extremely useful in protein structure determination and dynamics characterization for solution-state NMR. In solution state NMR, the NOEs provide invaluable information of through-space distance constraints. {^{1}H}-^{15}N steady-state NOE enhancement can also be used as a measure of the fast internal motions on the ps-ns timescale. The enhancement is an increase in the NMR signal due to a population inversion between the excited and ground states, and a result of the cross relaxation induced by the dipolar coupling of two spins in proximity to one another(59). The NOE is dependent on the strength of the dipolar coupling between two nuclei. The Hamiltonian for the dipolar coupling for two spin-½ nuclei is described as

$$H_{DC} = \frac{\hbar \gamma_I \gamma_S}{4\pi r^3} [1 - 3\cos^2\theta] \ (3I_z S_z - I \cdot S) \qquad [3]$$

The angular dependence of the dipolar coupling is averaged to zero in the isotropic case, however the non-secular terms of the dipolar coupling are not angular dependent, and contribute to cross relaxation pathways, giving rise to the NOE (60). It is also important to note that in solution, the isotropic tumbling averages the dipolar coupling so that the distance dependence becomes r^{-6} (60). The phenomenon of the NOE enhancement is best described by the derivation of the Solomon Equations (61).

When considering two spins, I_z and S_z, the energy level diagram can be described as in **Fig 1.10**. Six different transitions are possible for the spin pair, and their probabilities represented by the symbol W. The single-quantum transitions are observed in NMR, in particular with the HSQC experiment. The "forbidden" multiple quantum transitions (W_2^{IS} and W_0^{IS}) are responsible for the evolution of the NOE and are those which contribute to cross-relaxation.

One can consider W as a representation of how effective the transition pathway is, thus, it should also be a measure of the population of the levels. The net magnetization of each spin I_z and S_z can be given by summing the differences between the energy levels.

$$I_z=N_{\alpha\alpha} - N_{\beta\alpha} + N_{\alpha\beta} - N_{\beta\beta} \quad [4]$$

$$S_z = N_{\alpha\alpha} + N_{\beta\alpha} - N_{\alpha\beta} - N_{\beta\beta} \quad [5]$$

Where N_i represents the population of spins in each energy state. The rate of change over time for each spin is described as

$$dI_z/dt = dN_{\alpha\alpha}/dt - dN_{\beta\alpha}/dt + dN_{\alpha\beta}/dt - dN_{\beta\beta}/dt \quad [6]$$

$$dS_z/dt = dN_{\alpha\alpha}/dt + dN_{\beta\alpha}/dt - dN_{\alpha\beta}/dt - dN_{\beta\beta}/dt \quad [7]$$

The change in population for each level can be described using the W terms, much like a rate constant. The change in $N_{\alpha\alpha}$ will be used for the rest of the derivation.

$$dN_{\alpha\alpha}/dt = -W_1^I N_{\alpha\alpha} - W_2^{IS} N_{\alpha\alpha} - W_1^S N_{\alpha\alpha} + W_1^I N_{\beta\alpha} + W_1^S N_{\alpha\beta} + W_2^{IS} N_{\beta\beta} + \text{constant} \quad [8]$$

If the state is in thermal equilibrium, then

$$dN_{\alpha\alpha}/dt = 0, \quad [9]$$

And the expression can be simplified as

$$(W_1^I + W_2^{IS} + W_1^S)N_{\alpha\alpha}^0 + W_1^I N_{\beta\alpha}^0 + W_1^S N_{\alpha\beta}^0 + W_2^{IS} N_{\beta\beta}^0 = \text{constant} \quad [10]$$

Where N_i^0 indicates the population of spins at that energy state at equilibrium. By substituting this expression in for the constant in Equation 8, and assigning the equilibrium population state i as N_i, and given $n_i = (N_i - N_i^0)$,

$$dN_{\alpha\alpha}/dt = -(W_1^I + W_2^{IS} + W_1^S)\, n_{\alpha\alpha} + W_1^I\, n_{\beta\alpha} + W_1^S\, n_{\alpha\beta} + W_2^I S\, n_{\beta\beta}. \quad [11]$$

Similar expressions can be derived for $dN_{\alpha\beta}/dt$, $dN_{\beta\alpha}/dt$, and $dN_{\beta\beta}/dt$. Substituting these expressions in for the original equation of dI_z/dt, Equation 6,

$$dI_z/dt = 2(n_{\beta\beta} - n_{\alpha\alpha})(W_1^I + W_2^{IS}) + 2(n_{\beta\alpha} - n_{\alpha\beta})(W_1^I + W_0^{IS}). \quad [12]$$

By taking the sum and difference of I_z and S_z, we can derive expressions for the population differences to substitute into the equation.

$$2(N_{\beta\beta} - N_{\alpha\alpha}) = -(I_z + S_z) \quad [13]$$

$$2(N_{\beta\alpha} - N_{\alpha\beta}) = -(I_z - S_z) \quad [14]$$

$$2(n_{\beta\beta} - n_{\alpha\alpha}) = -(I_z - I_{z0} + S_z - S_{z0}) \quad [15]$$

$$2(n_{\beta\alpha} - n_{\alpha\beta}) = -(I_z - I_{z0}) - S_z + S_{z0}) \quad [16]$$

After substitution, dI_z/dt simplifies as follows,

$$dI_z/dt = -(I_z - I_{z0} + S_z - S_{z0})(W_1^I + W_2^{IS}) - (I_z - I_{z0} - S_z + S_{z0})(W_1^I + W_0^{IS}) \quad [17]$$

$$dI_z/dt = -(I_z - I_{z0})(W_0^{IS} + 2W_1^I + W_2^{IS}) - (S_z - S_{z0})(W_2^{IS} - W_0^{IS}) \quad [18]$$

A similar expression can be derived for dS_z/dt, and these constitute the Solomon expression for a two spin-1/2 system. Experimentally, if we saturate the frequency of the I_z spins while allowing the system to reaches a steady-state equilibrium, we set the system so that

$$dI_z/dt = 0 \quad [19]$$

$$S_z = 0 \quad [20]$$

As a result, the Solomon equations can then be simplified as

$$I_z - I_{z0} / S_{z0} = (W_2^{IS} - W_0^{IS}) / (W_0^{IS} + 2W_1^{I} + W_2^{IS}). \quad [21]$$

From this, an enhancement factor is then described as

$$f_I\{S\} = I_z - I_{z0}/ I_{z0} \quad [22]$$

$$=(\gamma_S/\gamma_I) W_2^{IS}- W_0^{IS} / W_0^{IS} + 2W_1^{I} + W_2^{IS} \quad [23]$$

$$= \sigma_{IS} / \rho_{IS} \quad [24]$$

σ_{IS} is the cross-relaxation rate constant, and the denominator, ρ_{IS}, is referred to as the dipolar longitudinal relaxation rate constant. The enhancement factor $f_I\{S\}$ is also commonly referred to as η.

NOE enhancement then becomes a probe for fast-dynamics because the fluctuations of nearby nuclei will contribute to this cross relaxation (59). Much like a radio-frequency pulse, the fluctuating interaction of two nuclei within proximity of each other is capable of causing energy transitions between those spins and promoting an NOE enhancement, provided the fluctuating interaction is on resonance with the Larmor frequency and induces relaxation. The enhancement is dependent on the rotational correlation time τ_c (**Fig 1.11**) (59). However, in NOE enhancement experiments which are used to probe the mobility of the N-H bond vector, the distance r is safely assumed to be *fixed*, leading to the probing of only the local internal fluctuations.

The $\{^1H\}$-^{15}N heteronuclear NOE experiment (**Fig 1.12**) works in an elegant fashion by taking advantage of this effect. One NOE experiment is taken with a presaturation on ^1H (hence an NOE enhancement) and one is taken without (**Fig 1.13**). A ratio of the residue intensities between these two experiments yields a residue-by-residue measure of the fast backbone dynamics.

NOE intensities are dependent on the internuclear bond distance and the molecular motions of the vector which joins these nuclei (59). Considering the N-H bond vectors in the peptide backbone, the distance is fixed, and the fluctuations of the vector are what will contribute to relaxation. The internal motion can then be described using two parameters: the generalized order parameter, S^2, and the correlation time for the internal motion, τ_e. S^2 takes on values between 0 and 1, where a value of 1 indicates the NH group is completely rigid in respect to the framework of the rest of the molecule, and values less than one indicates a greater degree of angular variations caused by internal motion (8) (**Fig 1.14**). An S^2 value of 0 means that the movement of the N-H bond vector is completely isotropic and sampling all possible orientations relative to the rest of the molecule (59).

The order parameter also affects the spectral density function (59). The common definition for the spectral density function takes into account the overall isotropic motion of the molecule, τ_c, at a given rate.

$$J(\omega) = \frac{2S^2\tau_c}{1 + (\omega\tau_c)^2} \qquad [25]$$

Considering the combination of the overall motion with the internal motion,

$$\tau_{comb}^{-1} = (\tau_c)^{-1} + (\tau_e)^{-1} \qquad [26]$$

The spectral density function becomes

$$J(\omega) = \frac{2S^2\tau_c}{1 + (\omega\tau_c)^2} + \frac{2(1-S^2)\tau_{comb}}{1 + (\omega\tau_{comb})^2} \qquad [27]$$

An important consequence of this dependence is that only internal motions faster than overall molecular tumbling can have an effect on relaxation. Therefore, the measured enhancement is sensitive only to internal motions faster than overall tumbling.

1.4.3 NMR Titrations for the Study of Protein-Protein Interactions

As methodologies progress, NMR studies of protein structure have moved towards the characterization of protein complexes in addition to singular proteins (62). By principle, proteins interact with other proteins and ligands in vivo to perform physiological tasks. Techniques in NMR that study protein-protein interactions can be applied to protein complexes at a total

molecular weight of 60 kDa, and up to 1000 kDa (62). NMR titrations offer a simple and elegant way to monitor residue specific changes in a protein upon the addition of a binding partner at an atomic resolution.

The ^{15}N HSQC titration experiment is useful for identifying key residues at the binding interface, measuring affinity, determining stoichiometry and specificity, and is also a valuable method for looking at the kinetics of the binding (62). The gradient-enhanced ^{15}N HSQC (**Fig 1.15**) is typically used, although recent advances in pulse-sequence development allows for faster data acquisition (63). The ^{15}N HSQC correlates the amide proton to the nitrogen of the peptide backbone, and generates a "fingerprint" for the protein of interest. Changes in the chemical shifts of residues, resonance intensity, and appearance of new resonances indicate structural and conformational changes in the protein induced by the presence of the binding partner, changes in electrostatics, hydrogen bonding, and other factors. Changes in the chemical shift perturbation or resonance intensity can be used to measure a binding constant of complex formation (62).

Chemical exchange will also give rise to additional resonance populations corresponding to different states of the protein during the titration. Dynamic equilibria will modify peaks and cause chemical shifts to move in NMR spectra (55). We will consider the case of either a molecule interconverting between two conformations or the binding of a ligand as two states, A and B, with an identical forward and reverse rate constant, k_1 and k_{-1}. The exchange rate is defined as the sum of these two rates.

$$A \underset{k_{-1}}{\overset{k_1}{\rightleftharpoons}} B \qquad [28]$$

If the two states A and B have distinct resonance frequencies, ν_A and ν_B, the interconversion between the two states can be categorized as slow, intermediate, or fast. These categories of chemical exchange are defined by the relationship of the exchange rate (k_{ex}) with the difference in the resonance frequencies, $\delta\nu = \nu_A - \nu_B$.

$$\textit{Slow Exchange} \quad k_{ex} << \delta\nu$$

$$\textit{Intermediate Exchange} \quad k_{ex} \sim \delta\nu$$

$$\textit{Fast Exchange} \quad k_{ex} >> \delta\nu$$

If we then consider a situation where the populations of the states A and B are equal, then in the regime of slow exchange, two equally intense and narrow peaks will appear (**Fig 1.16**) since k_{ex} is much smaller than the difference in the resonance frequencies.

As shown in **Fig 1.16**, as the exchange rate increases we observe a broadening of the two frequencies which becomes undetectable. This broad resonance is a phenomenon that occurs at the in the intermediate regime of NMR. If the exchange rate were to increase further, a gradual build up into a sharp resonance would occur at the mean frequency

$$\tfrac{1}{2} (\nu_A+\nu_B). \qquad [29]$$

which describes the fast regime.

Thus as demonstrated in **Fig 1.16** and discussed above, chemical exchange has a dramatic impact on the linewidths which are detected by NMR and much information can then be obtained about this phenomenon from the changes in linewidth. The equation which describes the change in linewidth by slow exchange is

$$\Delta\nu = k / \pi \qquad [30]$$

Where $\Delta\nu$ is defined as the change in linewidth at half maximum height (**Fig 1.17**). As k_{ex} increases, the exchange rate increase, and the line becomes widened. This phenomenon is also described as "lifetime broadening" and has some affiliation with the Heisenberg Uncertainty Principle (55, 64) (**Fig 1.17**). As the rate of chemical exchange increases, the lifetime of each species is shorter, leading to more imprecision of the energy levels. The "blurring" the measurement of the energy levels leads to line-broadening.

In the fast regime of chemical exchange, the expression for the change in linewidth is

$$\Delta\nu = \frac{\pi(\delta\nu)^2}{2k_{ex}} = \tfrac{1}{2}\pi(\delta\nu)^2\tau \qquad [31]$$

Where $\tau = 1/k_{ex}$. In order to see two separate frequencies, there would need to be an appreciable phase difference which would take a time

$$\tau = \tfrac{1}{2} (\delta\nu)^{-1}. \qquad [32]$$

If the rate of exchange k_{ex} is much faster than the difference in the frequencies between the two sites, $\delta\nu$, the phase difference between them averages to zero, and the resonance observed appears at the mean frequency. This effectively means that each spin spends on average half of the time in each site (55).

Intermediate exchange occurs when the two resonances just reach the point of merging into one broad line. For this to occur,

$$k = \frac{\pi \delta\nu}{\sqrt{2}} \sim 2.2\ \delta\nu \qquad [33]$$

These perturbations can be analyzed by utilizing line-shape analysis (65). Typically, if the protein of interest undergoes fast chemical exchange between two states, the trajectories of the resonances can yield information about binding events – a linear trajectory indicates two states in rapid exchange, while more complex trajectories indicate more than one state (62). Slow exchange will result in the appearance of new resonance populations over the course of the titration, with the free state resonances disappearing with intensity as the resonances associated with the bound, or other states, appearing. Binding constants can still be quantified by measuring the decrease of resonance intensities of the free state or increase of resonance intensities of the bound state as a function of addition of titrant, a technique explained more in detail in Chapter 4 (62). Intermediate exchange is the most difficult case to analyze since resonance frequencies lose definition and often line-broadening is so great the resonances are difficult to observe (66).

The analysis of the different types of exchange is a crucial component of analyzing the effect of structural dynamics in the allosteric mechanism of SERCA inhibition in Chapter 4. In the presence of SERCA, the different resonances of PLN undergo slow, intermediate, and fast exchange. The transition of the more thermodynamically stable T-state to the more dynamic R-state undergoes slow exchange, and line shape analysis was used to quantify the transitions and used to create a profile of the allosteric transitions for each PLN mutant studied.

1.5 TREATMENT OF HEART FAILURE BY TARGETING SERCA:PLN INTERACTIONS

Heart failure is the end-stage condition for a diverse collection of cardiovascular disorders, and is marked as a complex pathophysiological syndrome involving the circulatory, neurohormonal, and renal systems, in addition to other systems (67). In the conditions of heart failure, the amplitude and velocity of calcium cycling is depressed, and calcium homeostasis is disrupted (67, 68). Current treatments for heart failure are either focused on blocking neurohormonal pathways (β-blockers), which improve survival, but do not halt progression, or

are mechanical approaches which are invasive to the patient (valve replacements, whole heart transplants) (67, 69, 70). Thus, researchers are faced with the challenge of innovating new treatments to heart failure which directly address the underlying conditions.

Targeting Ca^{2+} cycling to treat cardiomyopathies has been of special interest, either through targeting Ca^{2+} load and storage (calsequestrin, parvalbumin, HRC), release (ryanodine receptor stabilization), or uptake (increase SERCA2a expression, protein phosphatases I inhibitors, reducing PLN inhibition) (69, 71). SERCA2a activity is depressed in failing hearts, making it a therapeutic target (72). Improving SERCA2a expression and activity has shown to be a promising avenue. SERCA2a delivered via rAAV-mediated gene therapy has been shown to improve patient mortality and morbidity in end-stage heart failure, and under the commercial name MYDICAR, has completed Phase II clinical trials (73). However, the size of SERCA2a is close to the size limitation of rAAV vector delivery, and targeting other smaller proteins that can enhance SERCA activity is a promising direction. Work by Chien and coworkers has previously demonstrated that delivery of a pseudophosphorylated PLN (S16E) effectively reversed heart failure parameters in both small and large animals under different models of heart failure (32, 33, 74). Although constitutively activating SERCA at first glance would seem to be a molecular solution to improving Ca^{2+} cycling, SERCA regulation is a complex phenomenon which needs to be finely regulated in response to various pathophysiological conditions. Hence, SERCA activity needs to stay within a "physiological window," (75) and design of therapies or small molecules to affect SERCA function should aim to finely tune its activity rather than constitutively activate the enzyme. One way to accomplish this is design of PLN mutations which are able to inhibit SERCA to varying degrees.

Numerous mutagenesis studies of PLN have been carried out by the MacLennan and Jones Groups which have offered invaluable insight to functionally relevant areas of PLN and they identified residues crucial to PLN's inhibitory ability (34) (**Fig 1.18**). What is clear from the data is that the transmembrane domain is Janus-faced, with one side of the helix primarily involved in oligomerization and the other side binding to SERCA (**Fig 1.18A, B**). Mutations in domain Ib and the domain II result in either gain-of-function (GOF) mutations when disrupting sites which are involved in oligomerization (top panel, **Fig 1.18B**), or loss of function (LOF) mutations when disrupting sites involved in binding to SERCA (**Fig 1.18C**). The overview of the results of the mutagenesis studies shows also that domain Ia and the loop are the optimum targets for designing loss-of-function (LOF) mutants, with the majority of LOF mutation sites on the face of the amphipathic cytoplasmic helix facing the membrane. From these mutation

studies, it is also clear that mutation of any of the Arg residues in PLN lead to disruption in optimum inhibitory ability of PLN, indicating their functional relevance in PLN:SERCA interactions and proper calcium cycling. What we can garner from these studies and other mutation studies (25, 76) is there exists a paradigm of conditions to consider when designing mutations of PLN for gene therapy: structural dynamics, ability to be phosphorylated, interactions with the membrane bilayer, oligomerization state, and interactions with SERCA and other proteins. Although PLNs sequence is short and it serves mostly as an inhibitor to a much larger enzyme, this makes PLNs function complex despite its compact nature, rendering each of its residues a target to manipulate its characteristics.

1.6 ORGANIZATION OF THE THESIS

Under the direction of my advisor, Dr. Gianluigi Veglia, I have worked along with other colleagues in several different angles to address how mutation of phospholamban affects its structural dynamics and interactions with its binding partners, and whether acting on the structural dynamics by mutation is a viable pathway to tuning SERCA function. We sought to use "rational design" approaches, basing the types of mutations on the structure and dynamics of PLN in its various states (reviewed in Chapter 2 and 3). The groundwork for these studies is found in Chapter 4, where we established a correlation between the structure, dynamics, and binding of PLN mutants to the level of SERCA inhibition. The study also resulted in a PLN mutant that is a promising gene therapy candidate, P21G AFA-PLN, for performing more rigorous animal screening. Initial *in vivo* studies of this mutant, done in collaboration with the lab of Dr. Roger Hajjar of Mt. Sinai Medical School, show promising results (**Fig 1.19).** What makes this mutant remarkable is that its design is based on structural dynamics and it demonstrates physiological efficacy.

Chapters 5 and 6 of this thesis aims to further develop the principles we use to rationally design gene therapy candidates and to innovate other PLN species based on the structure and dynamics of the SERCA:PLN complex. Several angles are used to address how to rationally design of these PLN mutants. I was interested in elucidating the mechanism by which known hereditary mutations of PLN led to dilated cardiomyopathy. Understanding how these mutations may lead to the manifestation of heart failure would offer insight to how to better design therapeutic mutants. The best known of these mutants, R9C, was hypothesized to have impaired phopshorylation by protein kinase A (PKA) (28). We observed that while phosphorylation of R9C by PKA was impaired in the wild-type pentameric assembly, phosphorylation was not

impaired in the monomeric form. We concluded that the Arg-Cys mutation did not directly impair PLN:PKA interactions, but rather altered the pentamer-monomer equilibrium, and that this effect was exacerbated under oxidative conditions. These results are summarized in Chapter 5.

We investigated the role of inter-domain communication in PLN, and to explore this domain of PLN, we looked at several glycine loop mutations and their effect on PLN structural dynamics and ability to inhibit SERCA. The findings show that insertion of a single glycine mutation within the loop domain confers varying degrees of SERCA inhibition. Additionally, systematic insertion of a double glycine mutation within the loop results in increasing the LOF character, while insertion of a triple glycine mutation renders a mutant that is fully inhibitory compared to the wild-type PLN. Correlated with the structure and the dynamics data, we found that as the dynamics of the loop increases, this uncouples the two helical domains of PLN, eventually crossing a threshold in the dynamics set by the phosphorylated form and resulting in a species that acts as the inhibitory transmembrane domain alone. The results of this study are in press for publication in the Journal of Muscle Research and Cell Motility and are summarized in Chapter 6.

By controlling the function of an enzyme by acting on the structural dynamic of its binding partner, the results of the research in this thesis aim to move from understanding the interplay of structural dynamics to controlling physiology at a molecular level. Thus, the overall goal of this thesis is to integrate structural biology and biophysics with physiology, and attempt to manipulate the physiological system at the molecular level using information garnered from physical data, a rationale which could be translated to similar systems where an enzyme is functionally regulated by a smaller protein or subunit.

Chapters 2-6 of this thesis consist of reprints with permission from the publisher of the following peer-reviewed articles:

Chapter 2: Background of SERCA regulation by phospholamban and sarcolipin.
Reprint from: "Structural and Dynamic Basis of Phospholamban and Sarcolipin Inhibition by Ca^{2+}-ATPase." Traaseth NJ, **Ha KN**, Verardi R, Shi L, Buffy JJ, Masterson LR, Veglia G. (2008) *Biochemistry*. 47(1):3-13

Chapter 3: Background on experimental methods applied.

Reprint from: "What can we learn from a small regulatory membrane protein?" Veglia G, **Ha KN**, Shi L, Verardi R, Traaseth NJ. (2010) *Methods Mol Biol*. 654:303-19.

Chapter 4: Structure, dynamics, and binding of a gradient of PLN mutations correlated to SERCA function.
Reprint from: "Controlling the inhibition of the sarcoplasmic Ca2+-ATPase by tuning phospholamban structural dynamics." **Ha KN**, Traaseth NJ, Verardi R, Zamoon J, Cembran A, Karim CB, Thomas DD, Veglia G. (2007) *J Biol Chem*. 282(51):37205-14.

Chapter 5: Molecular basis of dysfunction in SERCA:PLN^{R9C} interactions in reduced and oxidative conditions.
Reprint from: **"**Lethal Arg9Cys phospholamban mutation hinders Ca2+-ATPase regulation and phosphorylation by protein kinase A." **Ha, KN**, Masterson LR, Hou Z, Verardi R, Walsh N, Veglia G, Robia SL. (2011) *Proc Natl Acad Sci U S A.* 108(7):2735-40.

Chapter 6: Effect of single and multiple glycine loop mutations on PLN structural dynamics, correlated to SERCA function.
Reprint from: "Tuning the Structural Coupling between the Transmembrane and Cytoplasmic Domains of Phospholamban to Control Sarcoplasmic Reticulum Ca^{2+}-ATPase (SERCA) Function" **Ha KN**, Gustavsson M,Veglia G. 2012. In press. *J of Muscle Research and Cell Motility*.

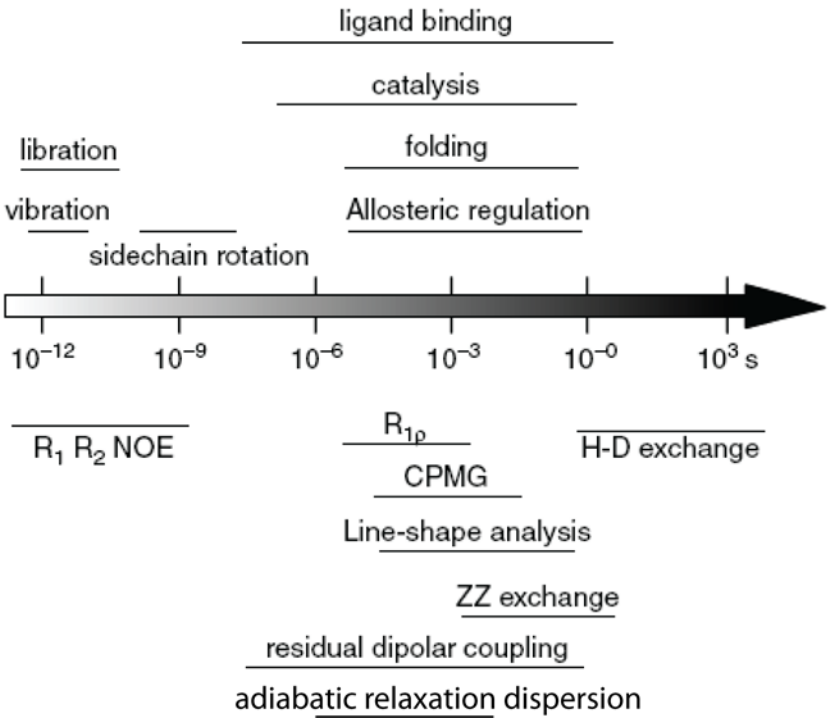

Fig 1.1 The breadth of timescales for protein motion and types of NMR experiments used to observe them. Image from Wang, *et al*. (10)

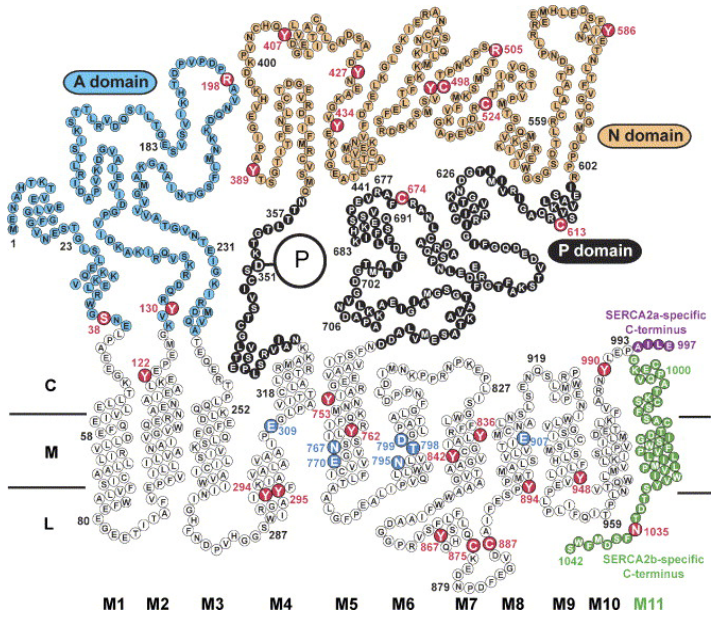

Fig 1.2 Primary sequence and secondary structure elements of SERCA2a. Picture taken from Vangheluwe, *et al*. (77)

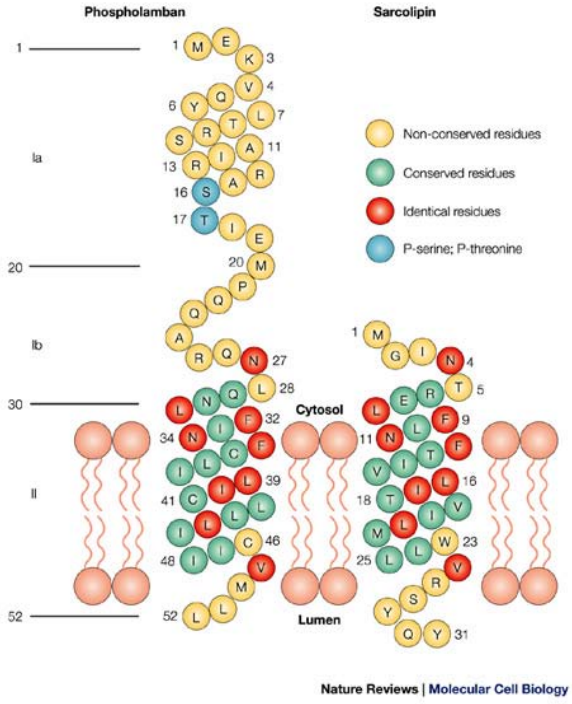

Fig 1.3 Primary sequence of PLN and SLN. Image taken from MacLennan, *et al*. (14)

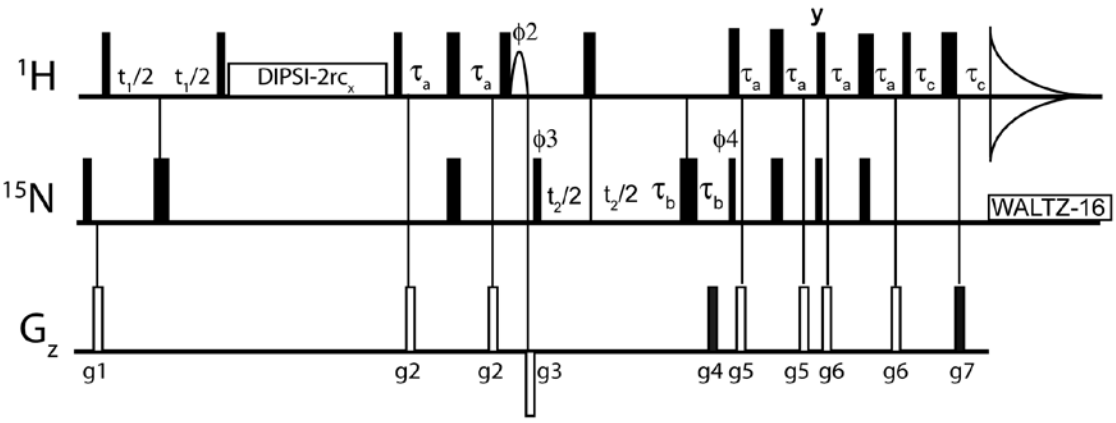

Fig 1.4 Pulse sequence for the gradient-enhanced ^{15}N-edited 3D TOCSY-HSQC. Adapted from Zhang, *et al.* (78)

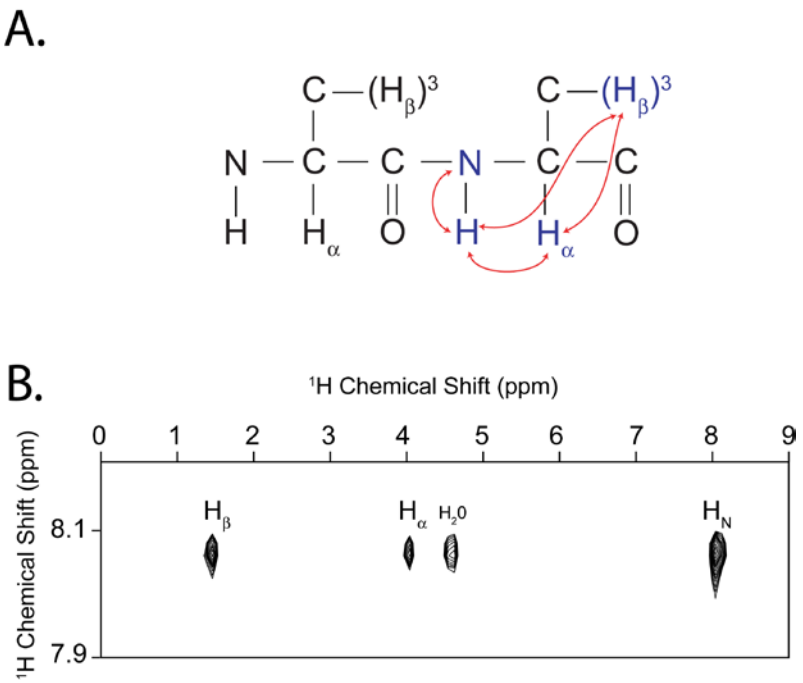

Fig 1.5 A. Magnetization transfer of the ^{15}N-edited 3D TOCSY-HSQC. B. Example of ^{1}H-^{1}H correlations in the TOCSY plane. Spin-system represented is for Ala 11 for P21L PLN.

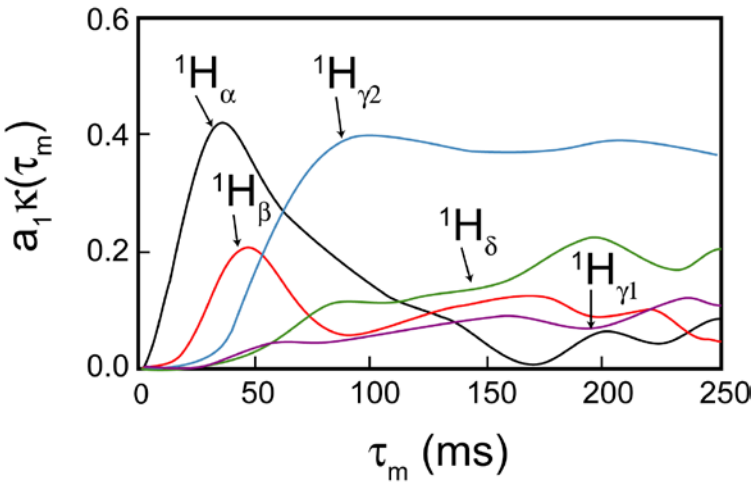

Fig 1.6 Cross-peak intensity for magnetization transfer from amide protons as a function of isotropic mixing time for an isoleucine spin system. Adapted from Cavanaugh, *et al.* (52).

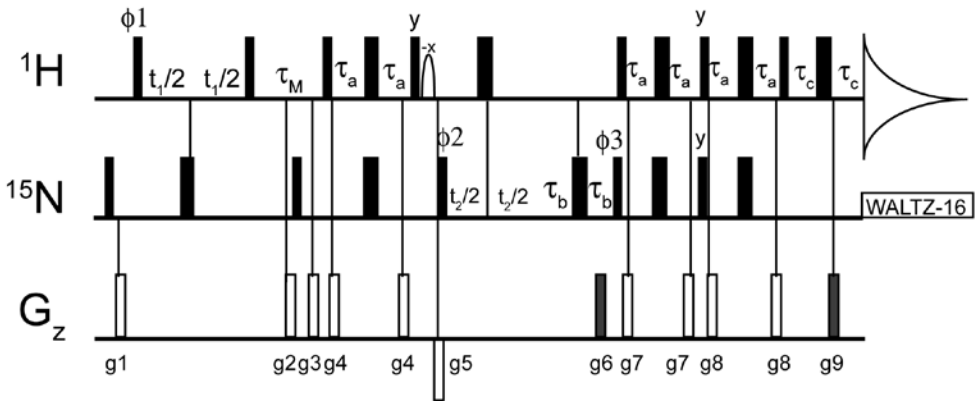

Fig 1.7 Pulse sequence for the gradient-enhanced ^{15}N-edited 3D NOESY-HSQC. Adapted from Zhang, *et al*. (78)

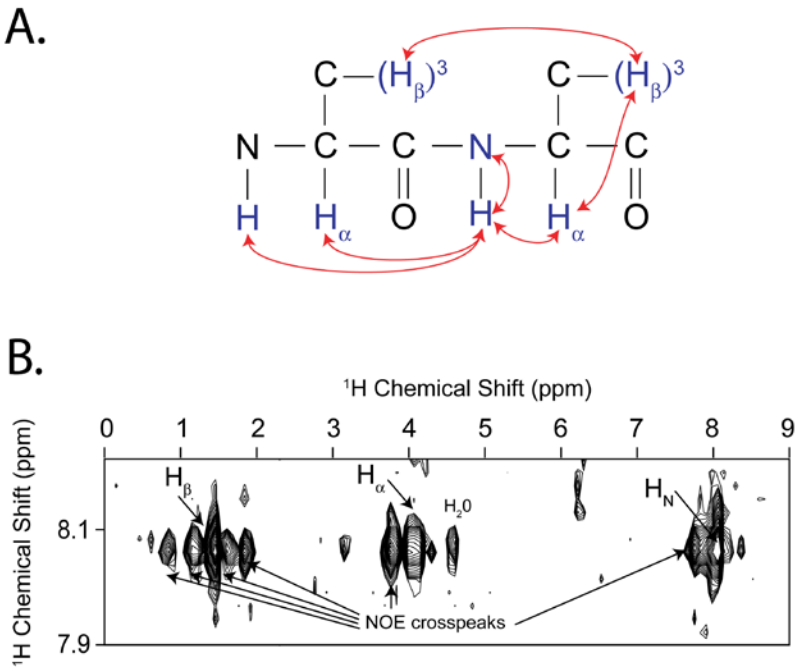

Fig 1.8 **A**. Magnetization transfer of the ^{15}N-edited 3D NOESY-HSQC. **B**. Example of NOE cross-peaks in the NOESY plane. Spin-system represented is for Ala 11 for P21L PLN.

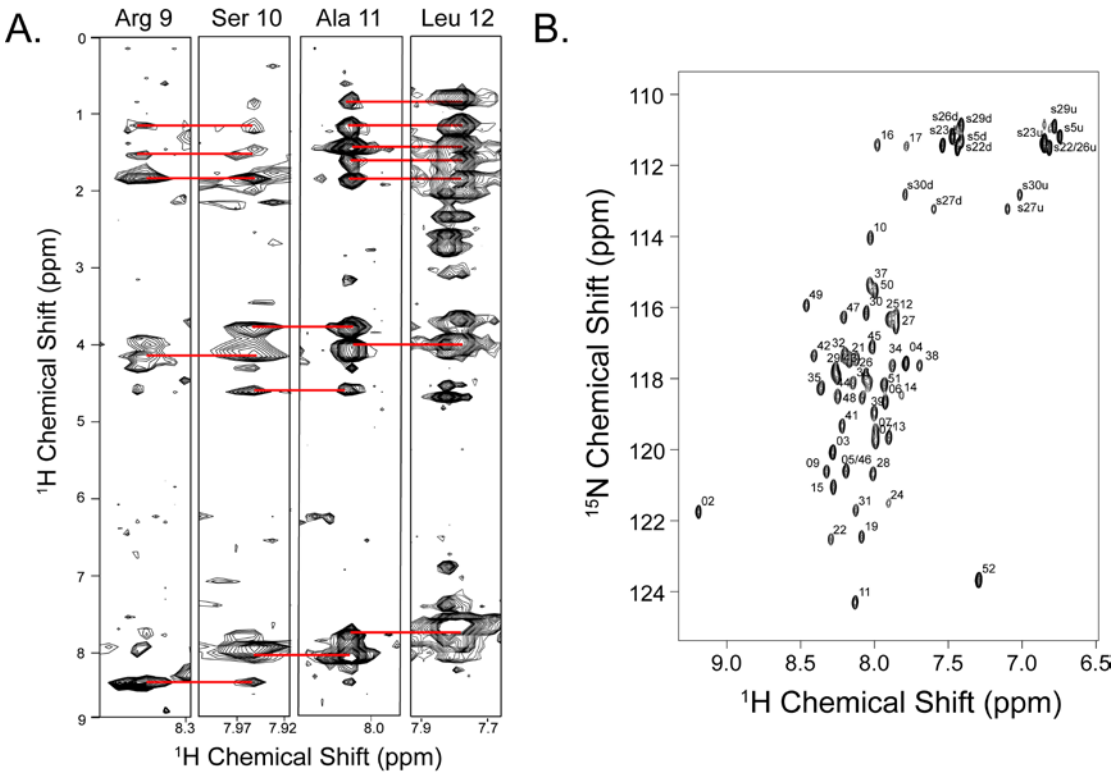

Fig 1.9 A. NOE correlations in the ^{15}N NOESY-HSQC for P21L PLN. B. Assigned ^{15}N HSQC for P21L PLN.

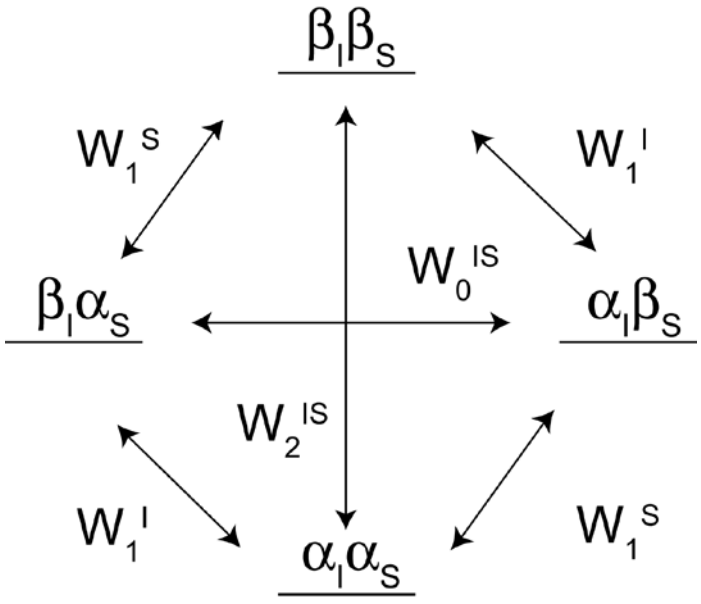

Fig 1.10 Energy levels and transition probabilities for a spin-½ pair.

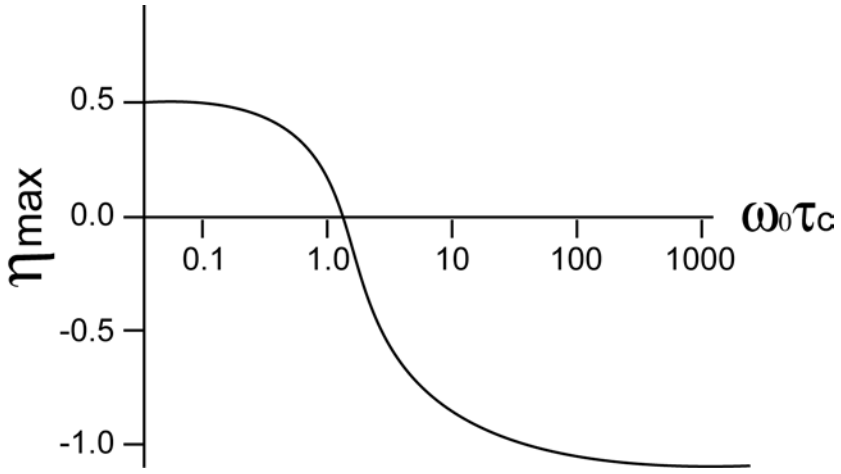

Fig 1.11 The dependence of the NOE enhancement, η_{max}, on the rotational correlation time, τ_c (56).

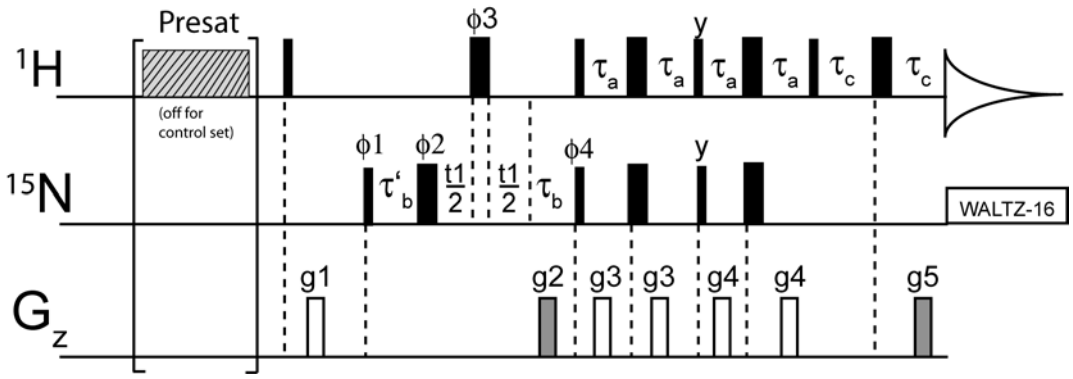

Fig 1.12 Pulse sequence for the gradient enhanced {^{1}H}-^{15}N heteronuclear NOE pulse sequence. Adapted from Farrow, *et al* (79)

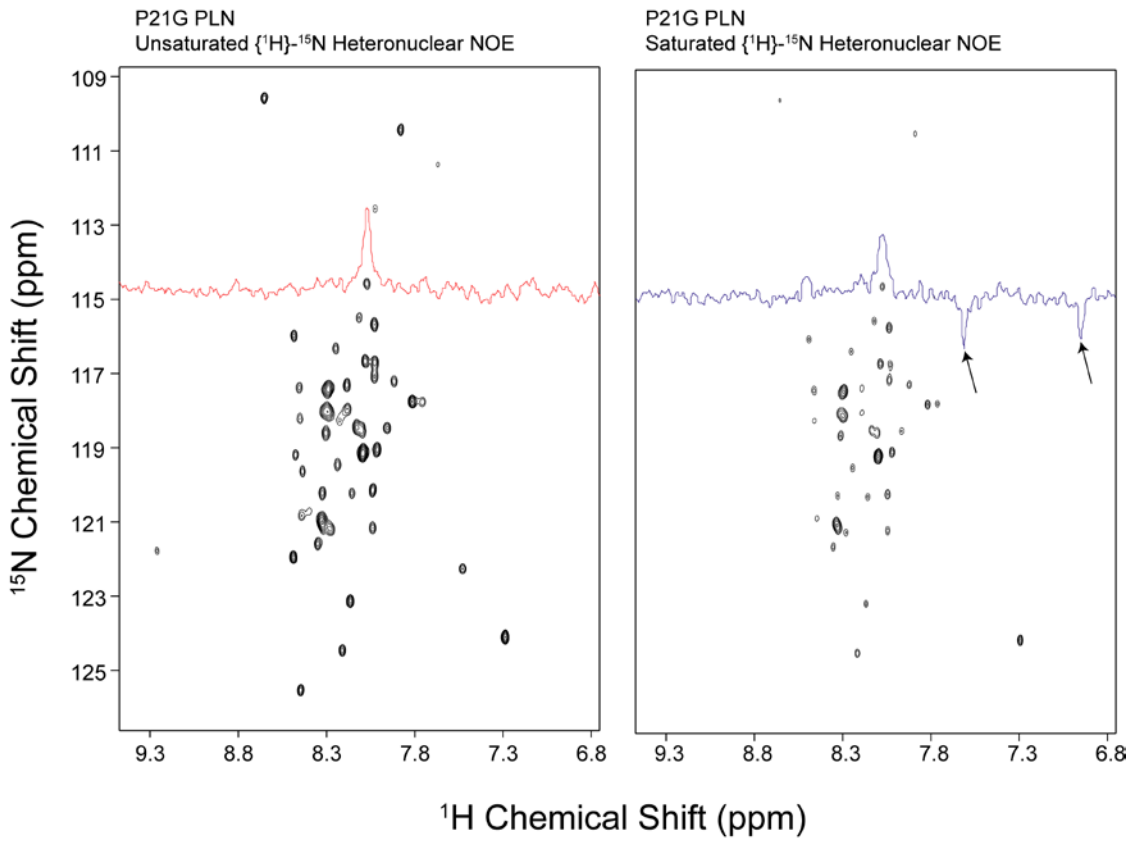

Fig 1.13 {^{1}H}-^{15}N NOE spectra. The spectrum on the left is without the ^{1}H presaturation period, and the spectrum on the right is with the ^{1}H presaturation period. Arrows in the saturated experiment are directed towards those negative NOEs corresponding to the extremely mobile NH groups of the side chains.

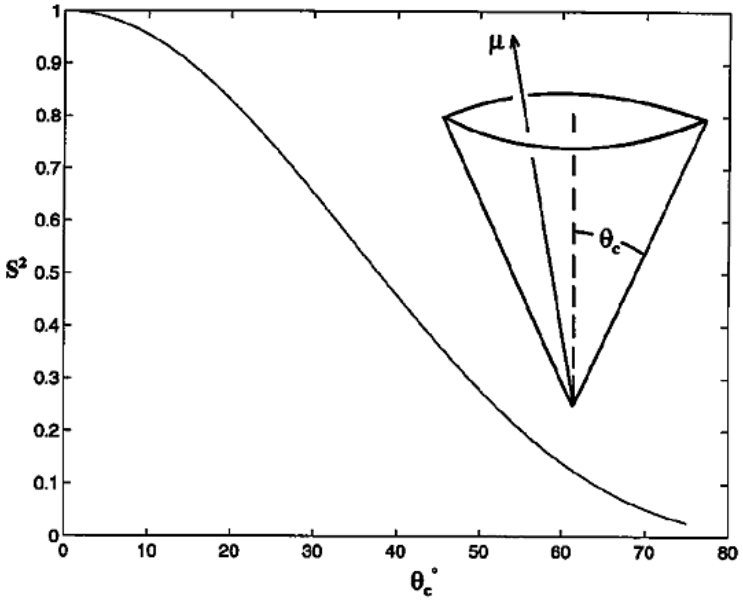

Fig 1.14 Dependence of the order parameter, S^2, on the internal correlation time, θ_c. Picture taken from Ishima, *et al.* (8)

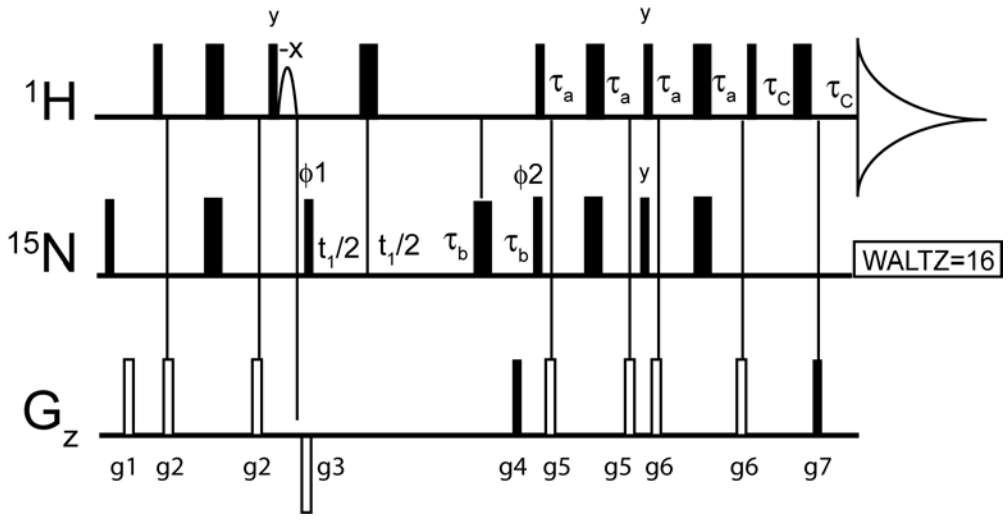

Fig 1.15 Pulse sequence for the gradient-enhanced ^{15}N HSQC. Image from Zhang, *et al*. (78)

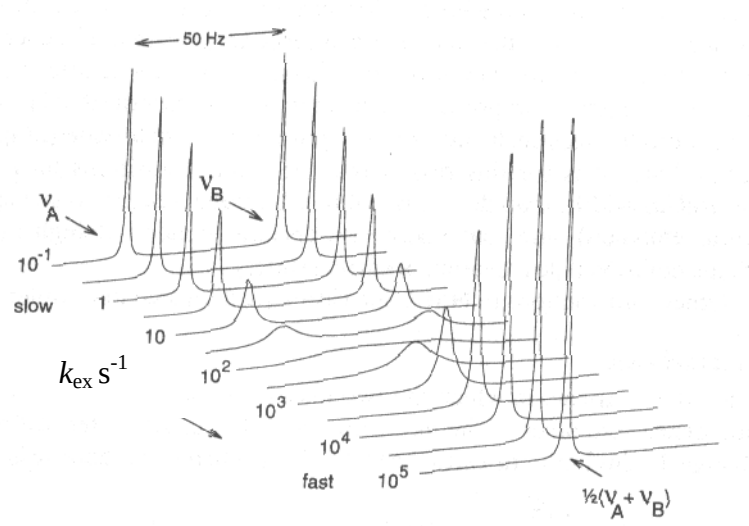

Fig 1.16 Calculated NMR spectra for a pair of nuclei exchanging at different values for the exchange rate, k_{ex}. Image taken from Hore (55).

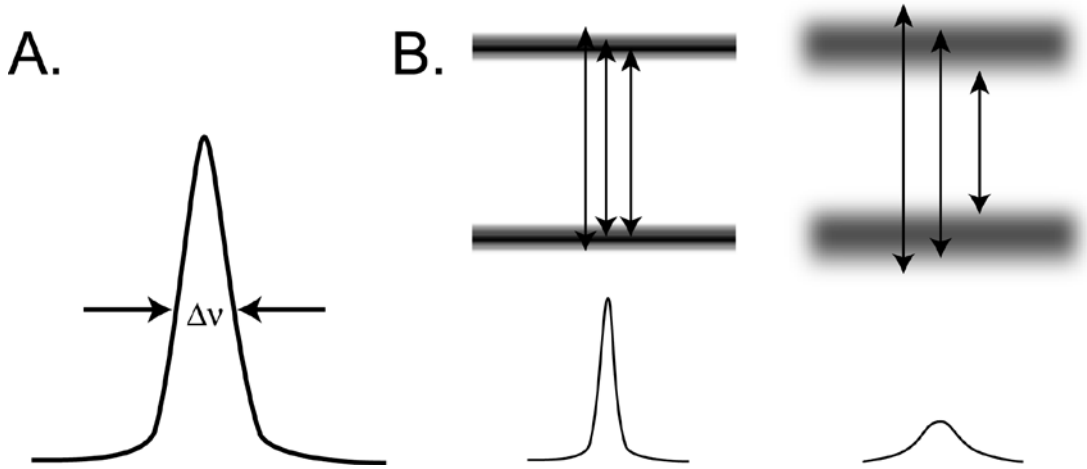

Fig 1.17 A. Linewidth at half-height. Δν is defined as the change in linewidth as a result of broadening in the presence of chemical exchange. B. The effects on exchange on line broadening. Adapted from Hore (55).

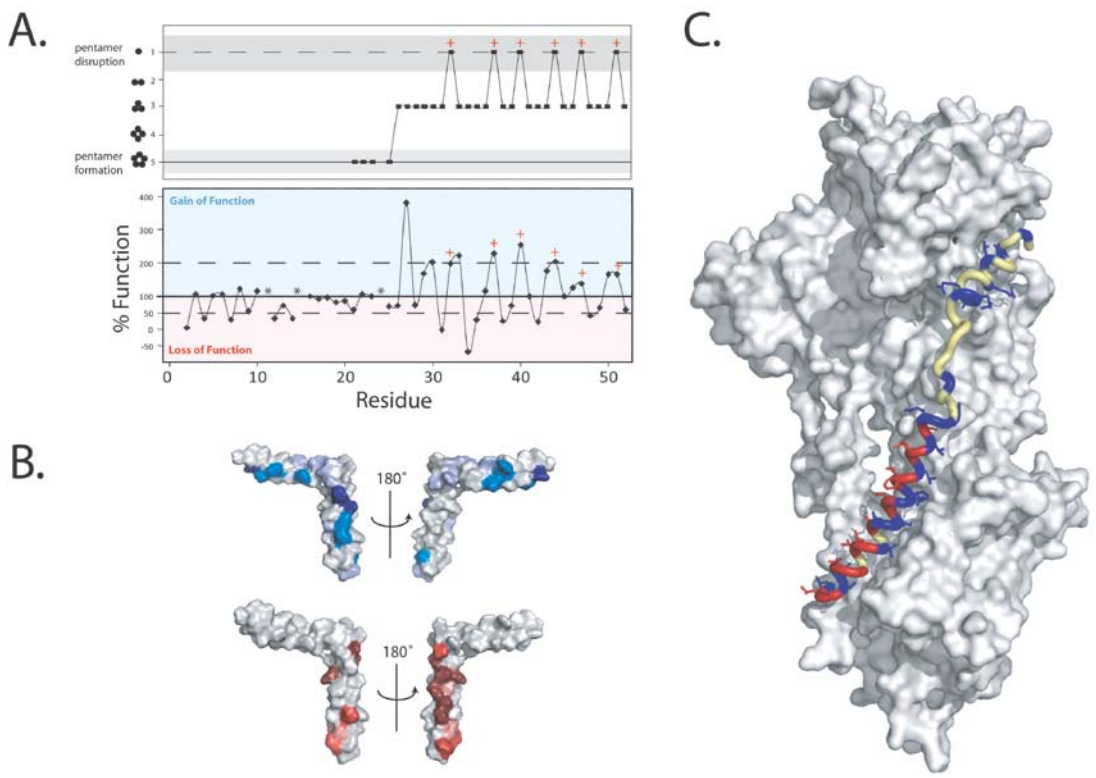

Fig 1.18 **A**. Plot of results from alanine scanning showing importance of residues for pentamer stability (top) and SERCA inhibition (bottom). The dashed line in the top graph draws the eye towards mutations which result in monomeric species of PLN. The top dashed line in the lower graph leads the eye towards gain of function mutation which increase SERCA inhibition by two-fold, while the lower dashed line highlights loss of function mutations which decrease SERCA inhibition by 50% compared to the wild-type. Red (+) symbols indicate those residues when mutated to alanine lead to a complete de-oligomerization of PLN in addition to superinhibition. **B**. Surface renderings of the PLN structure (PDB: 2KB7) with sites resulting in loss of function mutants from alanine scanning shown in blue (top) and gain of function mutants in red (blue). A darker color indicates an increasing severity in disruption of the function of that species. **C**. Plot of sites of loss of function mutations (blue) and gain of function (red) mutations on the model of the bound PLN:SERCA complex. Toyoshima C *et al* (2003)

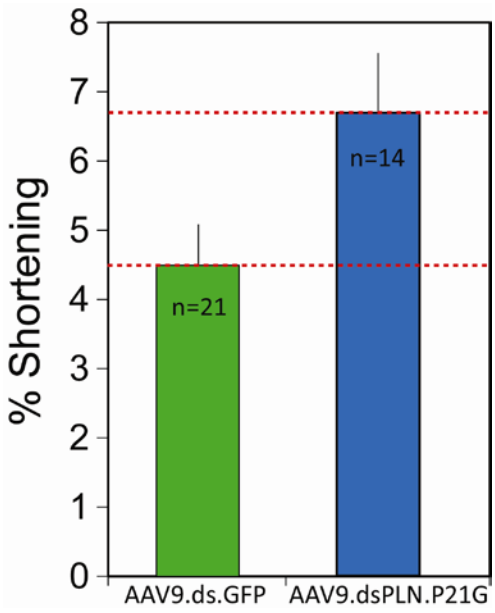

Fig 1.19 Effect on percent shortening of rat heart failure model cardiomyocytes upon delivery of GFP control (left, green) and AFA-PLN^{P21G} (right, blue) by rAAV vector. N indicates number of trials.

Chapter 2

Structural and Dynamic Basis of Phospholamban and Sarcolipin Inhibition of Ca2+-ATPase (SERCA)

Nathaniel J. Traaseth,[1] Kim N. Ha,[1] Raffaello Verardi,[1] Lei Shi,[2] Jarrod J. Buffy,[1] Gianluigi Veglia[1,2]

[1]*Department of Biochemistry, Molecular Biology and Biophysics and* ,[2]*Department of Chemistry, University of Minnesota*

Reprinted with permission from Biochemistry, Vol 47, Issue 1, pp 3-13

2.1 INTRODUCTION

Two membrane proteins, sarco(endo)plasmic reticulum calcium ATPase (SERCA) and the ryanodine receptors (RyR), play major roles in calcium regulation within muscle cells. RyR1 and RyR2 are responsible for releasing Ca^{2+} from the sarcoplasmic reticulum (SR) of skeletal and cardiac muscle, respectively, resulting in muscle contraction. Likewise, SERCA1a and SERCA2a pump calcium into the SR in skeletal and heart muscle, initiating muscle relaxation. Phospholamban (PLN), a 52-residue protein spanning the SR membrane, is an endogenous inhibitor of SERCA, lowering the apparent calcium affinity of the ATPase. The relief of SERCA inhibition is achieved by phosphorylation of PLN at Ser-16 by protein kinase A and/or Thr-17 by Ca^{2+}/calmodulin-dependent protein kinase (80). *In vivo* studies demonstrate that phosphorylation at Ser-16 and Thr-17 have different roles, suggesting that these mechanisms act independently (81, 82).

Sarcolipin (SLN) has a primary sequence homologous to that of the transmembrane domain of PLN (83, 84). Initially, SLN was thought to be the counterpart of PLN within skeletal muscle, playing only an ancillary role in cardiac muscle. Recently, however, significant expression levels of SLN have been detected in cardiac atrial muscle, with lower levels in ventricular muscle (85, 86, 87), suggesting that it may play an important role in regulation of the heart . When SLN was initially co-purified with fast-twitch skeletal SERCA1a (88), no post-translational modifications were identified, which led to the conclusion that the regulation of SLN depended on its variable expression levels (89, 90). Recent evidence shows that SLN is able to regulate SERCA and that its inhibition can be fully reversed by isoproterenol, a β-adrenergic receptor agonist, in PLN knock-out mice (17). These results led to the hypothesis that the inhibitory effect of SLN can be reversed via phosphorylation in a similar manner as PLN. *In vitro* experiments have shown that SLN can be phosphorylated at Thr-5 when co-transfected with serine/threonine kinase 16 (STK16) (17). From the biological data, it is clear that phosphorylation of PLN, and possibly SLN, constitute important driving forces for calcium re-uptake into cardiac SR.

Several crystal structures of SERCA in different conformations within the enzymatic cycle have revealed important atomic details regarding SERCA's mechanism (**Figure 2.1**) (91, 92, 93, 94, 95, 96). How much is known about the molecular details of PLN/SLN regulation and calcium translocation by SERCA? PLN is thought to bind and inhibit the low affinity calcium form of SERCA (E2) and detach from the enzyme (either partially or totally) upon phosphorylation at Ser-16, reversing its inhibitory effect and restoring the affinity of SERCA for Ca^{2+} ions. The only experimental structure of the SERCA/PLN complex is a low-resolution cryoelectron microscopy image (8-10 Å) obtained by Stokes and co-workers (97). Hampering the formation of large, highly diffracting SERCA/PLN and SERCA/SLN co-crystals is the dynamic interplay between the proteins. For this reason, MacLennan and co-workers have used a plethora of available biological data (mutagenesis studies, co-immunoprecipitation assays, and cross-linking experiments) in-concert with molecular dynamics simulations to model SERCA/PLN (98), SERCA/SLN (99), and SERCA/PLN/SLN complexes (99) (**Figure 2.2**). Hutter *et al.* have also modeled the solution structure of C41F PLN determined in chloroform/methanol with the E2 form of SERCA using molecular mechanics (100). While these models shed light into the interaction between SERCA and PLN and SLN, there are inconsistencies concerning the topology and structure of PLN and SLN within the complexes.

This review reports on our recent progress involving the structure determination of PLN and SLN in the free forms and towards elucidation of the interaction with SERCA using solution and solid-state NMR. While many contributions to the structural analysis of PLN and SLN from other laboratories are cited and related to our work, this review is not intended to be an exhaustive overview of the large amount of structural and biological information on PLN and SLN within the literature.

2.2 CHOICE OF MEMBRANE MIMICKING ENVIRONMENTS FOR SPECTROSCOPIC STUDIES

For both solution and solid-state NMR, we use two major criteria for sample preparation: 1) functionality of proteins under NMR conditions and 2) the ability to

acquire high quality NMR spectra. Being membrane embedded proteins, SLN and PLN need lipid environments to elicit their biological function. After scanning several different conditions, we chose dodecylphosphocholine (DPC) detergent micelles for solution NMR studies and a 4/1 mixture of Dioleoyl-*sn*-Glycero-3-Phosphocholine/Dioleoyl-*sn*-Glycero-3-Phosphoethanolamine (DOPC/DOPE) lipids for solid-state NMR studies. **Figure 2.3A and B** shows the calcium dependence of SERCA in the presence and absence of PLN (or SLN) under these conditions. The hydrolysis of ATP by SERCA is followed directly using ^{31}P NMR spectroscopy in DPC micelles and indirectly using the coupled enzyme assay in lipids (15, 101, 102). A representative example of the kinetic results from the ^{31}P spectroscopic assay is shown in **Figure 2.3C**. In both lipids and detergents, samples for the structure and dynamics studies are fully functional.

2.3 PLN STRUCTURE AND DYNAMICS IN DPC MICELLES

In the SR, PLN is thought to exist as an inactive pentamer (storage form), which depolymerizes into functional monomers prior to interaction with SERCA (**Figure 2.2**) (18, 19). Accordingly, we have focused our attention on a fully functional monomer of PLN (AFA-PLN) obtained by mutating the three cysteine residues (Cys-36, 41, 46) of the transmembrane domain to Ala, Phe, and Ala, respectively. Using NOE restraints in structural calculations, we have determined that PLN adopts an *L-shaped* conformation in DPC micelles comprised of three distinct structural domains: cytoplasmic domain Ia (helical from residues 2-16), loop (β-turn from residues 17-21), and transmembrane domain (helical from residues 22-52) (**Figure 2.4A and B**) (57). From simulated annealing calculations, we obtained a structural ensemble with very good convergence for each single structural domain (**Figure 2.4A**), but with the PLN conformers displaying an interhelical angle (angle between cytoplasmic and transmembrane domains) of 80 ± 22° (**Figure 2.4B**). Indeed, the limited number of NOEs detected in the loop did not allow us to constrain the two helical domains and obtain an ensemble of structures with a low RMSD over the entire protein backbone. Because of the lack of convergence on the orientation of the helical domain Ia with respect to the surface of the micelle, we used Mn^{2+} and 5’ and 16’-doxyl stearic acids as paramagnetic probes of the topological

arrangement of PLN in the micelle (57). Our results show that Mn^{2+} ions cause a reduction in the resonance intensities of residues located at both termini, the loop, and Ser-16 and Thr-17, showing that both phosphorylation sites are solvent exposed. Both 5' and 16'-doxyl stearic acids caused a reduction in the resonance intensities of residues located in the micellar region. 16'-doxyl stearic acid affected residues in the core of the micelle (residues 35-45), as well as Leu-7, located in the middle of domain Ia, a residue that is likely buried in the hydrophobic region of the micelle. At higher 16'-doxyl stearic acid/PLN ratios, domain Ia is also considerably affected by the paramagnetic center, with Ala-11 displaying slightly reduced resonance intensity.

Our structural ensemble of the PLN monomer is in qualitative agreement with studies carried out in organic solvents (103, 104), where the authors found an overall *L-shaped* structure of PLN with the intervening loop in either a short flexible turn or a β-turn type III conformation. However, we found an orientation of the cytoplasmic helix, which is in better agreement with the amphipathicity of the PLN sequence(57). The most relevant PLN conformations in PDB 1N7L are those in which the hydrophobic side chains in domain Ia (Val-4, Leu-7, Ala-11, and Ala-15) are oriented toward the interior of the micelle and the hydrophilic residues point toward the bulk solvent, rendering the two phosphorylation sites exposed for interaction with their respective protein kinases.

While our NMR structural studies identified *three structural domains*, nuclear spin relaxation measurements and solvent accessibility experiments carried out on uniformly ^{15}N labeled PLN(22, 105) further subdivided the helical segment from 22-52 into two domains: domain Ib (residues 22-31), which is more dynamic and constituted by hydrophilic residues, and domain II (32-52), more hydrophobic and motionally restricted. Therefore, we can divide PLN into *four dynamic regions*, which are characterized by different order parameters (see **Figure 2.4A** and **2.4B**). Carr-Purcell-Meiboom-Gill (CPMG) based relaxation measurements also indicated the presence of slow dynamics (μs-ms motion) in domain Ia, the loop, and domain Ib (22, 105). While the slow dynamics of domain Ia and the loop were predicted based on the H/D exchange factors, the flexibility of residues within domain Ib was unexpected. The plasticity of this region

supports biological evidence for the great importance of domain Ib and the molding necessary to *fit* into the binding groove of SERCA(98, 106).

Recently, a structure of wild-type PLN (wt-PLN) was reported showing the pentamer to be in a *bellflower* arrangement, where the cytoplasmic domain helix of each monomer makes an ~20° angle with respect to the bilayer normal(37), substantially different from the topology we reported for monomeric AFA-PLN(57). Our recent studies using solution NMR and EPR in DPC detergent micelles also point toward a dominating *L-shaped* conformation (or *pinwheel* model) for the pentamer(107). We also looked at the topology of pentameric wt-PLN in lipid bilayers using solid-state NMR, finding unambiguous evidence in support of the *pinwheel* model (see below).

2.4 SLN STRUCTURE AND DYNAMICS IN MICELLES

The initial structure of SLN was determined in sodium dodecyl sulfate (SDS) micelles using a synthetic polypeptide(108). Under these experimental conditions, SLN has an α-helical conformation from residue F9 to R27 with RMSDs of 0.65 and 1.66 Å for backbone and side chain atoms, respectively. Both the N-terminus (M1 to L8) and the C-terminus (S28 to Y31) were found to be unstructured. Subsequently, we expressed uniformly ^{15}N labeled recombinant SLN in *Escherichia coli*, which enabled the use of higher resolution [^{1}H, ^{15}N] NMR experiments in order to reduce several ambiguities in resonance overlap. With recombinant SLN, we determined the structure in DPC micelles, conditions that ensured the activity of SERCA, and found it to remain a single transmembrane helix with approximately five unstructured residues at either terminus (15). The superposition of the C_α, N_H and C' backbone atoms from residue R6 to R27 gave an RMSD of 0.4 ± 0.2 Å with an RMSD of 1.7 ± 0.3 Å for side chain atoms.

In addition to structure determination, we also measured spin relaxation rates, and found that the backbone dynamics, similar to PLN, is more complex than the structure. Relaxation measurements reveal four dynamic domains: a short unstructured N terminus (residues 1–6), a short dynamic helix (residues 7–14), a more rigid helix (residues 15–26), and an unstructured C terminus (residues 27–31) (15). H/D exchange factors also support the existence of four dynamic domains (15). The similarity of SLN structure and

dynamics with those of PLN domains Ib and II shows that sequence conservation is reflected in the conservation of both structure and dynamics (**Figure 21C**).

2.5 PLN AND SLN TOPOLOGIES AND DYNAMICS IN LIPID BILAYERS

Solid-state NMR in lipid bilayers has emerged as a complement to solution NMR studies in detergent micelles for elucidating structure, dynamics, and interactions between membrane proteins(109, 110). For our first solid-state NMR studies, we synthesized AFA-PLN ^{15}N labeled at Ala-11, Ala-15, and Ala-36, and measured the ^{15}N chemical shift anisotropy in 4/1 DOPC/DOPE mechanically oriented lipid bilayers on glass plate supports(111). Using these solid-state NMR measurements in concert with rigid body molecular mechanics, we found that the domains Ib and II are oriented approximately perpendicular to the plane of the bilayer with the interhelical (i.e. interdomain) angle ranging between 60 and 100°, ruling out the possibility of a continuous α-helix and also suggesting that the cytoplasmic domain of PLN interacts with the membrane surface.

Similar solid-state NMR measurements on SLN oriented in mechanically aligned DOPC/DOPE bilayers revealed the approximate parallel orientation of the SLN helix with respect to the membrane bilayer normal(108). Since the limited number of labeled sites did not allow us to give quantitative topological angles for SLN and PLN within the bilayer, we then proceeded to use 2D [^{1}H, ^{15}N]-PISEMA (polarization inversion spin exchange at the magic angle) experiments(112). This separated-local-field experiment correlates the ^{15}N chemical shift anisotropy (CSA) with the ^{1}H-^{15}N dipolar coupling (DC). Since the values of both CSA and DC depend on the orientation of the peptide plane with respect to the direction of the magnetic field, the assignment of the amide resonances allows for the determination of the structure and topology in aligned lipid bilayers.

We determined that AFA-PLN has an overall *L-shaped* conformation in mixed 4/1 DOPC/DOPE lipid bilayers, where the helix comprising domains Ib and II makes a tilt angle of ~21° with respect to the bilayer normal (113). As expected from the 1D solid-state NMR studies on synthetically ^{15}N labeled AFA-PLN (36), PISEMA NMR spectroscopy clearly shows that domain Ia interacts with the membrane surface, making

an angle of ~93° with respect to the bilayer normal (113). A current model of the PLN monomer is reported in **Figure 2.5**.

In addition to the structural and topological information obtained from oriented alignments, tilting the aligned samples to different angles with respect to the direction of the static field makes it possible to investigate the rotational dynamics of the protein within the bilayer (114, 115, 116). Tilting the AFA-PLN sample by 90° revealed that the domains Ib and II undergo fast long-axial rotational diffusion about the bilayer normal with the cytoplasmic domain undergoing this same motion and other complex dynamics, scaling both the values of CSA and DC (113). The dynamics detected in both our solution and solid-state NMR experiments may explain variability within the literature regarding the topology of the cytoplasmic domain of PLN. For example, a magic-angle-spinning (MAS) solid-state NMR study carried out by Baldus and co-workers found that while cross-polarization (CP) based pulse sequences were adequate to detect the transmembrane domain of AFA-PLN, showing the existence of a well-defined helix, the cytoplasmic domain residues were too dynamic to be detected(117). Instead, J-coupling coherence transfers, similar to those in solution NMR experiments, were used to detect the dynamic cytoplasmic domain, which resulted in the conclusion that the cytoplasmic domain was completely unstructured. While this study represents advancement in MAS methodology, the structure most likely represents a minor conformational state and is inconsistent with a wealth of data, including those from our laboratory, which consistently show a predominant helical cytoplasmic domain with an overall *L-shaped* monomeric structure in lipid bilayers and detergent micelles.

A close inspection of PISEMA spectra from selectively labeled samples reveals the presence of two peak populations that exemplify two slightly different topologies for the AFA-PLN domains Ib and II (113). The two topologies have the same tilt angle (θ) for domain Ib and II with respect to the membrane normal, but slightly different rotational angles around the helix axis (ρ). Multiple populations of PLN have also been observed by the Lorigan and Middleton groups using MAS NMR experiments in lipid vesicles (118, 119). The detection of multiple conformers underscores the plasticity of PLN, and might

be an important recognition mechanism for SERCA, protein kinase A, and protein phosphatase 1, previously shown necessary for physiological processes(106).

As with AFA-PLN, the PISEMA spectra of SLN obtained on uniformly ^{15}N labeled and selectively [^{15}N-Leu], [^{15}N-Ile], and [^{15}N-Val] samples also revealed the existence of two distinct topologies (120). Both the major and the minor populations of the resonances corresponding to domains Ib and II are oriented ~23° with respect to the lipid bilayer normal, but vary in the rotation angle about the helical axis by ~5° (in remarkable agreement with AFA-PLN). The primary sequence homology between SLN and PLN results in nearly identical structural and dynamic properties of these two regulatory proteins.

2.6 PENTAMERIC WT-PLN TOPOLOGY IN LIPID BILAYERS

More recently, our group has embarked on the validation of the pentameric structure of wt-PLN in lipid bilayers and detergent micelles (107). While monomeric PLN has previously been shown to bind and inhibit SERCA, a recent hypothesis proposed that the pentamer could also bind and inhibit SERCA (121). While there is broad consensus regarding the secondary structure of penameric wt-PLN, there is disagreement in the literature over the orientation of the cytoplasmic helix. In particular, there are four proposed models for pentameric wt-PLN (**Figure 2.6**). The first model (*extended helix/sheet*) shows wt-PLN to be comprised of two α-helices connected by an anti-parallel β-sheet (residues 22-32), where the cytoplasmic domain is oriented 50-60° relative to the bilayer normal (122). The second model depicts wt-PLN as a continuous α-helix with a tilt angle of 28 ± 6° with respect to the bilayer normal (123, 124). The third model (*pinwheel*) shows that the most stable pentamer has a *pinwheel* geometry in which the cytoplasmic domain helices are oriented ~90° with respect to the membrane bilayer normal (40). The fourth and most recent model (*bellflower*) shows the structure of the pentamer to be in a *bellflower* assembly with the cytoplasmic domain helices oriented ~20° with respect to the bilayer normal (37).

To study the topology of pentameric wt-PLN, we reconstituted the protein in mechanically aligned 4/1 DOPC/DOPE lipid bilayers and analyzed the protein's architecture using [^{1}H, ^{15}N] PISEMA spectroscopy. As with the AFA-PLN monomer (113), we found that the wt-PLN PISEMA spectrum is composed of three different populations of resonances (see 1D spectrum in **Figure 2.7A**) corresponding to: a domains Ib and II (with the resonances located between 170-220 ppm), an in-plane cytoplasmic domain (with resonances located between 50-100 ppm), and a more flexible region (loop and termini) with resonances clustered around ~110 ppm (isotropic portion of the spectrum). Since our 1D spectrum shows three distinct regions, indicating three unique wt-PLN domain alignments with respect to the membrane bilayer normal, this eliminates the possibility of the *continuous helix* model.

To distinguish between the other models depicted in **Figure 2.6**, we performed PISEMA experiments using selectively [^{15}N-Ala], [^{15}N-Thr], [^{15}N-Leu], [^{15}N-Ile], [^{15}N-Cys], and [^{15}N-Asn] labeled wt-PLN samples. Our experimental PISEMA spectra, reported as an overlay in **Figure 2.7**, show a remarkable similarity with the AFA-PLN monomer. In fact, the simulations for the cytoplasmic domain resonances (Leu-7, Thr-8, Ala-11, Ile-12, Ala-15, Thr-17, Ile-18) correspond to a helix with a tilt angle of ~90° with respect to the bilayer normal (**Figure 2.7E**) (107).

Figure 2.8 shows PISEMA spectra simulated from the *pinwheel* and *bellflower* PDB coordinates for those selectively labeled sites shown in **Figure 2.7**. If the pentamer topology corresponded to the *pinwheel* model, the cytoplasmic domain residues would resonate in the upfield region of the spectrum (50-100 ppm) (**Figure 2.8A**). On the other hand, if the architecture of wt-PLN were consistent with the *bellflower* model, the cytoplasmic domain resonances in the PISEMA pattern would occupy the downfield portion of the spectrum (170-220 ppm), as represented in **Figure 2.8B**. Comparing the experimental cytoplasmic domain spectra, it is clear that in lipid bilayers the cytoplasmic domain is oriented perpendicular with the bilayer normal forming an overall *pinwheel* geometry.

Structural fitting with an ideal helix in **Figure 2.7D** revealed that the helix corresponding to domain Ib and II of pentameric wt-PLN has a tilt angle (θ) of ~15° with

respect to the bilayer normal (107). Monomeric AFA-PLN has a tilt angle of ~21° (125, 126), which requires pentamer formation to tilt by ~6° to accommodate the leucine/isoleucine zipper holding the pentamer together (125, 126).

2.7 ALLOSTERIC ACTIVATION MODEL

The functionality of SERCA under NMR conditions and the quality of AFA-PLN spectra upon addition of SERCA enabled the *unprecedented* atomic mapping of the interactions between these two integral membrane proteins in detergent micelles (125, 126). In its free form, AFA-PLN exists in a dynamic equilibrium between two conformations, T and R states, where the T state or *L-shaped* conformation is thermodynamically stable, and the R state or extended form is identified with a more dynamic cytoplasmic domain (**Figure 2.9**) (127, 128). These two states are readily detected using EPR spectroscopy in both micelles and lipid bilayers (127, 128), but due to the timescale of the exchange NMR can only imply the existence of these forms from relaxation dispersion measurements (i.e. conformational interconversion). However, upon addition of SERCA to AFA-PLN, chemical shift perturbation analyses reveal the appearance of a second population of peaks within domain Ia, the loop, and domain Ib, indicating a conformational switch of AFA-PLN from the T to the R state, a process exemplifying an allosteric activation mechanism (127).

Resonances from the hydrophobic portion of the transmembrane region (domain II) also show chemical exchange to the R state (102). A difference plot of $^{1}H_{N}$ chemical shift before and after addition of SERCA for residues 32-52 shows a symmetric bimodal behavior where the C-terminal part of domain II shifted upfield and the residues near the N-terminal part downfield (102). Since upfield and downfield shifts have been correlated to the strength of hydrogen bonds (129), one possible explanation of the data is that the C-terminal end of the transmembrane domain (residues 46-52) unwinds upon binding SERCA. This hypothesis was first proposed by MacLennan and co-workers, who indicated an overall change in the secondary structure of the transmembrane domain, with residues 49-52 unwinding upon interaction with SERCA, a process that might facilitate binding (98).

These results are echoed in the binding of SLN to SERCA (15). Overall, SLN behaves like the transmembrane domain of AFA-PLN, with each dynamic domain mimicking the behavior of the corresponding domain in AFA-PLN. Upon addition of SERCA, the transmembrane domain is in fast exchange between two free forms (T and R states). As previously indicated, spin relaxation measurements dissected the transmembrane domain of SLN into two regions we named domain Ib and domain II in analogy with AFA-PLN. The chemical shift changes of these two regions follow the bimodal behavior of the transmembrane domain of AFA-PLN, indicative of a similar mechanism involving an unwinding of the C-terminal residues and a stabilization of the residues in the N-terminal portion of the protein as a result of the interactions with SERCA (15). This supports the hypothesis that both SLN and PLN transmembrane domains bind SERCA in the same site and with an identical mechanism.

2.8 EFFECTS OF PLN PHOSPHORYLATION ON THE ALLOSTERIC MECHANISM

The inhibition of SERCA by PLN can be reversed by phosphorylation at Ser-16 by cAMP-dependent protein kinase A (15). We solved the structure of Ser-16 phosphorylated AFA-PLN (pS16-AFA-PLN) and found that residues 14-16, previously helical, became unwound upon phosphorylation, revealing an order-to-disorder transition (105). In addition, we found that there are pronounced changes in pS16-AFA-PLN backbone dynamics on both the ps-ns and μs-ms timescales (105). Although small, some of the changes are propagated throughout the entire protein backbone, demonstrating that while the structural transitions following phosphorylation are localized, the changes in backbone dynamics are irradiated throughout the protein.

How can this order-to-disorder transition help in understanding the interaction with SERCA? To answer this question, we proceeded with the analysis of chemical shift perturbation of pS16-AFA-PLN induced by SERCA (102). We found that the conformational equilibrium between the T and R states upon addition of SERCA is influenced by the single phosphorylation at Ser-16; specifically, phosphorylation shifts the equilibrium toward the R state in a cooperative manner (102). Another considerable

difference upon phosphorylation includes a change in both the surface and the dynamics of domain Ib. In particular, a remarkable change is observed for the side-chain binding behavior. In constrast with unphosphorylated PLN, the Gln-26 resonance in the phosphorylated protein is unperturbed by SERCA with other smaller changes seen for side chain residues Asn-27, 30, and 34. A possible mechanism to explain these results is the rotation or rearrangement of domain Ib upon phosphorylation that disrupts crucial intermolecular hydrogen bonds, resulting in relief of inhibition. Based on the molecular model by MacLennan and co-workers (98), we proposed that a crucial hydrogen bond formed between Arg-324 and Gln-26 may be broken between AFA-PLN and SERCA after phosphorylation at Ser-16 (102). These findings are in agreement with mutagenesis studies, showing that Q26A is a loss-of-function mutant (130). In addition, cross-linking studies show that an N27C mutation in pS16-AFA-PLN is no longer able to cross-link with SERCA (98). While there are changes in the binding interface for domain Ib, the overall binding of the transmembrane domain to SERCA is not affected by phosphorylation. The overall dissociation constants (K_d) for domain II in both pS16-AFA-PLN and AFA-PLN are ~60 μM (102). This demonstrates that the major changes are in domain Ia, loop, and domain Ib, with domain II only marginally affected, supporting the hypothesis that phosphorylation at Ser-16 does not dissociate PLN from SERCA completely. We proposed domain Ib as a bridgehead region, which transmits the dynamics induced by phosphorylation at Ser-16 from the cytoplasmic helix to domain Ib, thereby regulating the intramembrane protein-protein interaction (102). A schematic of the allosteric model for phosphorylation is reported in **Figure 2.9**.

2.9 PERSPECTIVE

What can we learn from the analysis of the structure and dynamics of PLN? More importantly, how are structure and dynamics of PLN correlated to SERCA's function, and can we control the extent of inhibition of SERCA by manipulating PLN structural dynamics? These are questions we have begun to address concerning PLN and look forward to answering in the upcoming years.

Given the plethora of biochemical and molecular biology data currently available, it is a very exciting moment for the structural biologists involved in research on PLN and SLN and their interactions with SERCA. While our studies to date have focused on detecting the effects of PLN induced by SERCA, our future challenge involves detecting SERCA changes from PLN within the entire enzymatic cycle. Another important challenge is to study the SERCA/PLN complex in the complicated network of interactions involving protein kinase A and protein phosphatase 1. While solution NMR will help identify some important pieces of this complex puzzle, solid-state NMR will be the method of choice for the elucidation of the structural dynamics and interactions in these large complexes.

2.10 FOOTNOTES

We are grateful to members of the Veglia Laboratory who laid the foundation for the subsequent studies on PLN and SLN: Alessandro Mascioni, Bethany Buck-Koehntop, Jamillah Zamoon, and Emily Metcalfe, and for the productive collaboration with the laboratory of David Thomas. This work was supported by grants to GV (NIH GM64742, NIH HL80081, AHA 0160465Z).

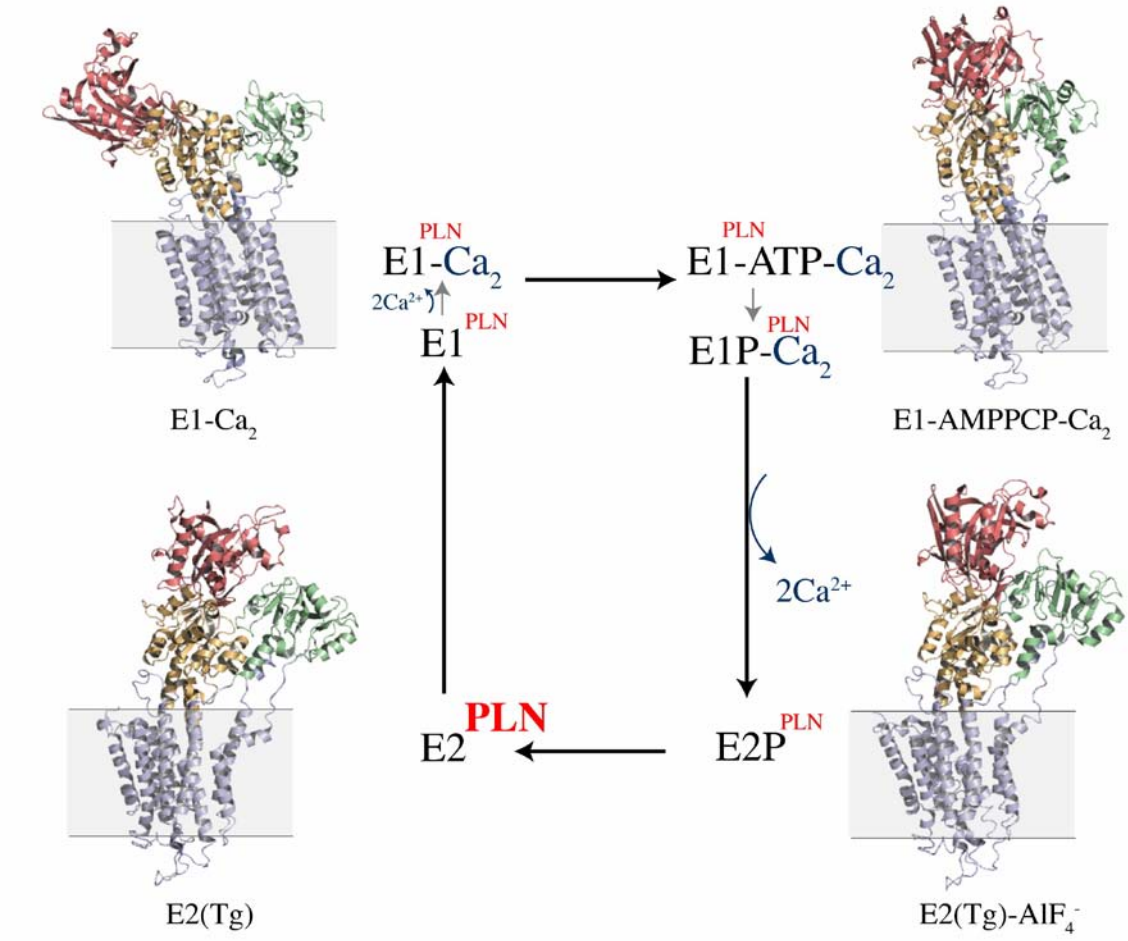

Figure 2.1. Enzymatic cycle mimicking the four major conformational states of SERCA: E2 (*1IWO)* (92), E1-Ca_2 (*1SU4)* (91), E1-ATP-Ca_2 (*1VFP)* (94), E2P (*1XP5)* (95). PLN and SLN are believed to inhibit the E2 conformation as indicated within the model. The model was reproduced from Inesi *et al.* (131).

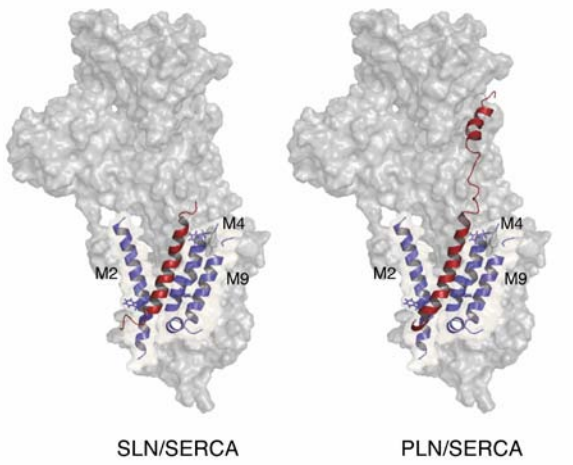

Figure 2.2. Models of SERCA/PLN (98) and SERCA/SLN (99). Coordinates of complexes generously provided by D.H. Maclennan.

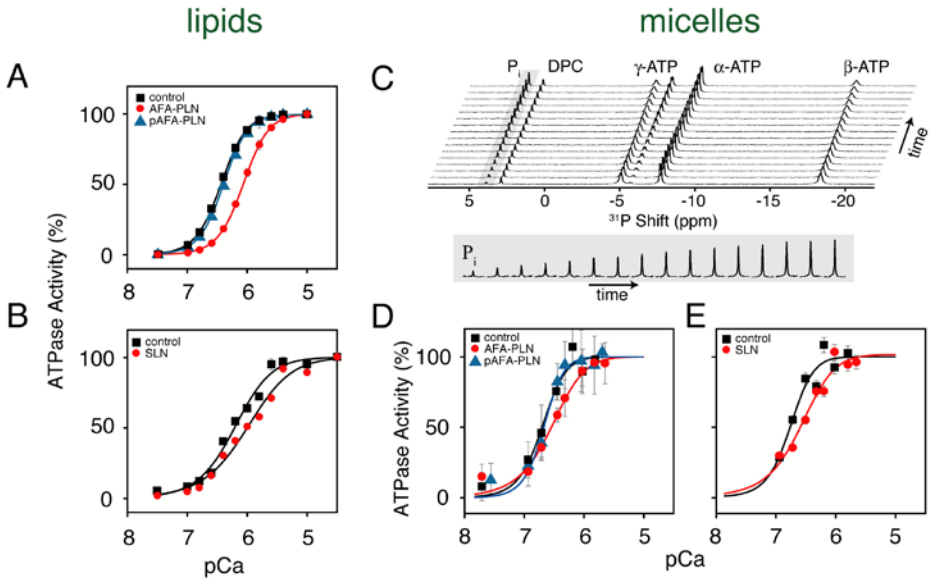

Figure 2.3. Activity assays of SERCA in the presence and absence of PLN and SLN in 4/1 DOPC/DOPE lipid bilayers (A and B) and DPC detergent micelles (D and E). SERCA activity in lipid bilayers was measured via the coupled enzyme assay and is reproduced from Buck *et al*. (101). The activity assays in DPC micelles were done using ^{31}P NMR spectroscopy as previously reported (102), reproduced from Buffy *et al.* (15) and Traaseth *et al*. (102).

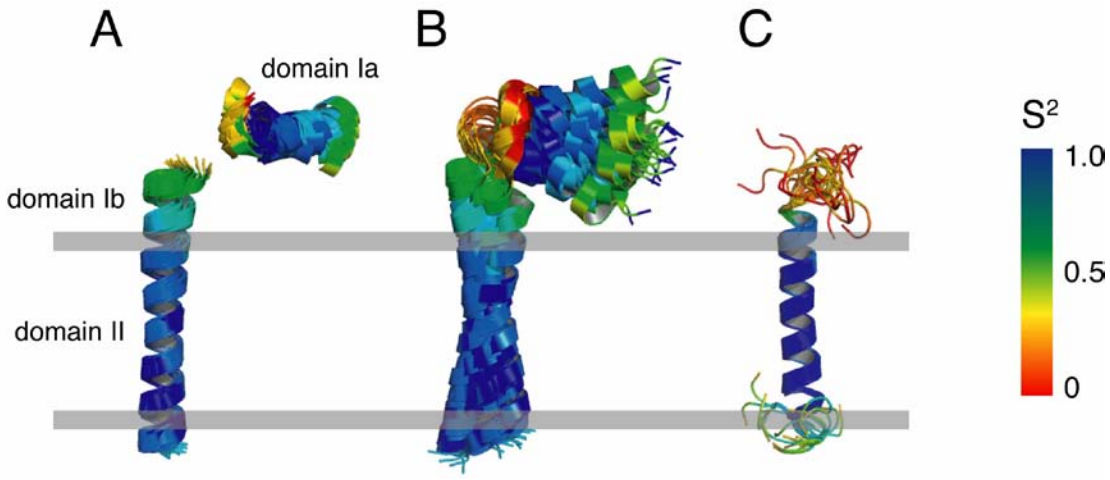

Figure 2.4. A) Separate overlay of PLN residues 2-16 and 22-52 from PDB *1N7L* (57). B) Entire backbone overlay of PLN from PDB *1N7L* (57). C) Backbone overlay of SLN as reported by Buffy *et al.* (15). The color-coding on the structures corresponds to the order parameters (S^2) as previously determined (22, 105).

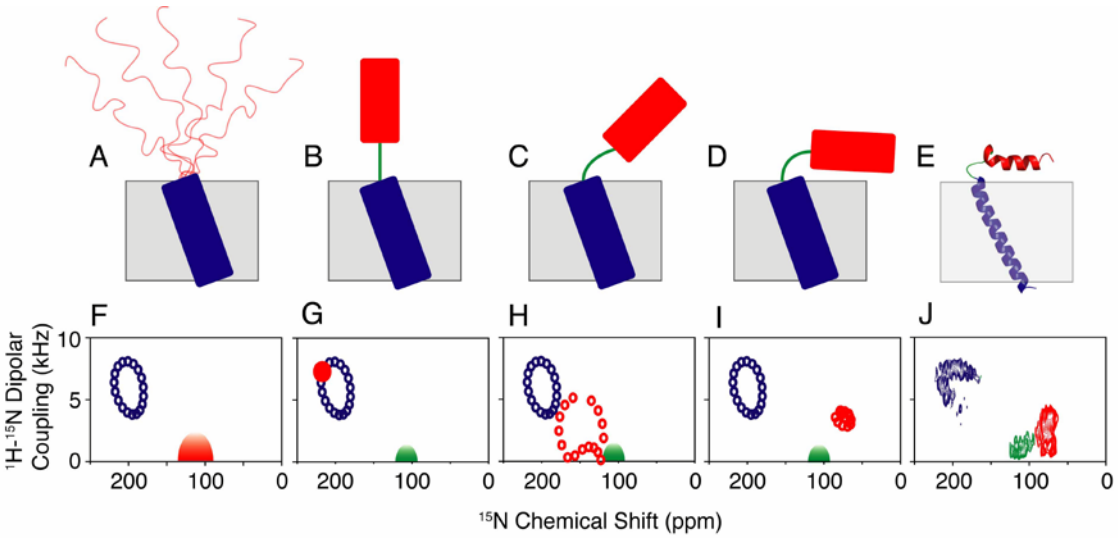

Figure 2.5. Structural models (panels A-D) proposed for PLN in lipid bilayers with PISEMA simulations (panels F-I). The ensemble of conformers reported by our laboratory (PDB 1N7L) is shown in panel E (57). The colors are coded with the regions of the protein: red for cytoplasmic, blue for transmembrane, and green for loop regions. The L-shaped topology (panels D and E) agrees best with the experimental PISEMA (panel J). Taken from Traaseth *et al.* (113).

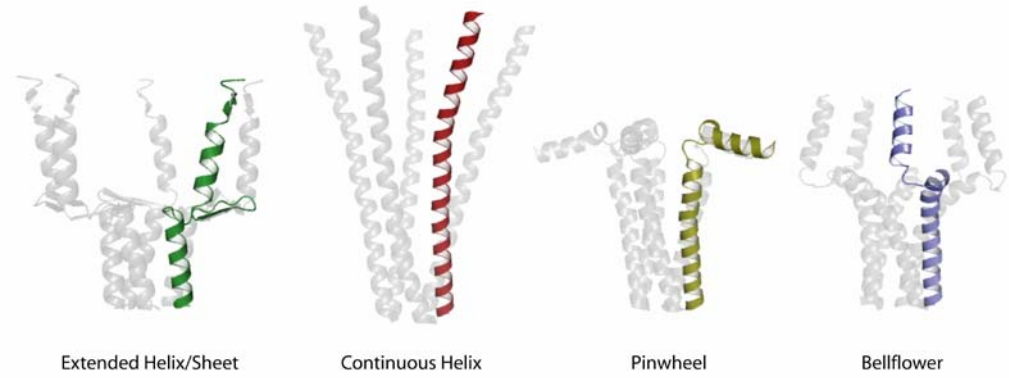

Figure 2.6. Structural models of wt-PLN. The *pinwheel* (*1XNU*) and *bellflower* (*1ZLL*) pentamer models were taken directly from PDB coordinates. Taken from Traaseth *et al.* (107).

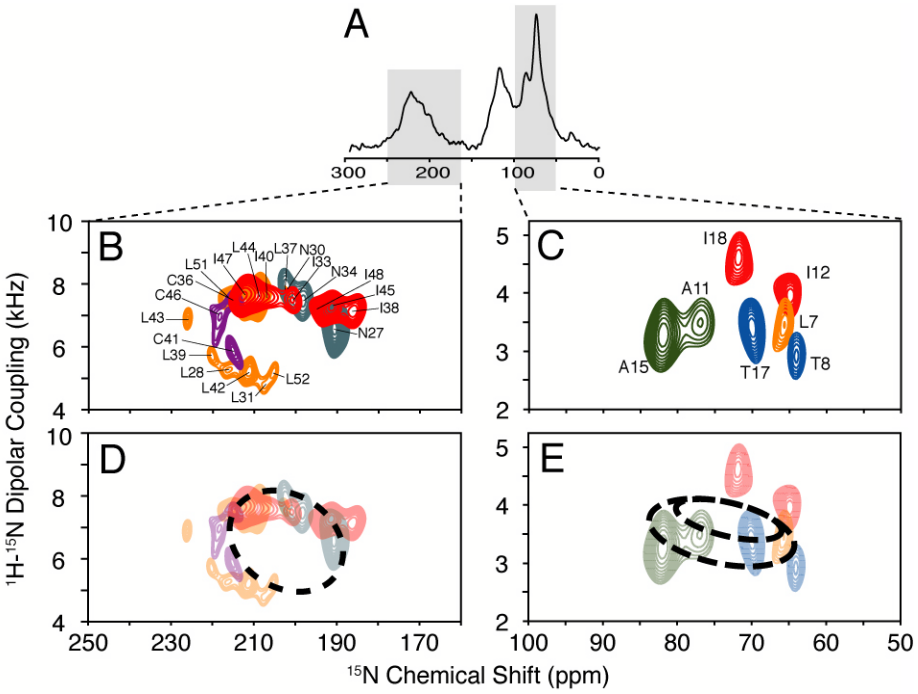

Figure 2.7. PISEMA spectra of PLN pentamer in lipid bilayers. (A) 1D cross-polarization spectrum of [U-^{15}N] wt-PLN in DOPC/DOPE oriented lipid bilayers. (B, C) Selectively labeled wt-PLN PISEMA spectra for the transmembrane and cytoplasmic helices, respectively. The residues are color coded with the PISEMA spectra: [^{15}N-Ala] green, [^{15}N-Cys] purple, [^{15}N-Leu] orange, [^{15}N-Ile] red, [^{15}N-Asn] gray, [^{15}N-Thr] blue. (D, E) Simulated PISA wheels for both transmembrane (θ=15°) and cytoplasmic (θ=92°) domains. Taken from Traaseth *et al.* (107).

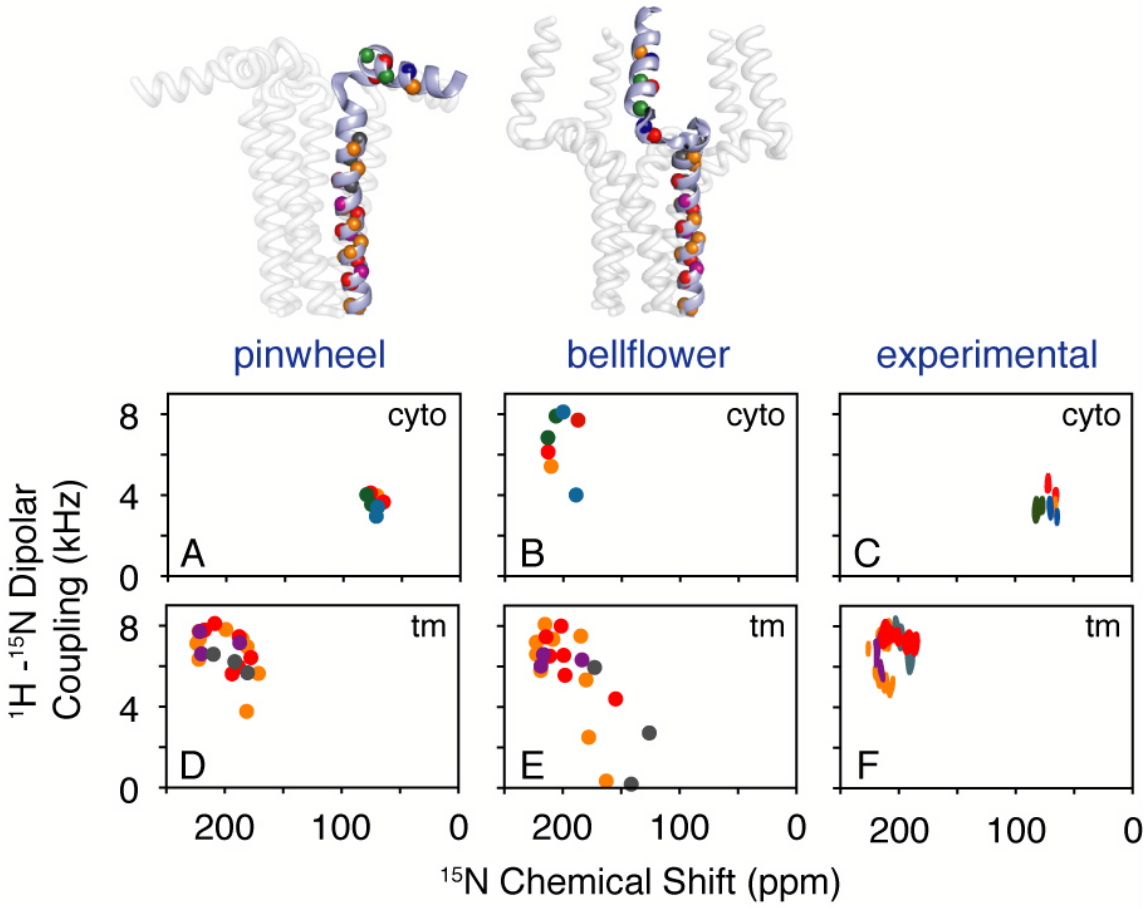

Figure 2.8. Simulated PISEMA spectra for the *pinwheel* and *bellflower* models. Unlike the *pinwheel* model, the *bellflower* model shows no high-field resonances. Experimental PISEMA spectra show the remarkable agreement with the *pinwheel* model (C, F). Taken from Traaseth *et al.* (107).

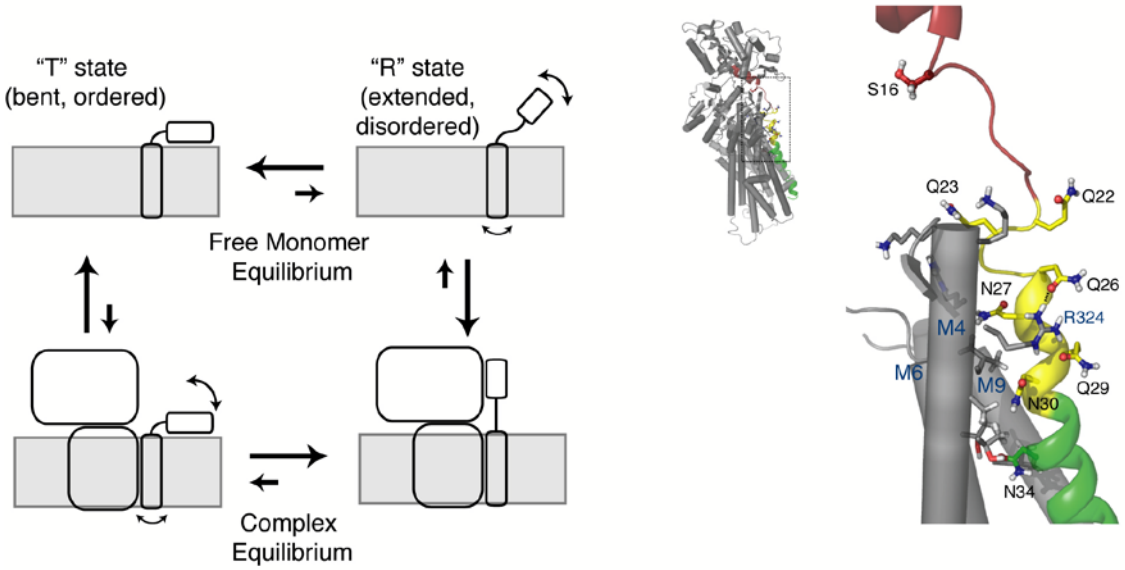

Figure 2.9. A) Allosteric model of PLN interaction with SERCA and the effect of phosphorylation at Ser-16 (indicated in red). PLN monomer interconverts between the L-shaped form (T state) and the less stable (more dynamically disordered) extended form (R state). B) PLN/SERCA model developed by Toyoshima *et al.* (98) highlighting the long range allosteric control phosphorylation at Ser-16 has on domain Ib. Figure adapted from Zamoon *et al.* (127) and Traaseth *et al*. (102).

Chapter 3

What Can We Learn From a Small Regulatory Membrane Protein?

Gianluigi Veglia[1,2], Kim N. Ha[1], Lei Shi[2], Nathaniel J. Traaseth[1], and Raffaello Verardi[1]

[1]*Department of Biochemistry, Molecular Biology and Biophysics and* ,[2]*Department of Chemistry, University of Minnesota*

Reprinted with permission from Methods in Molecular Biology: Membrane Protein Structure Determination, Vol 654, pp. 303-319

3.1 INTRODUCTION

Phospholamban (PLN) is a small integral membrane protein (52 residues) localized in the sarcoplasmic reticulum (SR) membrane that regulates the flow of calcium ions into the SR lumen of cardiac muscle (14). Specifically, PLN binds to SR calcium ATPase (SERCA), the enzyme responsible for calcium re-uptake into the SR lumen. In its unphosphorylated form, PLN inhibits SERCA by reducing its affinity for calcium. Upon β-adrenergic stimulation, PLN is phosphorylated by protein kinase A at S16 with concomitant relief of SERCA inhibition and restoration of SERCA activity. These cyclic events account for the relaxation (diastolic phase) of the heart muscle and if disrupted, may evolve into heart failure (132). Due to their central role in cardiac muscle contractility, PLN and SERCA have become targets for new, alternative therapies for heart failure (133). What can be learned from the study of the structural and dynamic transitions of PLN free and when bound to SERCA, and, more importantly, can these studies contribute in the development of new clinical approaches to heart failure?

Much progress has been made toward understanding the molecular mechanism of SERCA within the enzymatic cycle (131, 134). Undeniably, the first crystal structure of SERCA (E1-Ca_2, calcium bound form) solved by Toyoshima and co-workers paved the way for the atomic level understanding of calcium translocation in the SR (91). To date, there are ~10 crystal structures of SERCA under different experimental conditions that are allowing enzymologists to model the major conformational states of the enzyme during turnover (135). However, very few studies have been dedicated to the determination of the complexes between SERCA and its endogenous inhibitor PLN. This is probably due to the inherent dynamics of the SERCA/PLN complex that might complicate the formation of large, diffracting crystals. This hypothesis is reinforced by several fluorescence and EPR studies published by the Thomas and Squier Laboratories underscoring the dynamic nature of the SERCA/PLN complex (38, 136, 137, 138, 139). So far, the labs of Stokes and Young (121, 140) have produced the best images of this complex, although the resolution of the crystals does not define the interaction surface between the two proteins at the atomic level. NMR studies, on the other hand, have been focused on the structural dynamics of PLN in the free forms. This is mainly due to the

difficulties in producing recombinant SERCA and analyzing its complex with PLN by solution-state NMR (M_w ~ 116 kDa).

Our laboratory in collaboration with the Thomas laboratory has used a combination of solution and solid-state NMR methods to map the structural dynamics, topology and interactions between PLN and SERCA. Based on our chemical shift perturbation data from solution NMR, we have constructed an allosteric model for SERCA regulation by PLN (38, 102, 127, 141, 142). This regulatory model has been now adopted by several groups in the fields of structural biology and muscle physiology to explain the effects of naturally occurring and engineered mutations in PLN. More importantly, this model has allowed us to rationally manipulate the structural dynamics of PLN and design new mutants that are possible candidates for gene therapy.

In the following sections, we briefly review the molecular biology, biochemistry, and NMR approaches we have used to study SERCA's regulation by looking at PLN free (monomeric and pentameric) and bound to SERCA. We show the progression of our research from our initial hypotheses on the mechanism of SERCA regulation by PLN to our initial attempts to control PLN structural dynamics to tune SERCA's function.

3.2 MATERIALS

3.2.1 Expression and purification of monomeric and pentameric PLN

3.2.1.1. Plasmid construction and mutagenesis of AFA-PLN

1. pMal c2E maltose binding protein vector (New England Biolabs, MA)
2. Oligonucleotide primers (Biomedical Genomics Center, University of MN)
3. Pfu Turbo DNA polymerase (Stratagene, La Jolla, CA)
4. dNTP mix (Promega, Madison, WI)
5. T4 DNA ligase (Promega, Madison, WI)
6. 1x Luria-Bertani (LB) media
7. Qiaprep Spin Miniprep Kit (Qiagen, Valencia, CA)

3.2.1.2 Expression of unlabeled and ^{15}N uniformly labeled PLN

1. BL21(DE3) strain *Escherichia coli* cells (Novagen, NJ)
2. 1x Luria-Bertani broth media

3. M9 minimal media containing 12.8 g/L Na_2HPO_4 $7H_2O$, 3 g/L KH_2PO_4, 0.5 g/L NaCl, and 1 g/L ^{15}N-labeled NH_4Cl, 2 g/L glucose, and 0.1% w/v ampicillin.

4. 1 M IPTG (Gold Biotechnology, St. Louis, MO)

5. Mineral cocktail: 6 mg/L $CaCl_2$, 6 mg/L $FeSO_4$, 1 mg/L $MnCl_2$, 0.8 mg/L $CoCl_2$, 0.7 mg/L $ZnSO_4$, 0.3 mg/L $CuCl_2$, 0.02 mg/L H_3BO_3, 0.25 mg/L $(NH_4)_6MO_7O_{24}$, 5 mg/L EDTA.

6. Vitamin cocktail: 1 mg/L calcium pentothenate, 1 mg/L biotin, 1 mg/L folic acid, 1 mg/L niacinamide, 1 mg/L pyridoxal phosphate.

3.2.1.3 Purification of PLN

1. Lysis buffer: 20mM PBS pH 7.3, 120 mM NaCl, 8 mM EDTA, 0.1 mM DTT, 52.6 mM glycerol, 0.5 μg/ml Pepstatin A, 0.5 μg/ml Leupeptin, 2.5 μM lysozyme, 4.5 mM Tween-20.

2. Amylose affinity chromatography resin (New England Biolabs, MA).

3. Wash buffer: 20 mM PBS pH 7.3, 120 mM NaCl.

4. Maltose elution buffer: 46 mM maltose in 20 mM PBS pH 7.3, 120 mM NaCl, 1mM EDTA and 3.1 mM NaN_3.

5. Recombinant tobacco etch virus serine protease (Invitrogen, Carlsbad, CA).

6. Dialysis membranes with 1000 kDa molecular weight cutoff.

7. HPLC purification: H_2O with 0.1% trifluoroacetic acid and isopropanol.

3.2.1.3 Quantification

1. Biorad gradient 10-15% polyacrylamide gel (Biorad, Hercules, CA).

2. Protein standard.

3.2.1.5 Phosphorylation of PLN at S16 by cAMP dependent Protein Kinase A

1. Phosphorylation buffer: 20 mM MOPS (pH 7.3), 1%□β Octylglucoside, 1 mM ATP, and 1mM $MgCl_2$.

2. cAMP dependent protein kinase A catalytic subunit (Sigma) or recombinant kinase as described in ref. (105).

3.2.2 SERCA Preparation

1. White muscle from the back and hind legs of rabbit.
2. Extraction buffer: 20 mM MOPS and 0.1 M KCl, pH 7.
3. Sucrose buffer: 20 mM MOPS, 0.3 M sucrose, 1 mM NaN_3.
4. Reactive red affinity resin (Sigma).

5. SERCA buffer: 5 mM DPC, 1 mM $CaCl_2$, 1 mM $MgCl_2$, 20 mM MOPS (pH 7.0), 20% glycerol, 0.25 mM DTT, and 4 mM ADP.

3.2.3 Functional Assays

3.3.3.1 SERCA PLN Co-reconstitution

1. 1,2-dioleoyl-*sn*-glycero-3-phosphocholine (DOPC) and 1,2-dioleoyl-*sn*-glycero-phosphoethanolamine (DOPE) (Avanti Polar Lipids, Alabaster AL).
2. Biobeads (Biorad, Hercules, CA).
3. β–Octylglucoside (Sigma).

3.2.3.2 ATPase Activity Measurements

1. Coupled-enzyme assay mix containing 0.5 mM phosphoenol pyruvate, 2.5 mM ATP, 0.2 mM NADH, 2 IU of pyruvate kinase, 2 IU of lactate dehydrogenase, and 1-2 μg calcium ionophore (A23187).

3.2.3.3 ^{31}P NMR Activity Assays

1. Couple-enzyme assay mix containing a final concentration of 10 mM dodecylphosphocholine, 1 mM $MgCl_2$, 80 mM ATP, 20 mM MOPS (pH 7.0), and 0.2% $C_{12}E_8$.

3.2.4 NMR Spectroscopy

3.2.4.1 Solution state samples for titration

1. Dodecylphosphocholine (DPC) (Avertec or Cambridge Isotope Laboratories).
2. Solution state NMR sample buffer containing 20 mM Na_2PO_4, 120 mM NaCl, and 0.1% NaN_3.
3. Mini-dialysis chambers (Millipore, Billerica, MA).
4. Guanidinium-HCl (Sigma)
5. Dialysis buffer: 20 mM PBS and 50 mM β-mercaptoethanol.

3.2.4.2 Oriented Samples and ssNMR Spectroscopy

1. 10% (w/v) sodium lauryl sulfate (SDS).
2. DOPC and DOPE lipids.
3. Ultra filtration concentrator (Amicon, Millipore Corporation, Bedford, MA)
4. Glass plates, 8 x 12 mm (Marienfeld GmbH & Co, Lauda-Konigshofen, Germany).
5. Trifluoroethanol.
6. Extruder (Northern Lipids Inc. Burnaby, BC Canada).

3.3 METHODS

3.3.1 Expression and Purification of Monomeric and Pentameric PLN

For structural studies of membrane proteins by NMR, it is necessary to find a robust expression system that allows for the purification of milligram quantities of pure protein. For this purpose, we optimized a fusion protein construct for both monomeric (cysteine null PLN whith the following mutations C36A, C41F, C46A, which we called AFA-PLN) and pentameric species (101).

3.3.2 Construction of PLN and Mutant PLN Expression Plasmids

To maximize the expression, all of the codons were optimized for *E. coli*. The nucleic acid sequence was divided into four overlapping primers and three PCR reactions were performed, with incorporation of a TEV protease cleavage site between MBP and PLN, an *EcoR*I restriction site at the 5'end, and a *Hind*III site at the 3' end (a map of the plasmid is available from ref. (101)). Each polymerase chain reaction (PCR) was performed with a total volume of 50 μL containing 0.06 μM of each oligonucleotide, 80 μg of parental template, 200 μM dNTP mix, and 5.0 U Pfu Turbo DNA polymerase. Each PCR reaction was carried out in an Eppendorf Master Cycler system with standard temperature cycling suggested for Pfu Turbo DNA polymerase. AFA-PLN PCR product was amplified and then ligated into *EcoR*I and *Hind*III sites on the pMal c2E vector using T4 DNA ligase. The ligated product was used to transform XL1-Blue competent cells with transformants selected by growth on LB/ampicillin plates. For single-site mutations of PLN, the forward and reverse primers were designed with optimized codons for *E. coli* three residues before and after the target residue to be mutated. PCR was performed with Pfu DNA polymerase using the protocol as described above. PCR products were then digested with Dpn-I in order to remove non-mutated methylated dsDNA, and then were transformed into XL-Blue competent cells. Constructs were amplified and extracted using the Qiaquick Spin Miniprep kit.

3.3.3 PLN Expression

E. coli BL21(DE3) cells were transformed with MBP-PLN fusion constructs. 100 ml of LB growth media with 50 μg/ml ampicillin was inoculated with a single colony and grown ~16 h at 25 °C shaking at 250 RPM to reach an OD_{600} of ~1.0. The growth was then diluted (1:50) into M9 media containing mineral and vitamin cocktails and grown at 37 °C to an OD_{600} of ~1.0.

Protein expression was induced with 1 mM IPTG for 4.5 h at 37 °C. All cells were harvested by centrifugation at 6,370 x g for 20 min at 4 °C. Pellets were stored at -20 °C.

3.3.4 PLN Purification

PLN pellets (~10-15 g) were resuspended in ~400 ml of lysis buffer and agitated by blending using a Sorval Omni-Mixer 17105. Cell lysates were then sonicated on ice for 15 min using a Branson Sonifier 450 sonicator at an output setting of 4 and a duty cycle of 45%. After sonication, lysates were spun down at 45,700 x g for 20 min at 4 °C. The supernatant containing MBP/PLN fusion protein was applied to an amylose resin affinity chromatography column at 4 °C. The column was washed with 12 column volumes of wash buffer until the OD_{280} reached ≤ 0.05. The protein was eluted using a maltose solution, which MBP preferentially binds, separating the protein from the amylose resin. PLN was cleaved from MBP with TEV protease at 100 U/mg fusion protein at 30°C for ~5-8 h. At this point PLN can be further purified in two ways: 1) an S-100 sephacryl gel filtration column using an AKTA*prime* liquid chromatography system (Amersham Pharmacia Biotech), or 2) using reversed-phase HPLC. While we originally used the gel filtration method, we have abandoned this method in favor of the faster and higher resolving HPLC method as reported by Young and co-workers (143). For the HPLC method, the cleavage reaction was dialyzed against 4 L of ddH_2O in a 1000 Da cutoff membrane until PLN precipitated (~12 hr). The suspension was centrifuged at 6370 x g for 20 min at 4 °C. The supernatant containing soluble proteins (MBP, TEV protease, uncleaved fusion protein) was discarded. Pellets were solubilized in 1-2 ml of 10% (w/v) SDS and stored at 4 °C. This crude solution was purified by reversed phase HPLC using an Agilent 1100 system (Agilent Technologies, Inc. Santa Clara, CA, USA) equipped with a Vydac 208TP C8 monomeric reversed phase column (250 mm × 1.0 mm i.d. × 10 μm particle size, Grace Vydac, Hesperia, CA, USA). The mobile phases used were: A – H_2O with 0.1% TFA and B – isopropanol. The column (incubated at 50 °C) was equilibrated with 10% solvent B and proteins were eluted at 2 ml/min flow rate using the following gradient: 10% to 30% solvent B in 10 min, 30% to 50% in 20 min, 50% to 70% in 30 min, and 70% to 100% in final 10 min. The column was re-equilibrated with 10% B for 10 min after each run. With these conditions the retention time for PLN was ~59 min. PLN fractions were pooled and isopropanol was evaporated under a stream of N_2. The resulting suspension was lyophilized and the resulting protein powder stored at -20 °C.

3.3.5 Quantitation of Protein

Protein concentration at each purification step was determined using protein absorbance at 280 nm, or assayed with densitometry measurements of Coomassie or silver stained gels **(Figure 3.1A)**. Densitometry data was collected on a Bio-Rad Molecular Imager FX using Bio-Rad Quantity One quantitation software. Recombinant protein concentrations were determined by comparison to a standard curve of 1, 2, and 3 μg synthetic PLN peptides previously quantified by amino acid analysis. PLN was also identified with MALDI-MS and amino acid sequence analysis.

3.3.6 Phosphorylation of PLN at S16 by PKA

HPLC-purified PLN was reconstituted to a concentration of 0.25 mg/mL for phosphorylation. 1 mg PLN was phosphorylated with 1000 U of protein kinase A catalytic subunit. Phosphorylation was confirmed using a gel-shift from a western blot with anti-pS16 PLN antibody 285 and by MALDI-TOF MS.

3.3.7 SERCA preparation

SERCA was extracted from rabbit skeletal muscle, purified and tested for activity as reported previously (113, 127, 140). A solution containing 0.45 mM of SERCA, 5 mM DPC, 1 mM CaCl2, 1 mM MgCl2, 20 mM MOPS, 20% glycerol, 0.25 mM DTT, 0.4 mM ADP, pH of 7.0 was used for titration experiments (see below).

3.3.8 Functional Assays

3.3.8.1 SERCA/PLN Co-reconstitution

Lyophilized PLN protein was solubilized in 240 μL of chloroform containing 2.4 mg of lipids in a 4:1 molar ratio of 1,2-dioleoyl-*sn*-glycero-3-phosphocholine (DOPC) and 1,2-dioleoyl-*sn*-glycero-3-phosphoethanolamine (DOPE). Samples were then dried by removing the organic solvent under a stream of N_2 gas. The dried film of lipid and PLN was then hydrated in 120 μL of 25 mM imidazole (pH 7.0) by vortexing followed by brief (30-60 sec) water-bath sonication. The lipid/PLN vesicles were then adjusted to contain a final concentration of 20 mM imidazole (pH 7.0), 0.1 M KCl, 5 mM $MgCl_2$, and 10% glycerol. 4.8 mg of β-octylglucoside was added, followed by 60 μg of purified SERCA with the final volume adjusted to 300 μL with buffer. Removal of the detergent was performed by incubation with 120 mg of wet Biobeads for 3 h at 25 °C. The

SERCA/PLN lipid vesicles were separated from Biobeads using a gel-loading tip and micropipette and immediately assayed for function.

3.3.8.2 ATPase Activity Measurements

SERCA activity was assayed by an enzyme-linked assay (144) performed in a 96-well plate. Each assay was performed at 37 °C in a Thermomax microplate reader (Molecular Devices) in triplicate at different free calcium concentrations in a total volume of 175 μL. Between 1 and 3 μg of SERCA was added to the samples to start the assay, and the absorbance of NADH was monitored at 340 nm to determine the rate of ATP hydrolysis. Data was plotted in Origin 7.5 and fit using the Hill Equation (see below) to determine the shift in pK_{Ca} (**Figure 3.3B).**

3.3.8.3 ^{31}P NMR Activity Assays

To measure the hydrolysis of ATP by SERCA under solution NMR conditions (DPC detergent micelles), assays were performed by monitoring the inorganic phosphate ^{31}P NMR signal. The assay mixture consisted of 6 μM SERCA, 137 μM PLN, assay mix, and concentrations of $CaCl_2$ required to reach free Ca^{2+} concentration calculated based on the method of Fabiato and Fabiato (145). Upon each addition of nucleotide, eight free induction decays (FIDs) were collected, each consisting of 16 single pulse transients on ^{31}P. Data were collected on a Varian Inova spectrometer operating at a ^{1}H Larmor frequency of 500 MHz. After monitoring the rate, the inorganic phosphate signal was normalized to the known amount of DPC in the sample. This normalized amount was then plotted (*V* vs pCa) and fit by the Hill equation (**Figure 3.3C**).

$$V = V_{\max} / [1 + 10^{n(pK_{Ca} - p_{Ca})}] \quad (1)$$

V is the initial ATPase rate and *n* is the Hill coefficient. The data were normalized to the maximal rate, V_{max}, which was obtained from the fit, and then replotted to determine the shift in pK_{Ca} **(Figure 3.3B).**

3.3.9 NMR Spectroscopy

3.3.9.1 Preparation of solution NMR samples and titrations.

NMR samples were prepared by dissolving isotopically labeled PLN in NMR sample buffer containing 300 mM DPC and 10% D_2O to a final concentration of 0.23 mM. For the preparation of wt-PLN NMR samples (or other “difficult” samples), a slightly

different procedure was used: wt-PLN was solubilized in 300 mM DPC, 20 mM PBS (pH 6.0) and 6 M guanindinum-HCl. The sample was dialyzed overnight in a mini-dialysis chamber against 1 L dialysis buffer. For the NMR titration, SERCA at a concentration of 0.51 mM was added incrementally to the PLN sample as previously reported (127). To correct for this dilution, and potential pH and salt effects, the same titration experiment was performed with SERCA buffer in the absence of enzyme. After each SERCA addition, a ^{1}H-^{15}N heteronuclear single quantum coherence (HSQC) experiment was collected on a Varian Inova spectrometer operating with a ^{1}H Larmor frequency of 600 MHz at 37 °C, using an inverse detection triple-resonance and triple-axis gradient probe. The HSQC pulse program was equipped with pulsed field gradients for both coherence selection and sensitivity enhancement (146).

3.3.9.2 K_d Measurements by NMR

For measuring the binding constants, we assumed 1:1 binding between SERCA and PLN, and that the intensity reduction ($I_{retention}$) of the transmembrane domain residues in **Figure 3.2C** was directly related to the fraction of PLN bound to SERCA (f_b). For a complete derivation of Eqn. 3 see ref. (113) (Eqns. 4-10).

$$f_b = 1 - I_{retention} \qquad (2)$$

$$f_b = \frac{K_d + [SERCA]_t + [PLN]_t - \sqrt{(K_d + [SERCA]_t + [PLN]_t)^2 - 4[SERCA]_t[PLN]_t}}{2[PLN]_t} \qquad (3)$$

The dissociation constant (K_d) was calculated using a non-linear fit to Eqn. 3.

3.3.9.3 Preparation of Oriented Samples and Solid-State NMR spectroscopy

PLN was reconstituted into lipid vesicles using two different preparations: 1) detergent mediated reconstitution and 2) organic solvent mediated reconstitution.

> *3.3.9.3.1 Detergent mediated reconstitution*: 80 mg (4/1, w/w) of DOPC/DOPE were dissolved in chloroform and thoroughly vortexed. Chloroform was evaporated under a stream of N_2, after which the lipids were resuspended in 40 mL of ddH_2O. The lipid suspension was sonicated on ice until small unilamellar vesicles (SUVs) formed (the suspension became transparent). After sonication, the lipids were centrifuged (6,370 x g for 10 min at 4°C) to remove bigger vesicles and metal particles. PLN (~4 mg) was solubilized in 1 mL of SDS (10%, w/v) and dissolved in the lipid mixture prior to one freeze-thaw cycle. Samples

were extensively dialyzed against ddH_2O to remove the detergent and subsequently concentrated to 2 ml using an ultrafiltration device (10 kDa cutoff membrane). Approximately 100 µL of sample were transferred onto each of 20 glass plates. Samples were slowly dried at 40 ºC, rehydrated to the liquid-crystalline phase and finally sealed in a rectangular glass cell.

3.3.9.3.2 Organic solvent mediated reconstitution: DOPC/DOPE 80 mg (4/1, w/w) were dissolved in chloroform and thoroughly mixed. PLN (~4 mg) was solubilized in 50 µL of trifluoroethanol and added to the lipid mixture. Solvents were first evaporated under a stream of N_2 and then lyophilized overnight to ensure complete removal of organic solvents. The lipid/protein mixture was resuspended in 40 mL of ddH_2O and carefully vortexed. Small unilamellar vesicles were prepared by repeatedly extruding the lipid mixture through polycarbonate filters of decreasing pore size (200, 100, 50 µm) using a bench-top extruder. This SUV suspension was concentrated to 2 ml with samples dried and rehydrated as reported above. The final molar ratio of lipid/protein for all samples was ~200/1.

3.3.9.3.2 NMR Spectroscopy: The 2D polarization inversion spin exchange at the magic angle (PISEMA) was performed (112, 147) with TPPM decoupling during acquisition (148). Due to spectrometer limitations (lack of fast frequency switching), a phase modulated Lee-Goldberg (PMLG) was used in the indirect dimension to decouple ^{1}H-^{1}H interactions and allow for the evolution of ^{1}H-^{15}N dipolar coupling (149). The initial 90° ^{1}H pulse, cross-polarization, PMLG (^{1}H effective field), and TPPM decoupling during acquisition were applied at ~60 kHz RF field strength. Spectra of uniformly ^{15}N samples were acquired with 1 k scans and 30 t_1 increments while selectively labeled samples required 4-12 k scans and ~8-16 increments. All experiments were performed at the National High Magnetic Field Laboratory at a 14.1 T magnetic field strength (^{1}H frequency of 600.1 MHz) equipped with a Bruker DMX spectrometer using a low-E probe built by the RF program (150).

3.3.10 Structure Determination of monomeric and pentameric PLN using hybrid-solution and solid-state NMR method

Solution and solid-state NMR methods have been used as a complementary approach to the structure determination of small and medium size membrane proteins (151, 152). For solution NMR, the proteins are reconstituted in detergent micelles with a meticulous choice of experimental conditions, which is based on the NMR spectral features as well as preservation of SERCA function. For solid-state, we reconstitute membrane proteins in synthetic lipid bilayers, which are more amenable to enzyme function. The major advantage of solution NMR is to offer high-resolution spectra (membrane proteins up to hundreds of kDa have now been studied and assigned) and to obtain secondary and tertiary structures through NOE measurements. On the other hand, when membrane proteins are solubilized in detergent micelles, the topological information of the protein within the lipid bilayer is lost. This orientation information regarding the molecular topology can be recovered by solid-state NMR measurements using aligned samples.

Recent reports verify that the protein adopts a similar structure in both lipid bilayers and micelles; therefore, we decided to pool the information derived from these two techniques and combine the structural restraints into a unique molecular modeling protocol (4, 5). The total potential energy function (E_{Total}) is defined as a combination of an empirical energy function (E_{chem}) and two penalty functions that include solution (E_{solNMR}) and solid-state NMR (E_{ssNMR}) restraints (4):

$$E_{Total} = E_{chem} + E_{solNMR} + E_{ssNMR} \quad (4)$$

Where

$$E_{chem} = E_{bonds} + E_{angles} + E_{torsion} + E_{improper} + E_{vdw} \quad (5)$$

$$E_{solNMR} = E_{NOEs} + E_{CDIH} + E_{HBOND} + E_{RDC} + E_{PRE} + E_{CSP} \quad (6)$$

$$E_{ssNMR} = E_{CSA} + E_{DC} \quad (7)$$

The energy terms of E_{chem} are included into standard force field of XPLOR-NIH (153). E_{ssNMR} contains dipolar coupling and chemical shift anisotropy values derived from PISEMA or HETCOR experiments. As a result, the simulated annealing protocol minimizes the energy function for both distance and angular restraints as well as orientational restraints derived from solid-state NMR PISEMA experiments. **Figures 3.3D** shows the average structures from the lowest energy conformational ensembles for both the monomer (5).

3.4 CONCLUSIONS

3.4.1 Allosteric Model of SERCA Regulation by PLN

The outcomes of our investigation are summarized within the schematic in **Figure 3.4**. In agreement with both *in vitro* and *in vivo* studies, we found that PLN adopts a pentameric, L-shaped conformation both in micelles and in lipid bilayers. In particular, both solution and solid-state NMR data show that the cytoplasmic domain (which is amphipathic) interacts with the surface of the membrane mimicking environment (both for micelles and lipid bilayers), while the transmembrane domain form a tight hydrophobic bundle stapled together by a leucine-isoleucine zipper. PLN depolymerization into active monomers occurs in the presence of SERCA. In the monomeric state (prelude to the interaction with SERCA), PLN is predominantly in a resting T state with a small population in the R state. Using EPR spectroscopy, Thomas and co-workers have estimated that ~10% of PLN exists in the R state in lipid bilayers at 4 °C (38). In the presence of SERCA, the equilibrium is shifted toward the R state that is probably selected to bind the enzyme. Although dynamic in nature, PLN forms a stable inhibitory complex with SERCA (K_d in DPC detergent micelles ~60 μM). This inhibition is reversed by phosphorylation at S16, which changes the conformational dynamics and results in an unwinding of the cytoplasmic helix (22). In the presence of SERCA, phosphorylation at S16 PLN causes a slight rearrangement within domain Ib (residues 23-30) and changes the dynamics at the binding interface (38, 102). These structural dynamics affect the conformational transitions of the enzyme, and ultimately calcium translocation.

3.4.2 Rational Design of PLN Mutants as Possible Candidate for Gene Therapy

A fundamental aim of structural biology is to move from understanding structure and dynamics to controlling molecular function. With this in mind, we attempted to manipulate the structural dynamics of PLN and to promote the formation of the R state through mutagenesis. Recently, we found that by mimicking the S16 phosphorylated state of PLN (i.e. enhancing the local dynamics in the hinge region) it is possible to tune the extent of SERCA inhibition (25). This work was originally inspired by *in vivo* studies carried out by Chien and co-workers, who demonstrated that a pseudo-phosphorylated variant of PLN can relieve SERCA inhibition and increase heart contractility, ultimately reversing the damages of myocardial infarction. We found that by changing Pro21 to Gly it is possible to generate a *loss-of-function* mutant with characteristics similar to S16E (pseudo-phosphorylated species tested by Chien), preserving the posttranslational control by β-adrenergic stimuli (25). This new generation of mutants possesses

a *residual inhibitory power* that could be important in adjusting the pathophysiology of diseased hearts leading to reversal or hindrance of cardiac remodeling. We are currently working on different sites to improve the characteristic of *loss-of-function* mutants.

3.5 NOTES

3.5.1 For small membrane peptides, choice of fusion partner and cleavage protease can be crucial for successful expression and purification. Expression of small membrane peptides can induce inclusion bodies, or lead to cell death. We attempted cloning PLN with several other fusion partners and found MBP to offer the best degree of solubility and expression levels. For choosing a cleavage protease, scanning for secondary cleavage sites is also very important. For PLN, cleaving with thrombin and other proteases led to secondary cleavage. TEV has a longer recognition sequence (7 residues), making it very specific.

3.5.2 TEV can be easily expressed in *E. coli* and purified using a 6x-His and Ni-NTA resin chromatography within the laboratory. A construct of TEV that is particularly effective which we use is a S219V mutant with a poly-arginine tail kindly provided to us by the Gorelick Laboratory.

3.5.3 The method of unfolding the protein sample with guanidine HCl and refolding via dialysis used to prepare the wt-PLN solution state NMR samples described in section 3.4.1 is useful for other membrane protein NMR samples that are prone to aggregation or those which give non-uniform HSQC spectra. We have found that other “difficult” samples (such as pS16 PLN) give better spectra when prepared in this manner.

3.5.4 This work was supported by grants to G.V. from the National Institutes of Health (GM64742, HL80081, GM072701) and NJT (AHA 0515491Z). PISEMA spectra were acquired at the NHMFL, Tallahassee, FL (DMR-0084173). NMR instrumentation at the University of Minnesota High Field NMR Center was funded by the National Science Foundation (BIR-961477) and the University of Minnesota Medical School.

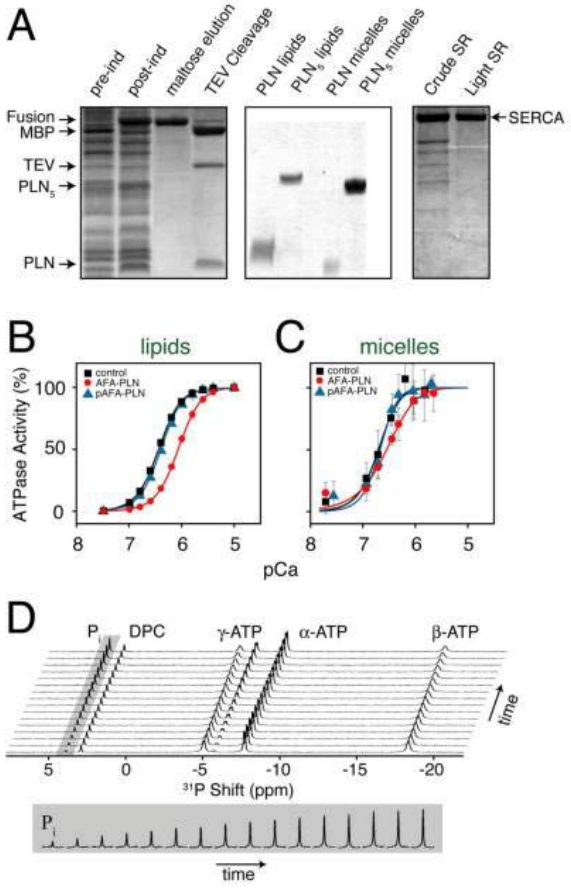

Figure 3.1. Purification and functional assays of PLN and SERCA. (**a**) Purification gels showing expression of fusion protein (before and after induction with IPTG), selection on amylose affinity column, and cleavage by TEV protease (*left gel*). *Middle gel* shows PLN monomer and pentamer reconstituted in DOPC/DOPE lipid bilayers and DPC detergent micelles. *Right gel* shows purification of SERCA from crude SR; light SR refers to purified SERCA used for activity assays and NMR experiments. (**b**) Normalized SERCA activity in the absence (*squares*) and presence of PLN (*circles*), and in the presence of phosphorylated PLN at S16 (*triangles*). This activity assay was performed in lipid bilayers using the coupled enzyme assay in a microplate reader. (**c**) SERCA activity monitored using ^{31}P NMR spectroscopy in DPC micelles. (**d**) Example of the ^{31}P NMR activity assay where the inorganic phosphate signal (*highlighted* in *gray*) is monitored as a function of time. *Middle gel* in (**a**) is reproduced with permission from ref. (107) Copyright 2007 National Academy of Sciences, USA. *Panel* (**b**) is reproduced with permission from ref. (142) Copyright 2008 American Chemical Society. *Panels* (**c**, **d**) are reproduced with permission from ref. (102) Copyright 2006 Elsevier.

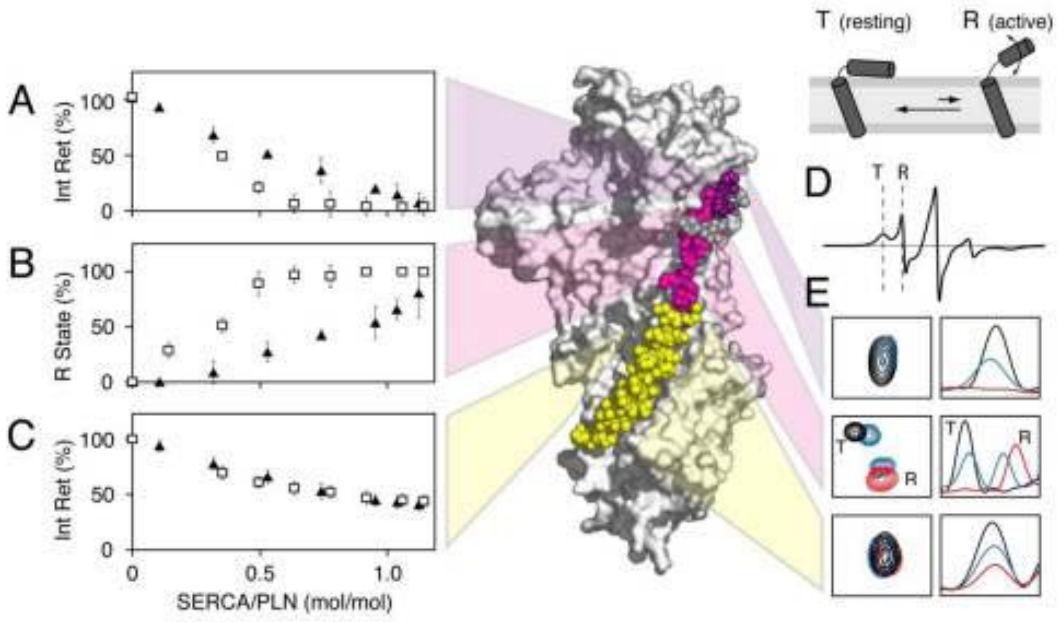

Figure 3.2. Solution NMR results on AFA-PLN/SERCA complex in detergent micelles. A) The intensity retention plotted for residues 2, 3, 6, and 8 in p16 PLN (white) and PLN (black) that disappear with increasing additions of SERCA. B) The percentage of PLN in the R state as a function of the SERCA/PLN molar ratio for p16 PLN (white) and PLN (black) for residues undergoing slow exchange (residues 10–12, 15–17, and 22). A value of 100% indicates that the peak (residue) has completely exchanged to the R state. C) The intensity retention for residues in the transmembrane domain (28–52) that decrease, but do not abolish in intensity. D) EPR spectrum of TOAC labeled A11 PLN in lipid bilayers in the absence of PLN. Since EPR probes a faster timescale, both the T and R states are observed in lipids. E) representative 1D and 2D spectra of the residues with abolished intensity (top, corresponds to A), residues undergoing slow exchange (middle corresponds to B), and residues with reduced intensity (bottom, corresponds to C). Coordinates for the PLN/SERCA molecular model were generously provided by Drs. MacLennan and Toyoshima. Panels A-C and E were adapted with permission from Ref (102). Copyright 2006 Elsevier. Panel D was reproduced with permission from Ref (127). Copyright 2005 National Academy of Sciences USA.

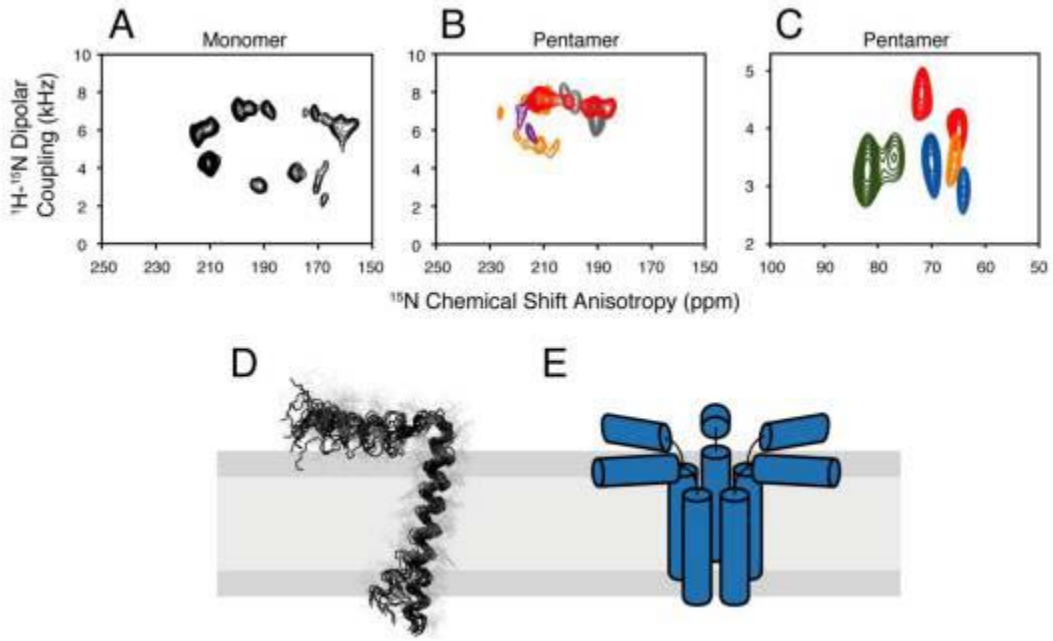

Figure 3.3. Solid-state NMR spectra with overlaid ensemble PLN structures. PISEMA spectra for uniformly ^{15}N labeled PLN monomer (A) and selectively labeled PLN pentamer (B, transmembrane domain residues; C, cytoplasmic domain residues). Note that dipolar coupling values within the spectra are scaled by the theoretical 0.82 factor for the PISEMA experiment (112). Panel D shows the overlay of the structural ensemble for monomeric PLN determined using a hybrid of solution and solid-state NMR restraints (PDB 2KB7) (5). Panel E shows a cartoon representation of the PLN pentamer indicating the pinwheel assembly (107). Panels A-C are reproduced with permission from refs. (5, 107). Copyright 2007 and 2009 National Academy of Science USA.

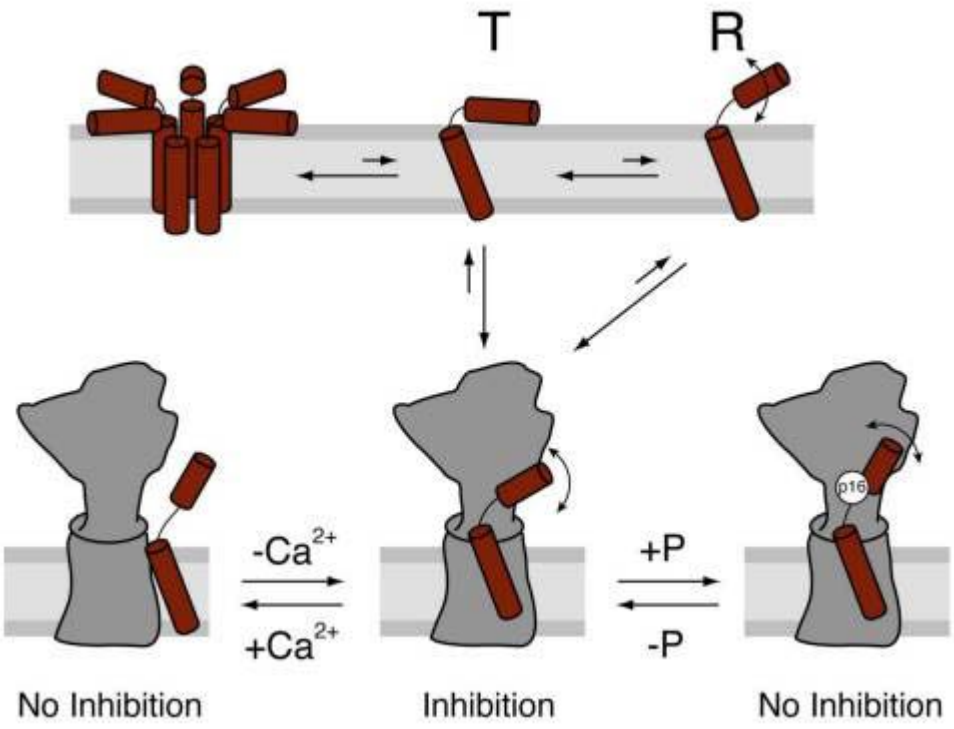

Figure 3.4 Allosteric model of PLN/SERCA interaction showing depolymerization of pentameric PLN into monomeric units that undergo exchange between an ordered T state and a disordered R state(s) (38, 102, 127, 141, 142).

Chapter 4

Controlling the Inhibition of the Sarcoplasmic Ca^{2+}-ATPase by Tuning Phospholamban Structural Dynamics

Kim N. Ha,[1] Nathaniel J. Traaseth,[1,2] Raffaello Verardi,[1] Jamillah Zamoon,[1] Alessandro Cembran,[2] Christine B. Karim,[1] David D. Thomas,[1] and Gianluigi Veglia[1,2]

[1]*Department of Biochemistry, Molecular Biology and Biophysics and* ,[2]*Department of Chemistry, University of Minnesota*

Reprinted with permission from Journal of Biological Chemistry, Vol. 282. Issue 151, pp. 37205-14

4.1 INTRODUCTION

Calcium translocation is a major signaling mechanism for mammalian cells (154). In cardiac myocytes, calcium regulates contractility and relaxation through a "calcium induced calcium release" cycle (12, 155, 156). At low concentrations, calcium ions enter the myocytes through voltage-dependent L-type calcium channels that are embedded in the sarcolemmal-sarcoplasmic reticulum (SR) junctions, acting as a trigger for the release of calcium ions by the ryanodine receptors. Subsequently, free intracellular calcium ions bind the myofilaments, initiating muscle contraction. Relaxation of the muscle fibers occurs when calcium ions dissociate from the myofilaments and are transported out of the cytosol into the SR vesicles, a process that is primarily controlled by SR Ca^{2+}-ATPase (SERCA) and phospholamban (PLN) (13, 14, 157).

SERCA (a 110 kDa integral membrane enzyme) transports two calcium ions into the SR by hydrolyzing one molecule of ATP (131, 134). This ATP-driven calcium pump has a large cytoplasmic region (divided into actuator, nucleotide-binding, and phosphorylation domains) and a transmembrane domain that constitute the calcium channel (94, 134) (**Figure 4.1**).

PLN, a single-pass transmembrane protein, is the endogenous inhibitor of SERCA in the cardiac muscle (13). PLN has three structural domains: cytoplasmic helix (domain Ia, residues 1-16), loop (residues 17-21), and transmembrane helix, which was further divided into two dynamic domains (domain Ib, residues 22-31, and domain II, residues 32-52). Proline 21, situated in the dynamic loop, breaks the helicity of the transmembrane domain, determining the *L-shaped* topology of both monomeric and pentameric PLN in lipid bilayers (**Figure 4.1**) (57, 102, 107, 111).

Growing evidence suggests that PLN acts as a subunit of SERCA (141), with its transmembrane helix bound in the hydrophobic groove between transmembrane domains M2, M4, M6, and M9 of the enzyme and its cytoplasmic helix interacting with the cytoplasmic domains of SERCA (98) (**Figure 4.1**). β-adrenergic stimuli activate protein kinase A (PKA), resulting in PLN phosphorylation at S16 (pS16-PLN) with complete relief of inhibition and restoration of the calcium flux into SR vesicles (13). S16 phosphorylation is necessary and sufficient to relieve the inhibitory effect of PLN (80, 158), although T17 and S16/T17 double phosphorylation are also present in intact myocardial tissue (159, 160).

Defective cellular calcium handling by the SERCA/PLN complex is responsible for the progression of heart failure (14). In fact, aberrant mutations in the PLN primary sequence have been directly linked with specific heart conditions. R9C mutation, R14 deletion, and L39

truncation of PLN have been detected in patients affected by dilated cardiomyopathy (DCM) (28, 30, 31). One promising therapeutic strategy is to augment cardiac contractility by inducing a positive inotropic effect, targeting PLN function directly (i.e., reducing its inhibitory effects) (161). This can be accomplished by a) decreasing PLN's expression level, b) increasing phosphorylation of PLN, c) using PLN inhibitors that interfere with the SERCA/PLN complex formation (e.g. quercitin, tannin, and ellagic acid), or d) using mutants with dominant negative effects, loss-of-function (LOF) mutants, that compete with endogenous wild-type PLN (32). This last approach has received significant attention after the success of Chien and co-workers in the design and delivery of a pseudo-phosphorylated mutant of PLN (S16E-PLN). Using a new recombinant adeno-associated virus vector (rAAV), these researchers were able to reverse the effects of progressive dilated cardiomyopathy (32, 133). In particular, they showed that expression of S16E-PLN in animal models with chronic heart failure and DCM as well as with post-cardiac infarction resulted in a substantial increase of both cardiac diastolic and systolic functions (86). More recently, using percutaneous cardiac recirculation-mediated gene transfer with S16E-PLN, the Power and Chien groups demonstrated the reversal of heart failure progression even in large animals (33).

Prompted by the success of the S16E-PLN mutant, we began our structural investigation of PLN mutants with a view toward rational design of improved LOF mutants. Previous mutagenesis studies (34, 125) gave invaluable insight into PLN function. However, they did not distinguish whether a point mutation causes changes in the interaction surface between SERCA and PLN, in PLN structural dynamics, or both. As a consequence, rational designs of single or double mutations with increasing or decreasing inhibitory effects have been quite difficult to achieve (19, 130, 162). From these studies, Young and coworkers concluded that the inhibitory properties of each amino acid are context-dependent (35).

For our rational design of mutants, we postulated that by manipulating PLN structural dynamics it could be possible to regulate SERCA's function. This hypothesis is substantiated by a compilation of studies that we have carried out in the last few years on PLN (phosphorylated and unphosphorylated) free and bound to SERCA and culminated in the formulation of the allosteric mechanism of regulation of SERCA by PLN(13, 35-37). This model assumes that PLN exists in a dynamic equilibrium between T and R states, with SERCA shifting the equilibrium toward the R state prior to forming the inhibitory complex. Phosphorylation at S16 affects PLN structural dynamics and, in turn, the allosteric equilibrium, causing the formation of the non-inhibitory SERCA/PLN complex (38, 102, 105, 127).

In this paper, we demonstrate that it is possible to tune PLN structural dynamics and mimic PLN phosphorylation to gain control of SERCA's function. As proof of concept, we present a new PLN mutant, P21G-PLN, with improved *in vitro* characteristics with respect to S16E-PLN for a possible use in rAAV gene therapy.

4.2 EXPERIMENTAL PROCEDURES

4.2.1 NMR Sample Preparation

^{15}N-labeled monomeric PLN mutants were expressed as a fusion protein with maltose binding protein and purified as described previously (101). Primer synthesis and DNA sequencing were performed at the BioMedical Genomics Center of the University of Minnesota. Sequences of the forward and reverse primers consisted of the optimized codons for *E. coli* for 3 residues before and after the target residue to be mutated. Polymerase chain reaction (PCR) was performed with a total volume of 50 μL containing 0.06 μM of each oligonucleotide, 80 μg of parental template, 200 μM dNTP mix (Promega), 10x buffer (10 μL per reaction), and 5.0 U Pfu Turbo DNA polymerase (Stratagene). PCR was carried out in a Perkin-Elmer GeneAmp PCR system 2400 at 95 ºC for 3 minutes followed by 16 temperature cycles of 95 ºC for 15 seconds to denature the DNA, 55 ºC for 1 minute to anneal, and 68 ºC for 12 minutes to elongate. PCR products were then digested with Dpn-I (Stratagene) in order to remove non-mutated methylated dsDNA. After digestion, the products were transformed into XL-1 Blue competent cells (Stratagene) and grown on Luria Bertani medium (LB)/ampicillin plates. DNA purification was performed with Quick-Spin Minipreps (Qiagen). The purified DNA was quantitated by measuring the UV absorption. DNA sequencing confirmed the single site mutations on the PLN background. Purified plasmid constructs were then transformed into the BL21 (DE3) strain of *E. coli* and protein purification was performed as previously described (101). Phosphorylation at S16 by protein kinase A of the P21G mutant was performed as previously described (105). NMR Samples were prepared by dissolving the lyophilized proteins (PLN, P21A, S16E, P21G, P21L, P21I, S16EP21G, pS16 PLN, pS16-P21G) in 300 μL phosphate buffered saline solution, pH 6.0, containing 300 mM dodecylphosphocholine (DPC) (Avertec) and 10% D_2O. The protein final concentration in the NMR samples was ~0.25 mM as estimated by gel densitometry.

SERCA was extracted from rabbit skeletal muscle, purified and tested for activity as reported previously (102, 127). A solution containing 0.45 mM of SERCA, 5 mM DPC, 1 mM CaCl2, 1

mM MgCl2, 20 mM MOPS, 20% glycerol, 0.25 mM DTT, 0.4 mM ADP, pH of 7.0 was used for titration experiments (see below).

4.2.2 NMR Experiments

NMR experiments were carried out on a 600 MHz Varian INOVA spectrometer operating at ^{1}H Larmor frequency of 600.13 MHz and equipped with an inverse detection triple resonance and triple axis probe. All of the experiments were performed at 37° C. [^{1}H,^{15}N] heteronuclear single quantum coherence (HSQC) spectra (48) were acquired with 6000 Hz spectral width in the direct dimension (^{1}H) and 1500 Hz in the indirect dimension (^{15}N). 1024 and 128 complex points were collected for the direct and indirect dimensions, respectively. 2D data were processed to a final matrix size of 2048 x 256 after zero filling and Fourier transformation. Resonance assignments for all the mutants were carried out using a combination of 3D [^{1}H,^{15}N] TOCSY-HSQC (70 ms mixing time) and [^{1}H,^{15}N] NOESY-HSQC (70 ms mixing time) experiments (47, 51). The 3D experiments were acquired with 6000 Hz spectral width in both ^{1}H dimensions and 1500 in the ^{15}N dimension. The 3D matrices were acquired with 1024x160x80 complex points with 2048x320x160 after final processing. The recycling delay used was 1.2 s for all of the experiments. Data processing was carried out using NMRPipe software (163). The secondary structure was assessed using Hα chemical shift index (CSI), which is the difference between the PLN Hα chemical shifts and those from random coil values (45). Because of the high rotational anisotropy of PLN and its mutants, the analysis of the order parameters (the customary index for protein internal dynamics, ps-ns timescale) does not give good convergence; therefore, we limited our analysis to heteronuclear NOE data (22). [^{1}H,^{15}N] steady-state NOE enhancement experiments were acquired using standard pulse sequences based on Farrow et al. (1994) (79) using a spectral width of 6000 Hz in ^{1}H, 1500 Hz in ^{1}H with 1024 points collected in the direct (^{1}H) dimension and 64 points collected in the indirect (^{15}N) dimension. For the saturated spectrum, a 3 sec ^{1}H presaturation period was used. Peak intensities were analyzed and quantified using NMRView software (164).

4.2.3 Analysis of the correlations between mutations and structural dynamics

The local and long-range perturbations caused by each mutation (or phosphorylation) on the structural (CSI) and dynamical (NOE) properties (P) of PLN were analyzed for each residue by computing the correlation coefficients (ρ_{PM}) between the property P and each mutation M (165):

$$\rho_{PM} = \frac{\sum_{i=1}^{n_M}\left[\left(P_i - \mu_P\right)\left(M_i - \mu_M\right)\right]}{\left(\sigma_P \sigma_M\right)}$$

where μ and σ are the average values and standard deviations for *P* and *M*, respectively, and n_M is the total number of species. To assign *M*, we ordered the different PLN mutants based on increasing average NOE values for residues 17 to 30, corresponding to the loop and domain Ib. The heteronuclear NOEs for the specified range change from 0.50 to 0.69 in the following order: pS16-PLN< pS16-P21G < P21G < PLN < P21A < P21I < P21L. Then the incremental values of the heteronuclear NOE across the species were associated to the variable *M* for a total of 7 samples (n_M=7). In the histogram of **Figure 4.3** we report all the correlations calculated. The gradation of gray in the figures indicates the relevance of each correlation. Meaningful correlations respond to the following criteria: a) have an absolute value much greater than the corresponding error (greater than one standard deviation, and b) show a significant change in CSI (>0.05 ppm) or heteronuclear NOE (>0.1). Given the small sample size (n_M=7), the errors are computed using the nonparametric bootstrap calculated with the R software package (http://www.R-project.org) with a number of bootstrap samples of 200.

4.2.4 NMR titrations of PLN mutants with SERCA: determination of K_d and T to R transitions

NMR titration were carried out monitoring the chemical shifts of the amide fingerprint regions of PLN variants using [^{1}H,^{15}N]-HSQC experiments. A total of 13 different experiments were acquired after each SERCA addition up to a final molar ratio of 1:1 (SERCA:PLN). The K_d values were determined by following the disappearance of the resonances corresponding to the transmembrane domains of PLN upon addition of incremental amounts of SERCA as described previously (102, 127). Assuming 1:1 ratio between SERCA and PLN, the intensity reduction ($I_{retention}$) of transmembrane domain residues is directly related to the fraction of PLN bound to SERCA (f_b),

$$f_b = 1 - I_{retention}$$

Then $I_{retention}$ is correlated to a dissociation constant (K_d) through the following derivation (102, 127).

$$f_b = \frac{[PLN\text{-}SERCA]}{[PLN]_f + [PLN\text{-}SERCA]}$$

$$K_d = \frac{[PLN]_f [SERCA]_f}{[PLN\text{-}SERCA]}$$

$$[SERCA]_t = [SERCA]_f + [PLN\text{-}SERCA]$$

$$[PLN]_t = [PLN]_f + [PLN\text{-}SERCA]$$

$$K_d = \frac{[SERCA]_t - f_b([PLN]_t - [SERCA]_t) + f_b^2[PLN]_t}{f_b}$$

Taking the negative quadratic solution, the fraction bound is:

$$f_b = \frac{K_d + [SERCA]_t + [PLN]_t - \sqrt{(K_d + [SERCA]_t + [PLN]_t)^2 - 4[SERCA]_t[PLN]_t}}{2[PLN]_t}$$

Finally, the K_d values were calculated using a best-fit non-linear regression of Eqn. 8. The transitions from T to R state for each mutant were quantified by following the disappearance of the T state and the appearance of R state in the [^{1}H, ^{15}N]-HSQC spectra (102, 127). The percent of R state was then plotted as a function of the SERCA:PLN molar ratio. The resulting curves were fitted using the Hill equation. Hill coefficients were used to estimate the degree of cooperativity of each construct. Buffer titrations (PLN titrations with SERCA buffer only) were used as a control to account for the effects of dilution to peak intensity and chemical shifts (102, 127).

4.2.5 Preparation of EPR samples

PLN and mutants were prepared with the spin-labeled amino acid 2,2,6,6-tetramethylpiperidine-1-oxyl-4-amino-4-carboxylic acid (TOAC) substituted for A11, using solid-phase peptide synthesis, as reported previously (128, 166). Unlike conventional spin labels attached flexibly to cysteine side chains, this spin label couples the nitroxide moiety rigidly to the alpha carbon, providing direct detection of peptide backbone dynamics. This spin label has no effect on PLN function (128). Phosphorylation of spin-labeled PLN at S16 was accomplished as described previously (38). For EPR experiments, TOAC-PLN was reconstituted into lipid vesicles containing DOPC/DOPE (4:1, 200 lipids per PLN). EPR experiments were conducted in low Ca (pCa 6.5) buffer (50mM KCl, 5mM $MgCl_2$, 0.5mM EGTA, 210μM $CaCl_2$, 50mM MOPS, pH 7.0), where the inhibitory effect of PLN is maximal.

4.2.6 EPR Experiments on PLN in lipid bilayers

EPR spectra were acquired using a Bruker EleXsys 500 spectrometer with the SHQ cavity. Samples (20 μL in a 0.6 mm i.d. quartz capillary) were maintained at 4ºC using the Bruker temperature controller with a quartz dewar insert. The field modulation frequency was 100 kHz, with a peak-to-peak amplitude of 1 G. The microwave power was 12.6 mW, producing moderate saturation (so that signal intensity was at least 50% of maximum) without significant effect on the spectral lineshape. Spectra were analyzed in terms of peptide backbone rotational dynamics and mole fractions of two resolved conformations using computational simulation as described previously (38).

4.2.7 Activity Assays

The inhibitory potency of PLN and its mutants was measured in lipid bilayers (EPR conditions). To measure activity in membranes, each PLN mutant was co-reconstituted in lipid bilayer membranes (DOPC:DOPE 4:1) with purified SERCA at molar ratios of 10:1 SERCA:PLN and 700:1 lipids/SERCA. The calcium dependence of the ATPase activity was measured at 25 °C using coupled enzyme assays (167). The consumption of NADH was monitored by the decrease in its absorbance at 340 nm using a Spectromax microplate reader (Molecular Devices). The initial ATPase rate V was measured as a function of pCa (calculated as described previously), and the data were fit using the Hill equation,

$$V = V_{max} / [1 + 10^{\,n\,(pKCa - pCa)}]$$

to determine V_{max} , pK_{Ca} (the pCa value when $V = V_{max}/2$), and n (Hill coefficient). V_{max} was obtained from the fit, and the data were plotted as V/V_{max}.*vs* p*Ca*. Since the maximal velocity is not reproducible for the SERCA/PLN complex, we used the pK_{Ca} values to quantify the inhibition caused by PLN mutants.

4.3 RESULTS

4.3.1 NMR structural dynamics of PLN mutants

Our central hypothesis is that PLN regulates SERCA through an allosteric mechanism (127)**.** According to this mechanism, free PLN exists in a dynamic equilibrium between T and R states, where the T state is the predominant *L*-shape topology and the R state is more dynamic. SERCA selects and binds the R state. Phosphorylation at S16 by protein kinase A reverses PLN inhibition. This single phosphoryl transfer introduces a negative charge in the cytoplasmic

domain, partially unwinding the helix, increasing its ps-ms dynamics, and promoting the transition from the T to the R state. This order-to-disorder transition causes the disruption of the SERCA/PLN interaction surface (102, 105). Can mutations mimic the effects of phosphorylation?

To answer this question, we designed a series of PLN mutants with a gradation of helicity and structural rigidity. These mutagenesis studies were carried out on monomeric PLN in which the three non-essential cysteines 36, 41, and 46 were mutated into Ala, Phe, and Ala (126). The monomeric species is biologically relevant for two reasons: first, it has been shown that monomeric PLN is the inhibitory species (19, 168), and second, it retains the same activity as wild-type PLN (126).

As a starting point for our mutagenesis studies, we chose P21, a pivotal residue that breaks the transmembrane helix of PLN, determining its *L-shaped* conformation (57) and the dynamic partition into four dynamic domains: domain Ia, loop, domain Ib, and domain II (**Figure 4.1A**) (22). Nuclear spin relaxation measurements revealed that P21 bridges the two most dynamic regions: loop and domain Ib (**Figure 4.1A**). The new mutants were designed using JUFO (169) and PrDOS (www.prdos.hgc.jp) software packages that predict both secondary structure and dynamics based on protein primary sequences. From the JUFO and PrDOS scores, we selected the following mutants with increasing propensity to form a continuous, more rigid helix throughout the entire PLN sequence: P21G< P21A< P21I< P21L.

We probed the structural dynamics of the different mutants reconstituted in dodecylphosphocholine (DPC) micelles, a membrane mimicking system that preserves SERCA activity (127). Using a combination of [^{1}H,^{15}N] TOCSY and NOESY (47, 51) spectra and [^{1}H-^{15}N] heteronuclear NOE experiments (79), we assessed both the secondary structures and internal dynamics of all of the mutants. Specifically, we use Hα CSI, an indicator of protein secondary structure (45) and heteronuclear NOE values to probe PLN backbone ps-ns dynamics (170). The CSI for the H_{α} protons and the [^{1}H,^{15}N] heteronuclear NOE values for all the mutants are reported in **Figure 4.2**.

The red and black traces correspond to unphosphorylated (inhibitory form) and phosphorylated (non-inhibitory form) PLN that we have previously published (22, 105). These are shown in each panel to guide the reader. Visual inspection reveals a gradation of structural dynamics of PLN mutants going from the most flexible and least helical P21G to the most rigid and helical P21L. However, to rationalize the effects of the point mutations on the structural dynamics, we analyzed our data using a correlation function as described in the Experimental

Procedures. **Figure 4.3** shows the correlation plots for CSI and heteronuclear NOE for all of the different mutations.

In black are those residues with an absolute value of the correlation coefficient greater than one standard deviation and in dark-gray are those between two and three standard deviations. In addition, the extent of the variations of CSI and heteronuclear NOE are indicated on top of the most significant residues. A negative correlation (or anticorrelation) for the CSI graph in **Figure 4.3A** indicates that moving from P21G to P21L the resonance for a given residue shifts upfield (the residue becomes more helical), a positive correlation indicates a correlated shift downfield toward random coil values. As expected, the residues adjacent or in the immediate proximity of the mutated site show strong anti-correlations (see residues 18, 19 and 20). Interestingly, residue 27 (and to a lesser extent residue 30) exhibits a noticeable positive correlation or decrease in helical content. Note that these residues are neighbors to Q26, which we identified as the bridgehead between the cytoplasmic and the transmembrane domains and is responsible for the transmission of the phosphorylation signal at S16 down to the membrane-embedded region (102). **Figure 4.3B** displays the correlations between the heteronuclear NOE values versus residue number as a function of the different mutations. In this case, a positive correlation indicates that mutations at P21 increase the residue rigidity, while an anti-correlation indicates that the residue becomes more dynamic. Most of the residues in the loop and domain Ib show positive correlations, while smaller anti-correlations are present for residue 37 and 46. Overall, mutations at position 21 induce both short- and long-range effects.

4.3.2 *Structural Dynamics of S16E-PLN*

The analysis of the CSI and heteronuclear NOE plots indicates that the strength and the dynamics of the cytoplasmic helix of this mutant are intermediate between those of P21G and P21A mutants (**Figure 4.2**). The CSI of the S16E mutant has a profile similar to that of PLN for both domains Ib and II, while showing significant differences from E2 to M20. The heteronuclear NOE values also follow this trend, showing values that are intermediate between the unphosphorylated and phosphorylated forms of PLN. Therefore, the structural dynamics of S16E pseudo-phosphorylated mutant of PLN is similar but not identical to that of pS16-PLN.

4.3.3 *EPR of selected mutants in lipid bilayers*

In order to test whether the effects of PLN mutation on dynamics in DPC micelles are similar to those observed in lipid environment, we carried out EPR experiments on selected TOAC-spin-labeled PLN reconstituted into lipid bilayers (**Figure 4.4**), of the same lipid composition used to

measure functional regulation of SERCA by PLN. In all four PLN variants tested, the EPR probe, reporting the backbone dynamics at position 11 in the cytoplasmic domain, shows clear evidence for two resolved states, a broad component corresponding to the ordered T state, and a narrow component corresponding to the dynamically disordered R state (128). The vertical dashed lines in **Figure 4.4** show that the spectral line positions, thus the rotational dynamics, of the T and R states are essentially unaffected by phosphorylation or mutation. Therefore, the principal effect observed is a change in the distribution (i.e. mole fractions) between the two states.

Phosphorylation at S16 induces a dramatic increase in the mole fraction in the R state, at the expense of the T state, while the S16E mutation produces an intermediate effect (**Figure 4.4**, top) and the P21A mutation produces an opposite effect – decreasing the mole fraction in the R state (**Figure 4.4**, bottom). Thus, the effects of mutation on these conformational transitions are consistent with the NMR observations in DPC micelles (**Figure 4.2**).

4.3.4 Structural Dynamics-Function correlations: Effects of mutations on SERCA activity

In order to characterize the functional effects of these mutations, we reconstituted each mutant with SERCA in lipid membranes and measured ΔpK_{Ca}, which corresponds to the difference between the pK_{Ca} measured from the normalized calcium affinity curve in the absence and presence of PLN. Typical PLN inhibition of SERCA is characterized by ΔpK_{Ca} (change in calcium affinity) ~0.30 for unphosphorylated PLN (inhibitory complex) and a value of 0 for phosphorylated PLN (pS16-PLN; non-inhibitory complex), indicating no inhibition of the enzyme (34). Optimal enzyme inhibition is obtained with PLN (a proline at residue 21), which gives a ΔpK_{Ca} shift of 0.30. We found that either increased rigidity or increased flexibility of the loop and cytoplasmic regions of PLN decreases SERCA's apparent affinity for calcium (**Figure 4.5**). Increasing PLN rigidity results in smaller ΔpK_{Ca} values, i.e. a LOF mutant. Both P21A and P21I were found to have a ΔpK_{Ca} shift of 0.21, while P21L, the most rigid mutant, displayed the greatest loss in function with a ΔpK_{Ca} shift of 0.17. Increasing PLN mobility also causes decreased inhibitory potency, lowering ΔpK_{Ca} with respect to PLN. For instance, the P21G mutation showed a decrease in ΔpK_{Ca} similar to that of P21A and P21I. S16E, which is dynamically very similar to P21G, also showed a decrease in ΔpK_{Ca} to 0.15, while pS16-PLN (the most dynamic PLN form) shows complete relief of inhibition ($\Delta pK_{Ca} \sim 0$). Therefore, similar to the structure and dynamics (see CSI and NOE values) the inhibitory potencies of S16E-PLN and P21G-PLN are intermediate between those of PLN and pS16-PLN.

4.3.5 Effects of SERCA on the structural transitions of PLN mutants

To map the effects of each mutation on the T to R state transitions of PLN upon interaction with SERCA, we carried out a series of NMR titrations by adding purified SERCA incrementally to each mutant. Addition of SERCA causes the appearance of two different populations (states) of PLN amide resonances in the [^{1}H,^{15}N]-HSQC spectrum (**Figure 4.6A**). In analogy with our previous work (13, 35), the resonances that exchanged between two states were assigned to the free T and R states of PLN. While qualitatively the behaviors of the fingerprint resonances in the [^{1}H,^{15}N]-HSQC of the different mutants upon addition of SERCA were similar, there were marked quantitative differences in the allosteric transition for each mutant. **Figure 4.6B** shows the percentage of the R state for the cytoplasmic residues present with increasing amounts of SERCA (102). For PLN, we found that the transition from the T to R state is gradual, while for pS16-PLN this transition occurs in a cooperative manner, with a combined Hill coefficient of ~3-4 (102). For the more dynamic mutants (S16E and P21G), we observe an increase in cooperativity with respect to PLN, but a substantial reduction in cooperativity with respect to pS16-PLN (see Hill coefficient in Table 1). Interestingly, the more motionally restricted mutants (P21L, P21I, and P21A) show cooperativity similar to that of pS16-PLN, meaning that [SERCA]:[PLN] molar ratios smaller than those required for PLN are sufficient for triggering the T to R transition.

In addition to characterizing the transition to the R state, the reduction in transmembrane domain intensities allowed for the determination of a dissociation constant (K_d) for each mutant (**Figure 4.5B**). This was accomplished using the decrease of the signal intensity of domain II upon titration with SERCA (102). While the more flexible variants of PLN display K_d values ~60 μM (in agreement with our previous NMR and EPR data in DPC micelles (127)), the values of K_d increase with increasing helicity and rigidity up to ~170 μM for P21L-PLN. This supports our earlier hypothesis that PLN molds into the hydrophobic core of the enzyme and its plasticity is an essential requirement for binding (22).

4.3.6 The gatekeeper role of the Q26 side chain

When analyzing the effects of phosphorylation at S16, we proposed that the side chain of Q26 located in domain Ib is crucial for PLN inhibition (102). Using site directed mutagenesis MacLennan and co-workers (130) showed that Q26A mutation generates a LOF mutant, supporting our original hypothesis that alanine is unable to form intermolecular hydrogen bonds. Recent molecular modeling calculations carried out by the same group support the involvement

of Q26 side chain in the SERCA/PLN binding interface (130). **Figure 4.7** shows the intensity retention of the Q26 NH_2 groups at the end point of SERCA titrations with all PLN species. Upon addition of SERCA, the majority of the mutants analyzed retain ~50% of the intensity of the Q26 NH_2 groups, while the intensity retention is much greater (up to 100%) for both phosphorylated species (pS16-P21G-PLN and pS16-PLN). This suggests that changes in the dynamics induced by mutations are not sufficient to affect the gatekeeper role of the Q26 side chain and only phosphorylation causes this side chain to swing away from the protein-protein interface.

4.3.7 Phosphorylation of P21G mutant

We also tested whether P21G still has post-translational control, a crucial factor in the view of developing a new generation of LOF mutants. Indeed, we found that P21G can be fully phosphorylated by PKA (**Figure 4.8**) and like pS16-PLN is a complete LOF species. **Figure 4.8** shows that the calcium affinity curves for pP21G-PLN and pS16-PLN are super-imposable, demonstrating the complete reversal of the residual inhibitory effect of P21G. Interestingly, pS16P21G-PLN is not as dynamic as pS16-PLN. However, the dynamic-function correlation graph shows that it must have passed the mobility threshold to become a complete LOF species.

4.3.8 P21GS16E double mutant

Are the effects of mutations additive? What is the role of electrostatics in PLN phosphorylation? To answer these questions, we cloned a monomeric mutant of PLN with both P21G and S16E mutations. If the effects of the double mutation were additive, we would expect an augmentation of the LOF effects with respect to the single P21G mutation, with a relief of inhibition similar to that of pS16-PLN. On the contrary, we found that this double mutant still has a residual inhibitory potency, which is intermediate between those of P21G and S16E single mutations. While this behavior is counterintuitive at first, this double mutant is slightly more rigid and helical than both P21G and S16E, and has a lower affinity for SERCA (K_d ~ 80 μM), making its inhibitory activity similar to that of P21A. We conclude that (a) the effects of the two mutations are not additive, and (b) PLN dynamics has a dominant effect over electrostatics at S16.

4.4 DISCUSSION

In our previous work, we hypothesized an allosteric control mechanism for SERCA by PLN (127). We showed the existence of a dynamic equilibrium between two states of PLN: T state,

which is more static and *L-shaped*, and R state, which is more dynamic. Based on the effect of phosphorylation at S16, we also suggested that the structural dynamics of PLN may have a direct influence on the calcium affinity and the allosteric transitions of the enzyme (38, 102). In the current work, we demonstrate that (a) the structural dynamics of PLN plays a crucial role in the allosteric regulation of SERCA, and (b) it is possible to gain control of SERCA function through the modulation of PLN structural dynamics. NMR data provides detailed insight into the conformational dynamics of PLN in DPC micelles, while EPR data (**Figure 4.4**) confirms that similar conclusions are valid in lipid bilayers and shows clearly that the principal effect of phosphorylation or mutation in the loop region of PLN is to regulate the equilibrium between R and T states.

In agreement with previous studies (171), we found that proline 21 is pivotal for optimal inhibition of SERCA. Point mutations in this site induce long-range changes in PLN structural dynamics, affecting PLN interactions with SERCA (**Figure 4.3**). Interestingly, the changes in the structural dynamics observed have short- and long-range correlations. In other words, single point mutations not only affect residues in the immediate proximity of the mutated site (loop), but also distant residues with a direct relation to the overall PLN structural dynamics. In particular, CSI correlation plots show a strong positive correlation for N27 and a weaker positive correlation for N30, in antithesis with the trend observed for the other residues around the P21 site. Both residues are proximal to Q26, a key residue that was predicted to swing away from the SERCA/PLN interface upon phosphorylation at S16 (98, 102). It is possible that a less structured domain Ib with concomitant breakage of intermolecular hydrogen bonds is necessary for complete relief of inhibition.

These changes in structure and dynamics of PLN induced by single mutations have direct effects on its inhibitory potency. To interpret the complex energy landscape of SERCA/PLN interactions, we built a simplified energetic diagram that summarizes the behavior of the mutants analyzed (**Figure 4.9**). In the absence of SERCA, PLN is in equilibrium between a more populated T state where the cytoplasmic domain is in direct contact with lipid membranes and a less populated R (activated) state. In the presence of SERCA, this equilibrium is shifted toward the R state. Unphosphorylated PLN binds SERCA to form an inhibitory complex (low energy), while S16 phosphorylation leads to a non-inhibitory complex (high energy) without completely dissociating from the enzyme. Our results indicate that this transition from an inhibitory to a non-inhibitory complex is strongly influenced by structural dynamics.

Mutations change the activation energy for the T to R transition, a primary difference between pS16-PLN and PLN (**Figure 4.9**). In the presence of SERCA, the most rigid mutants (P21A, P21I, and P21L) have a lower activation energy to transition from the T to R state. Interestingly, they show the same cooperativity (similar Hill coefficient) as the most dynamic species (pS16-PLN), suggesting that the R state could be an ensemble of different conformations (105). On the other hand, S16E and P21G display a cooperativity intermediate between that of PLN and pS16-PLN. In the bound state, full inhibition is reached only with PLN that forms a low energy complex with SERCA, while all of the mutants generated are LOF with higher energy complexes.

Can we use this knowledge to design a new generation of LOF mutants? Based on our data, we found that more helical and motionally restricted mutants of PLN are LOF with cooperative T to R state transitions. However, the more rigid mutants have lower binding affinities (K_d ~2 times larger for the most motionally restricted P21L) and would not be good candidates to compete with wild-type PLN for possible rAAV gene therapies (172). On the contrary, more mobile mutants such as S16E and P21G have binding affinities similar to those of the non-mutated PLN and would constitute good LOF candidates. Remarkably, P21G has both an inhibitory effect and affinity for SERCA similar to that of S16E. The residual inhibitory effects are $\square pK_{Ca}$ ~0.22 and 0.15 for P21G and S16E, respectively. Since P21G is more dynamic than S16E, this small but significant difference in the inhibitory potency might be attributable to the difference in charge between the two mutants and the different interaction surfaces with SERCA.

A significant limitation of the S16E mutant is its lack of post-translational control by PKA, i.e., position 16 is no longer phosphorylatable. Unlike S16E, P21G has position 16 still accessible to PKA, enabling post-translational control. This would allow further augmentation of the LOF character of the designed mutants *in vivo*. Of course, the ideal LOF species is pS16-PLN, which still binds SERCA with high affinity without inhibiting its function. Rationally designed LOF mutants should mimic the structural dynamics of pS16-PLN. However, complete LOF mutants would correspond to ablation of PLN (i.e., continuous activation of SERCA), which can result in dilated cardiomyopathy (31). Therefore, it is necessary that the new mutants possess a *residual* inhibitory effect like P21G.

While *in vivo* testing using rAAV is necessary to completely validate the therapeutic possibility of P21G, our *in vitro* assays show that this mutant lays the ground for the next generation of rationally designed PLN species with potential therapeutic application. Unlike

S16E, these new mutants would simultaneously preserve post-translational control in addition to increased internal dynamics.

Indeed, the current study is limited to the correlation between backbone internal dynamics and PLN's inhibition of SERCA. As shown for Q26 (a residue involved in the SERCA/PLN interface), the involvement of this side chain in the protein-protein interface is not affected by mutations at position 21, but rather it is sensitive only to phosphorylation (see **Figure 4.7**). To fully understand how the phosphorylation signal is relayed through the mutation sites in the loop to the transmembrane protein interface, future studies on the structural dynamics of PLN side chains with and without phosphorylation in the presence of SERCA will be necessary.

In summary, we have demonstrated that by fine-tuning the structural dynamics of PLN, it is possible to modulate its allosteric regulation of SERCA. The possibility of controlling SERCA activity will help design new PLN mutants that can be utilized in the correction and reversal of calcium cycling abnormalities in heart failures. From a general structural biology point of view, the possibility of fine-tuning a membrane enzyme's function by modifying its subunits' structural dynamics opens up the application of similar strategies in the regulation of other membrane-bound proteins that are governed by similar mechanisms. For instance, similar approaches can be used in the modulation of the Na/K-ATPase, which is regulated by phospholemman, a single pass membrane protein with a function similar to that of PLN (155).

4.5 FOOT NOTES

This work was supported by the NIH Grants GM64742 and K02HL080081 to GV, and GM27906 to DDT. NJT was supported by an American Heart Association Greater Midwest Affiliate pre-doctoral fellowship (0515491Z). NMR instrumentation at the University of Minnesota High Field NMR Center was funded by the National Science Foundation (BIR-961477) and the University of Minnesota Medical School. We thank Zhiwen Zhang and Florentin Nitu for excellent technical assistance.

	K_d (μM)	n	ΔpK_{Ca}
P21L-PLN	173 ± 24	2.44 ± 0.25	0.17 ± 0.02
P21I-PLN	157 ± 6	2.43 ± 0.27	0.21 ± 0.01
P21A-PLN	132 ± 2	2.69 ± 0.39	0.21 ± 0.01
S16EP21G-PLN	79 ± 7	2.34 ± 0.34	0.18 ± 0.02
PLN	67 ± 4	1.92 ± 0.21	0.30 ± 0.04
S16E-PLN	70 ± 6	2.21 ± 0.27	0.15 ± 0.02
P21G-PLN	70 ± 4	2.18 ± 0.28	0.22 ± 0.05
pS16P21G-PLN	71 ± 4	2.40 ± 0.34	0.00± 0.02
pS16-PLN	62± 4	3.54 ± 0.77	0.00± 0.02

Table 4.1 Summary of the dissociation constants (K_d), Hill coefficients (n), and calcium affinity shifts of SERCA for the different mutants and phosphorylated PLN species**.** The K_d values were obtained from NMR titrations by fitting $I_{retention}$ of the transmembrane domain resonances as a function of SERCA additions. The Hill coefficients were calculated by fitting the appearance of the R state in the [^{1}H, ^{15}N]-HSQC spectra upon addition of SERCA using the Hill equation. The ΔpK_{Ca} values from the coupled assays were calculated as the difference between the pK_{Ca} for SERCA in the presence of each mutant and that of SERCA in the absence of inhibitor (see Experimental Procedures).

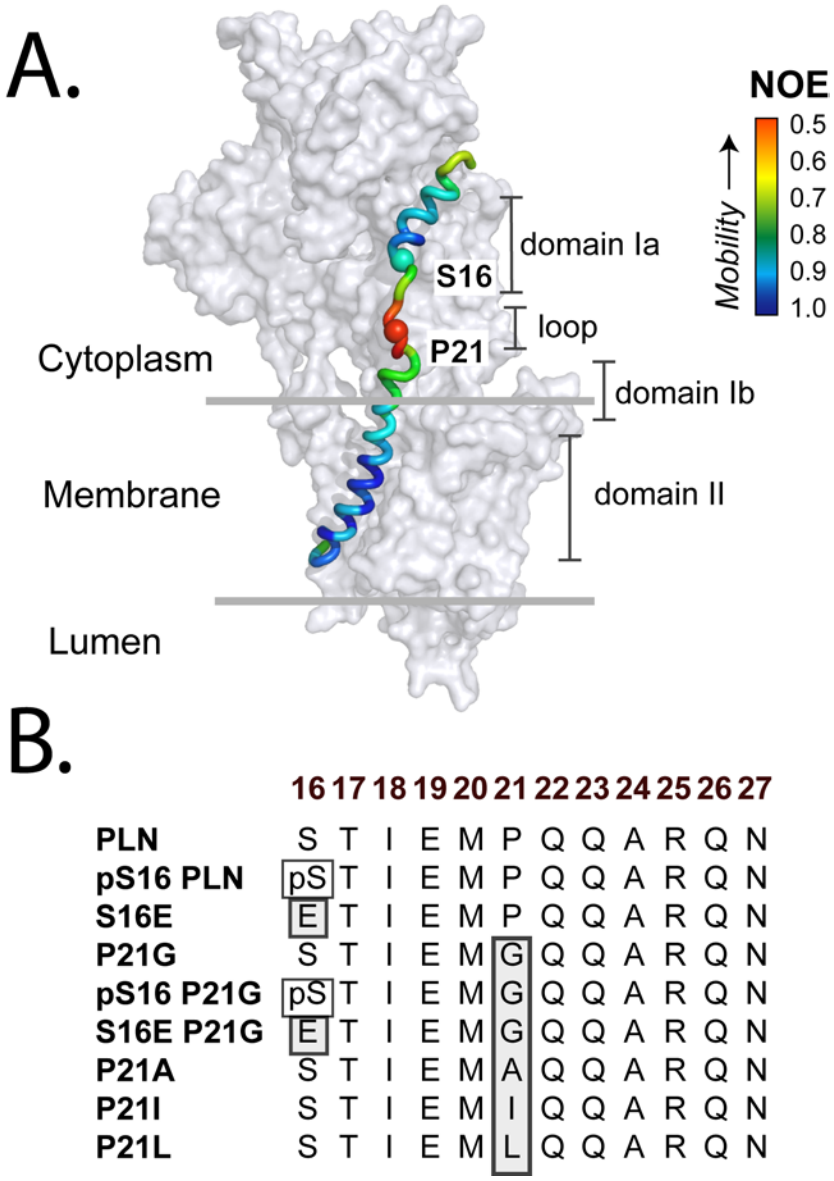

Figure 4.1 Map of PLN dynamics onto the SERCA/PLN complex as modeled by MacLennan and co-workers (98). The color gradation of the backbone of PLN reflects the [^{1}H-^{15}N] heteronuclear NOE values measured by solution NMR (22). The amino acid sequences correspond to the regions 16-27 of all the mutants analyzed in this study.

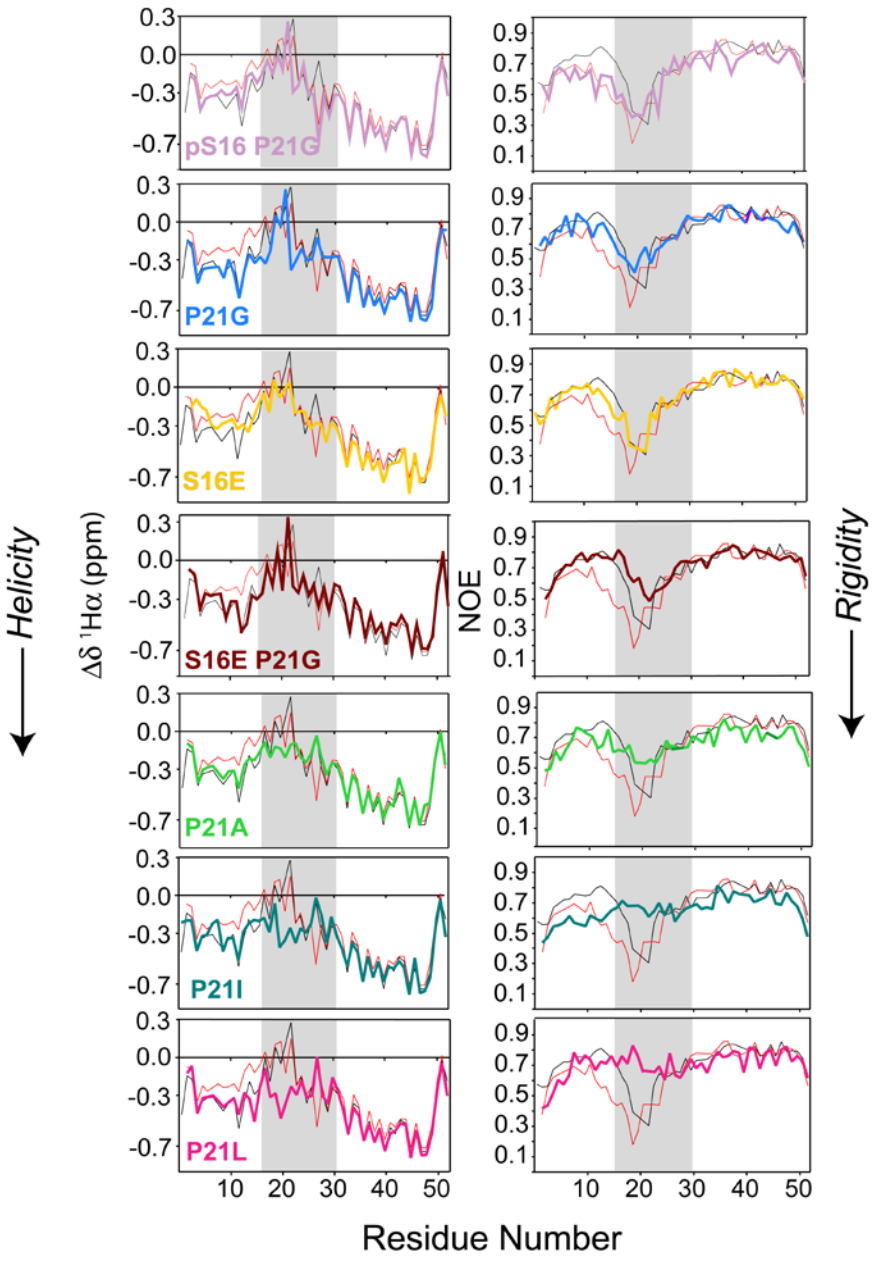

Figure 4.2 Secondary structures and dynamics of all the PLN mutants in DPC micelles. Chemical Shift Indices (CSI) and [^{1}H-^{15}N] heteronuclear NOE experiments are shown for all the mutants analyzed. Black and red traces correspond to PLN and pS16-PLN, respectively, and are used as guidance for the reader. The gray shaded region indicates the residues considered for the structural-dynamics-function correlations (see **Figure 4.3**). The heteronuclear NOE data and CSI for monomeric PLN both phosphorylated and unphosphorylated are reproduced with permission from Zamoon et al (2003) and Metcalfe et al. (2005) (22, 57, 105).

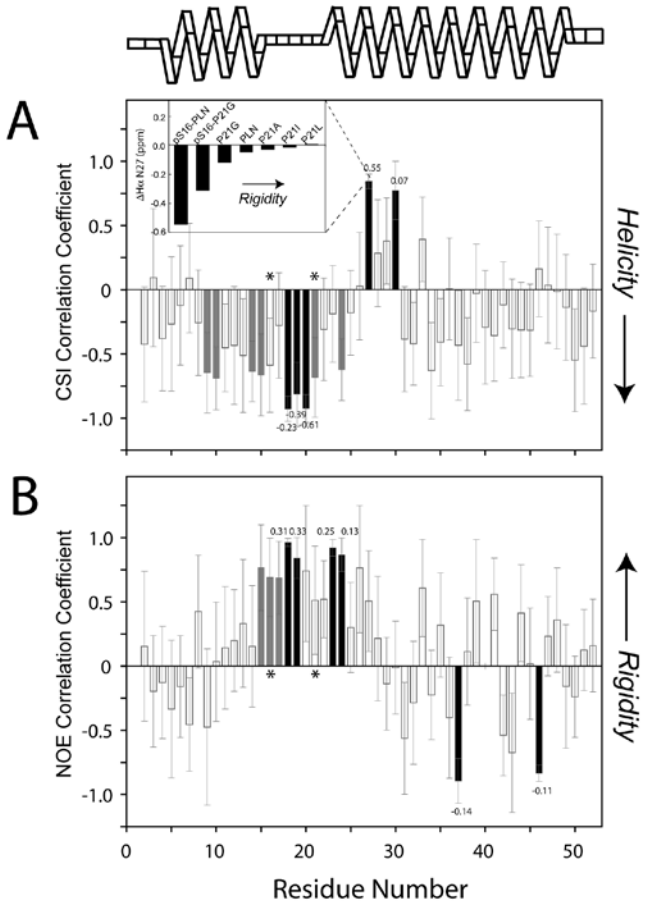

Figure 4.3 Correlation plots for both CSI and heteronuclear NOE. A. CSI correlation plot (CSI correlation coefficients versus residue number). Negative correlations (anticorrelations) indicate that mutations induce a helical conformation. Positive correlations indicate that mutations cause a shift toward the random coil. B. [^{1}H-^{15}N] heteronuclear NOE correlation plot (NOE correlation coefficient versus residue number). Positive correlations indicate that the residues are more restricted, negative correlations indicate that the residues become more mobile. The error bars represent one standard deviation. The inset in panel A shows an example of the chemical shift correlation obtained for N27.

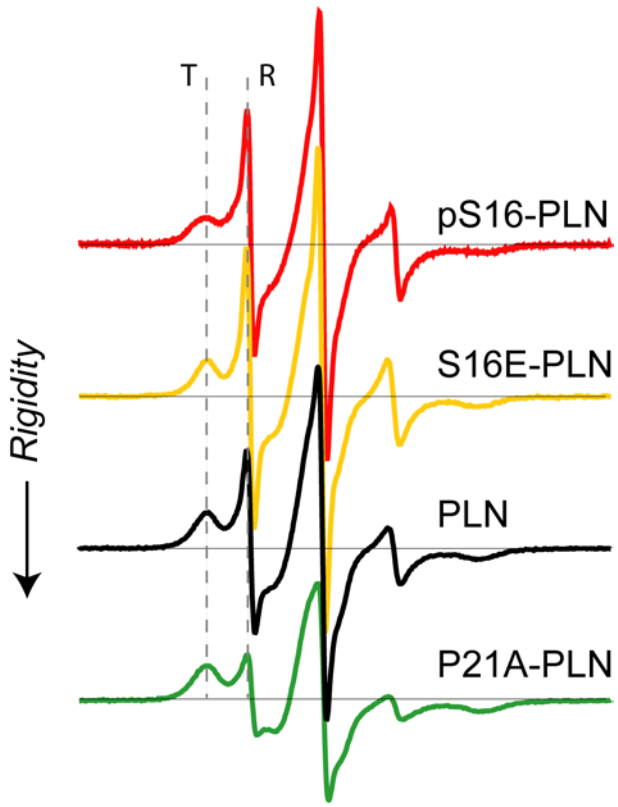

Figure 4.4 EPR spectra of TOAC-labeled PLN in lipid bilayers. Color coding is same as in Figure 4.2: black and red spectra correspond to PLN and pS16-PLN, respectively. Top: Yellow is S16E. Bottom: Green is P21A. Vertical dashed lines indicate the well-resolved spectral positions of low-field lines of the T and R components (conformations). Mole fractions of the R component are 0.31 ± 0.02 (pS16-PLN), 0.23 ± 0.03 (S16E), 0.11 ± 0.02 (PLN), and 0.06 ± 0.02 (P21A). Spectra are normalized to the double integral, so they all correspond to the same spin concentration. The baseline is 120 G wide.

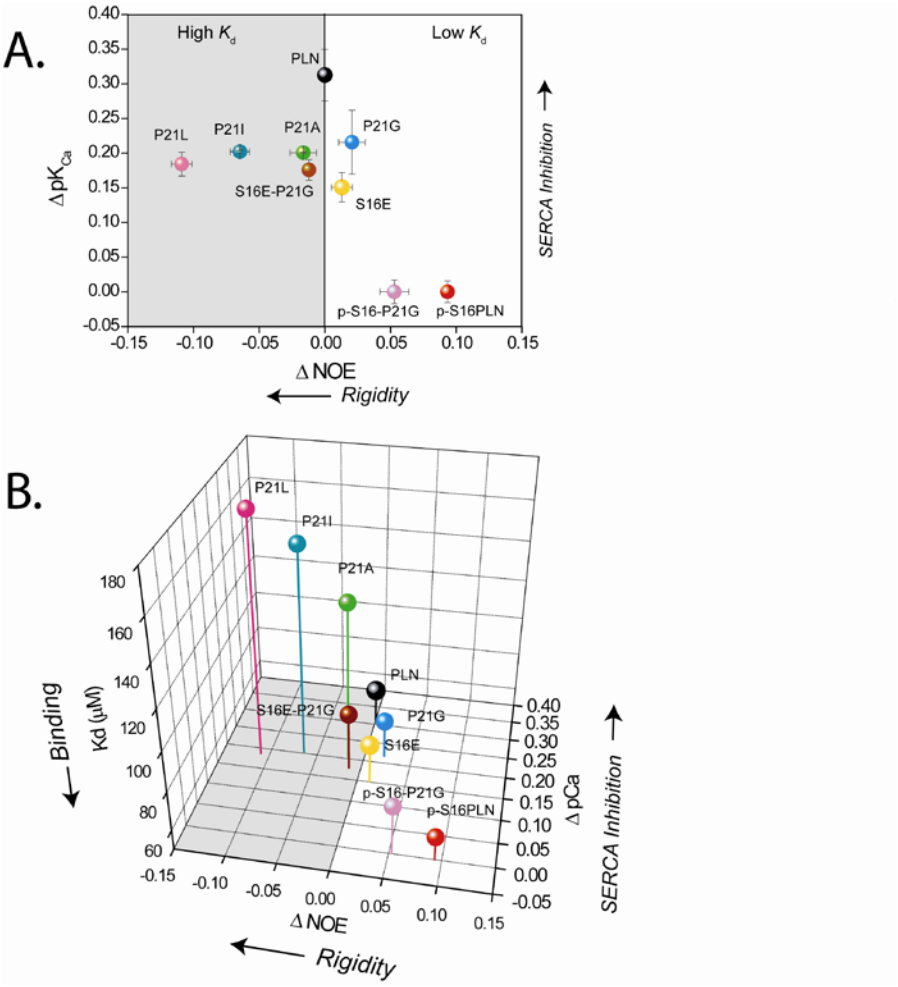

Figure 4.5 Structure-Dynamics-Function correlations diagrams for the different mutants of PLN. A. 2D projection of the change in activity correlated with change in dynamics. B. 3D diagram showing the increasing K_d with backbone rigidity of the different PLN species. The diagrams are divided into two regions: high affinity (with K_d comparable to that of the monomeric PLN) and low affinity (K_d values higher than that of the monomeric PLN). Note that heteronuclear NOE data and CSI for monomeric PLN both phosphorylated and unphosphorylated are taken with permission from Zamoon et al (2003) and Metcalfe et al. (2005) (22, 57, 105).

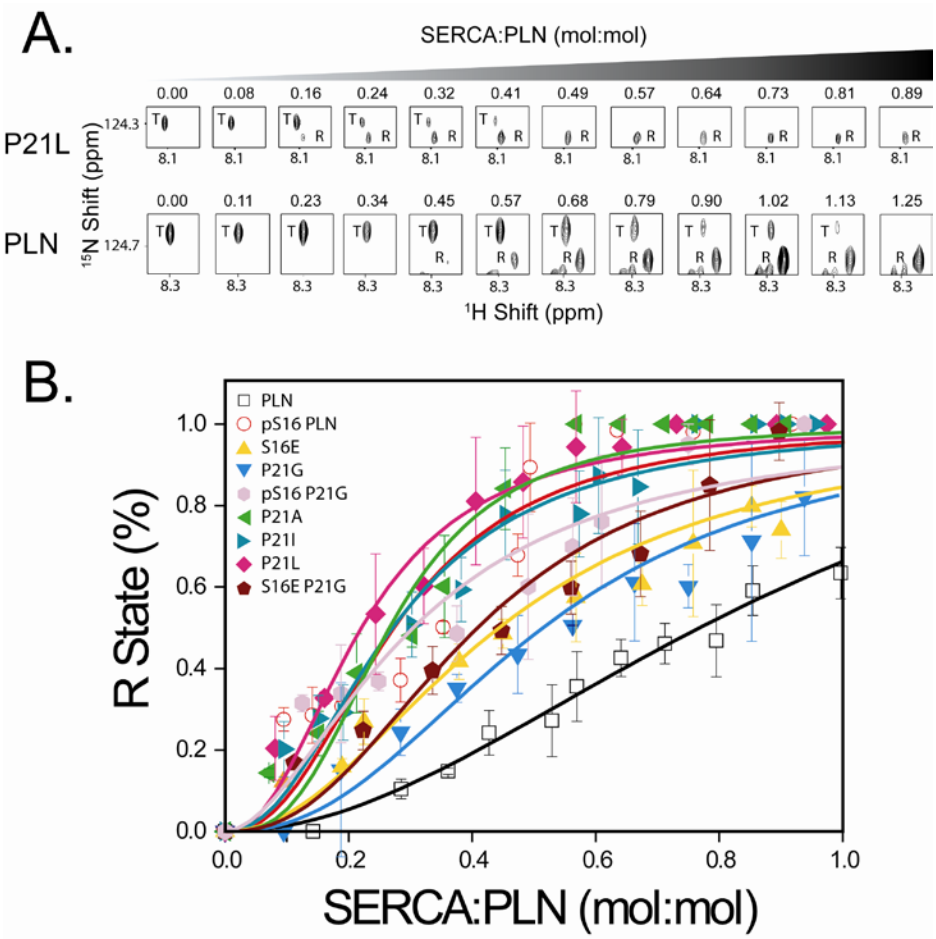

Figure 4.6 T to R transitions for PLN, pPLN and the different mutants. A. Portions of [^{1}H, ^{15}N] HSQC spectra showing the T to R state transition of A11 for P21L-PLN and PLN upon addition of incremental amounts of SERCA. B. Plots of the % of R states derived from the HSQC spectra at different SERCA/PLN ratios. The experimental points were fit using the Hill equation. Note that smaller SERCA:PLN ratios are sufficient to cause the transitions for pS16-PLN and all the motionally restricted mutants. Higher ratios are necessary for PLN, while S16E and P21G show an intermediate behavior.

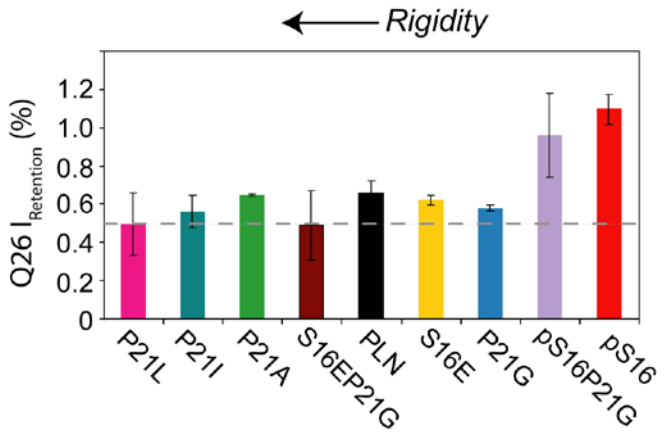

Figure 4.7 Intensity retention for Q26 side chain resonances in the [^{1}H,^{15}N]-HSQC spectra of each mutant upon titration with SERCA. Full intensity retention corresponds to no perturbation upon binding SERCA (i.e. the residue is not involved in the binding interface). Upon phosphorylation almost full intensity is retained, showing that Q26 side chain upon phosphorylation is no longer involved in the binding interface (102).

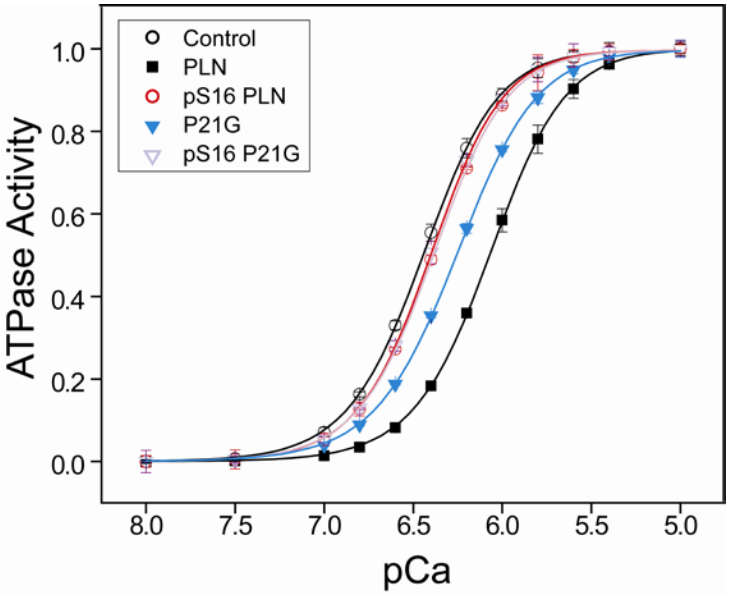

Figure 4.8 Functional assays in lipid bilayers for P21G and phosphorylated P21G. Note that phosphorylated P21G has the same effect as phosphorylated PLN. Data sets were fit by equation 2 and plotted as V/V_{max}. Each point represents the mean ($n \geq 6$); in most cases, the error measured was smaller than the plotted symbol.

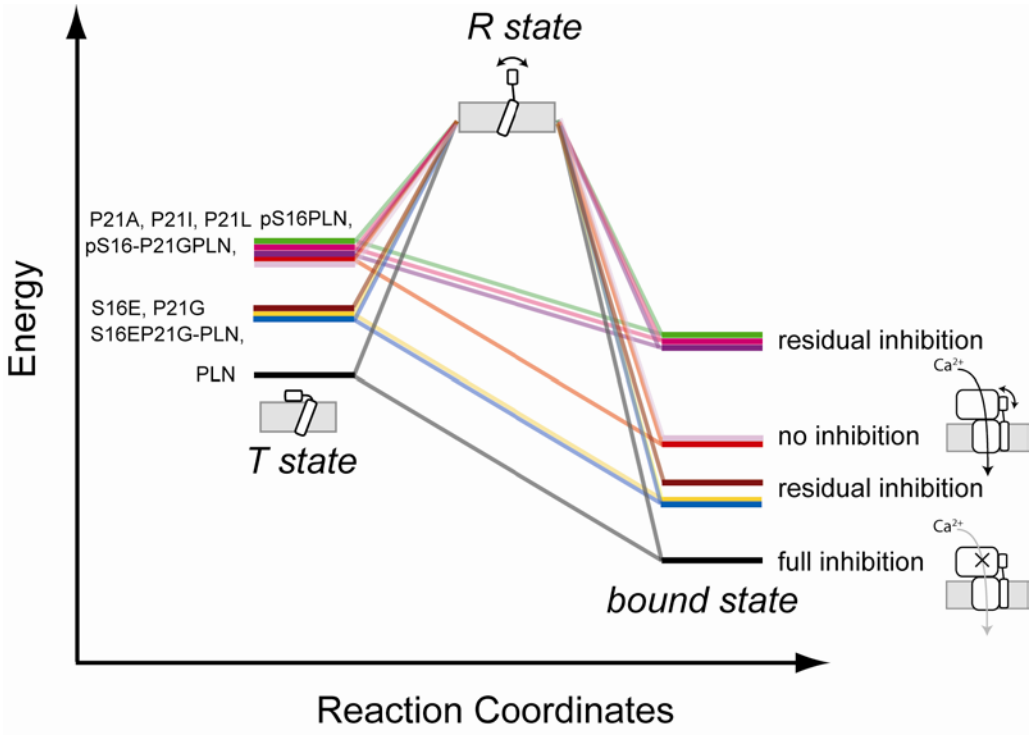

Figure 4.9 Proposed energy diagram to interpret the effect of mutation and phosphorylation on SERCA activity. All the possible states are reported (T, R, inhibitory, and non-inhibitory complexes). The difference in energy levels of the free PLN species reflects the relative propensity of PLN species to undergo cooperative transition from the T to R state upon addition of SERCA (see **Figure 37** and the Hill coefficients in Table 1). The relative energy in the bound state reflects both the K_d values (affinity for SERCA) and the inhibitory potency (i.e. ability to form an inhibitory complex).

Chapter 5

A lethal Arg9Cys phospholamban mutation hinders Ca^{2+}-ATPase regulation and phosphorylation by protein kinase A

Kim N. Ha,[1] Larry R. Masterson,[1,2] Zhanjia Hou,[3] Raffaello Verardi,[2] Naomi Walsh,[1] Gianluigi Veglia,[1,2] Seth L. Robia[3*]*

[1]Department of Biochemistry, Molecular Biology, & Biophysics, [2]Department of Chemistry - University of Minnesota, Minneapolis, MN, 55455

[3]Department of Cell and Molecular Physiology, Loyola University Chicago, Maywood, IL 60153

Reprinted with permission from the Proceedings of the National Academy of Sciences, Vol 108, Issue 7, pp 2735-40

5.1 INTRODUCTION

Heart failure (HF) is the leading cause of morbidity and mortality worldwide (174, 175). The most prominent disorder leading to HF is dilated cardiomyopathy (DCM), a disease characterized by left ventricular dilatation and impaired systolic function (174, 175). DCM has both acquired and genetic etiologies (174, 175). Recent genome sequencing has revealed a high incidence of DCM-associated mutations in cytoskeletal, nuclear, as well as sarcomeric proteins (176). A number of mutations have been indentified in calcium handling proteins, which play a central role in the mechanics of heart muscle contractility (14, 132, 154, 176).

Cardiac muscle contraction (systole) begins when an action potential causes membrane depolarization, activating the sarcolemmal L-type calcium (Ca^{2+}) channels. Ca^{2+} flows through the L-type Ca^{2+}-channels into the cytosol. This increase in Ca^{2+} concentration induces a large-scale release of Ca^{2+} into the cytosol from intracellular stores by the sarcoplasmic reticulum (SR) Ca^{2+}-release channels (or ryanodine receptors). Ca^{2+} then moves toward the contractile apparatus, where it binds the troponin complex and initiates contraction. Muscle relaxation (diastole) occurs when Ca^{2+} is sequestered into the SR by the SR Ca^{2+}-ATPase (SERCA) (177) a membrane-embedded Ca^{2+} pump (178). SERCA is regulated by phospholamban (PLN), which reduces its apparent Ca^{2+} affinity (13, 142). PLN's inhibition is reversed by cAMP-dependent protein kinase A (PKA), which phosphorylates PLN at Ser16, enhancing cardiac contractility and reestablishing Ca^{2+} flux (179).

PLN is a single-pass membrane protein, which comprises three structural domains (5, 57, 180), further subdivided into four dynamic domains [cytoplasm: domain Ia (residues 1–16), loop (residues 17–22), domain Ib (residues 23–30); transmembrane: domain II (residues 31–52)] (22) (**Fig 5.S1**). In membranes, PLN forms homopentamers arranged in a pinwheel topology that are in equilibrium with monomers (40, 107) that bind SERCA with 1:1 stoichiometry (14, 18, 19, 98, 121). Also, it has been proposed that the PLN monomer-pentamer equilibrium plays a central role in SERCA regulation (14).

Several naturally occurring mutations in the PLN gene have been linked to hereditary DCM (132), including a substitution of Arg9 for Cys (PLN^{R9C}) located in the cytoplasmic domain Ia of PLN (Figure 5.S1), which has been identified in several cases of familial DCM (28). R9C cardiotoxic effects are correlated with inefficient Ca^{2+} handling (181) and show a dose-dependent inhibition of SERCA (182). Schmitt et al. hypothesized that PLN^{R9C} leads to DCM by binding irreversibly to the catalytic subunit of PKA (PKA-C) and preventing PLN^{R9C} and/or PLN^{wt}

phosphorylation at Ser16 (28). To date, however, there are no firm conclusions on the molecular mechanisms that link PLN^{R9C} to DCM.

Here, we used an array of biochemical and biophysical techniques both in vitro and in live cells to establish the molecular determinants of the cardiotoxic effects of PLN^{R9C}. Specifically, we focused on the effects of this aberrant mutation on (*i*) the recognition and phosphorylation by PKA-C, (*ii*) the PLN monomer-pentamer equilibrium, and (*iii*) SERCA regulation. We found that the R9C mutation stabilizes the pentameric assembly, hindering PLN deoligomerization, phosphorylation by PKA-C, and SERCA regulation. Importantly, we discovered that these effects are exacerbated under oxidative environments, which are related to both physiological and pathophysiology conditions of cardiac myocytes resulting from myocardial ischemia (183, 184).

5.2 RESULTS

Our immediate objectives were to determine the effects of R9C mutation on (*a*) the PKA-C recognition and phosphorylation, (*b*) the PLN monomer-pentamer equilibrium, and (*c*) SERCA regulation. Toward these goals, we utilized three different PLN constructs with and without the R9C mutation: (*i*) synthetic peptides spanning cytoplasmic residues of PLN (PLN^{wt}_{1-20} or PLN^{R9C}_{1-20}), (*ii*) full-length recombinant pentamers (PLN^{wt} and PLN^{R9C}), and (*iii*) recombinant monomeric PLN (AFA-PLN), where the three transmembrane cysteines (Cys36, Cys41, Cys46) were mutated into Ala, Phe, Ala, respectively. This triple mutation abolishes PLN oligomerization without altering PLN's inhibitory function (185). We carried out these experiments in the presence of dithiothreitol (DTT ranging from 1 to 20 mM) or hydrogen peroxide (H_2O_2 ranging from 1–100 μM), chemicals commonly used to mimic physiological redox conditions and oxidative stress (186, 187).

5.2.1 Effects of the R9C Mutations on the Phosphorylation Kinetics by PKA-C.

Under reducing conditions, phosphorylation kinetics of synthetic PLN peptides were monitored using a coupled enzyme assay (188), standardized with a synthetic peptide corresponding to the minimal recognition sequence for the kinase (Kemptide) (189). Under our experimental conditions, recombinant PKA-C shows a catalytic efficiency typical for Kemptide ($k_{cat}/K_M \sim 0.78$) (188, 190). Interestingly, we found that PKA-C is able to phosphorylate both PLN^{wt}_{1-20} and PLN^{R9C}_{1-20} peptides with similar catalytic efficiencies (**Fig 5.1A** and **Table 5.S1A**). Moreover, we carried out competitive kinetic assays in the presence of products phosphorylated

at Ser16 ($pPLN^{wt}_{1-20}$ or $pPLN^{R9C}_{1-20}$). Our measurements did not show any substantial product inhibition (**Fig 5.1A**). Also, we performed the experiments under oxidative conditions, varying the concentration of H_2O_2 from 1 to 100 μM. Because the coupled enzyme assay is incompatible with oxidizing agents, we monitored peptide phosphorylation using electrophoretic mobility shift assay (EMSA) and identified the products with electrospray ionization mass spectrometry (ESI-MS). We found that the PLN peptides are phosphorylated under both oxidizing and reducing conditions (**Fig 5.1B**), but under oxidizing conditions, PLN^{R9C}_{1-20} forms dimers, which can still be fully phosphorylated by PKA-C. Phosphorylation reactions were repeated with full-length PLN^{R9C} and PLN^{wt}. Interestingly, we did not detect any phosphorylation for pentameric PLN^{R9C} under either reducing or oxidizing conditions (**Fig 5.1B**). The absence of phosphorylation of pentameric PLN^{R9C} was confirmed by EMSA and MALDI-TOF mass spectrometry (**Fig 5.S2**). In contrast, we found complete phosphorylation for the PLN^{wt} and monomeric AFA-PLN^{R9C}. The observed gel shift (**Fig 5.1B**) is typical of AFA-PLN phosphorylation at Ser16 (105). Based on these results, we conclude that phosphorylation by PKA-C is impaired only for the R9C pentamer.

5.2.2 SERCA Activity Assays.

To characterize the efficacy of PLN^{R9C} to bind and reduce SERCA's apparent Ca^{2+} affinity (pK_{Ca}), we performed coupled enzyme activity assays in reconstituted lipids. In agreement with Schmitt et al. (182), we found that monomeric AFA-PLN^{R9C} is a loss-of-function (LOF) mutant, with a partial inhibitory effect on SERCA; i.e., slight reduction in pK_{Ca} (**Fig 5.1C**, *Left*). Phosphorylation at Ser16 relieves the inhibitory effect for both AFA-PLN^{wt} and AFA-PLN^{R9C} (**Fig 5.1C**, *Center*). Remarkably, the PLN^{R9C} pentameric species is a total LOF (**Fig 5.1C**, *Right*). Taken together, these results suggest that if PLN^{R9C} were to deoligomerize, it would be able to reversibly inhibit SERCA.

5.2.3 Stability of PLN Pentamer and Cys Accessibility.

Based on the results above, we deduced that PLN^{R9C} could in principle regulate SERCA, although with a reduced degree of inhibition. However, EMSA and mass spectrometry data show that the pentameric species is not phosphorylated at Ser 16. Therefore, the cardiotoxic species is possibly the pentameric assembly, which prevents phosphorylation and hampers the monomer-pentamer equilibrium necessary for the regulation of SERCA. To further test this hypothesis, we measured the stability of the pentamers (PLN^{wt} and PLN^{R9C}) using thermal unfolding and gel electrophoresis. At 25 °C and in the presence of 10 mM DTT, the pentamer to monomer ratio

detected by SDS-PAGE for PLN^{wt} is approximately 4:1 (78% pentamer). Fitting of the densitometry data from the SDS gels gave a melting temperature (T_m) of 45 ± 1 °C for the wild-type pentamer. Under the same conditions, the pentamer/monomer ratio for PLN^{R9C} increases noticeably (92% pentamer) and its T_m is 51 ± 1 °C (**Fig 5.2**). The thermostability of the mutant is even more pronounced under oxidative conditions (100 μM H_2O_2). We obtained T_m values of 52 ± 2 °C and 67 ± 6 °C for PLN^{wt} and PLN^{R9C}, respectively. The SDS gels of the oxidized pentamers (**Fig 5.2**) show some important features: (*i*) PLN^{R9C} pentamers have slightly less mobility than the PLN^{wt}, which suggests a change in the protein structural topology (i.e., hydrodynamic radius), and (*ii*) the presence of heat-resistant dimers. The latter was also observed in the oxidation studies of PLN^{wt} carried out by Froehlich et al. (191) (**Fig 5.2**). To test whether the formation of the dimers is due to the cytoplasmic (Cys 9) or transmembrane (Cys36, Cys41, Cys46) cysteines, we carried out the same experiments with AFA-PLN^{R9C}. Under reducing conditions, AFA-PLN^{R9C} runs as a monomer on an SDS-PAGE gel; whereas under oxidizing conditions it forms dimers (**Fig 5.3A**). PLN^{R9C}_{1-20} behaves in a similar manner, suggesting a marked tendency of Cys9 to form intermolecular disulfide bridges. To further support the formation of disulfide bridges, we probed the presence of free thiols for the PLN variants with Ellman's reagent (5,5′-dithiobis-(2-nitrobenzoic) acid; DTNB). For PLN^{R9C}_{1-20}, we detected the formation of disulfide bridges even in the presence of moderate amounts of reducing agent (DTT < 1 mM). Under stronger reducing conditions (DTT > 10 mM), however, the PLN^{R9C}_{1-20} runs as a monomer (**Fig 5.3A**) and forms a 1:1 adduct (DTNB: PLN^{R9C}_{1-20}) after ~80 min (**Fig 5.3B**). Under oxidizing conditions (ranging from 1 to 100 μM H_2O_2), PLN^{R9C}_{1-20} forms dimers, with the Cys residues becoming completely inaccessible to DTNB. We repeated these measurements with PLN^{R9C} and PLN^{wt} and found that under reducing conditions PLN^{R9C} is much more reactive with DTNB than PLN^{wt}. We monitored the DTNB reaction up to ~90 min. To reach completion, however, the reaction requires more than 18 h (126). Because the membrane-embedded Cys residues of PLN^{wt} react with DTNB very slowly (> 300 min), we assigned the fast rise of the binding curve for PLN^{R9C} to the reactivity of Cys 9 (**Fig 5.3B**), which is more exposed to the soluble DTNB. Under oxidizing conditions, both PLN^{R9C} and PLN^{wt} behave identically, with very sluggish reaction kinetics with DTNB. The latter is in quantitative agreement with previous cysteine accessibility measurements carried out by Karim et al. (126). Overall, these data suggest that oxidation of Cys 9 results in formation of stable dimers and confers greater thermostability to PLN^{R9C} oligomers.

5.2.4 Probing PLN Oligomerization and SERCA Binding Using Quantitative Fluorescence Resonance Energy Transfer (FRET).

We probed the oligomerization of the PLN^{wt} and PLN^{R9C} pentamers in live AAV-293 cells using quantitative FRET measurements between fluorescent protein tags fused to PLN's cytoplasmic domains (192, 193). Specifically, to detect intrapentameric FRET (i.e., FRET between protomers in each pentamer), we engineered PLN^{wt} or PLN^{R9C} with cerulean fluorescent protein (Cer) and yellow fluorescent protein (YFP), respectively, and coexpressed them in AAV-293 cells (192, 193). For SERCA binding assays, we tagged SERCA with cyan fluorescent protein (CFP) and measured FRET with YFP-PLN constructs. To quantify the dependence of FRET on PLN expression levels, we carried out a cell-by-cell survey of quantitative FRET and fluorescence intensity (an index of protein concentration). For both PLN constructs, we found that intrapentameric FRET increased with protein concentration to a maximum value ($FRET_{max}$) (**Fig 5.4A**). For PLN^{R9C}, $FRET_{max}$ is slightly higher than PLN^{wt} ($p < 0.05$). This corresponds to a modest decrease in the average distances between the Cer-YFP probes within the PLN^{R9C} pentamer relative to PLN^{wt}, which may reflect the formation of disulfide bridges in the pentameric mutant (**Table 5.S2**). The curve representing the concentration dependence for PLN^{R9C} is left-shifted with respect to that of PLN^{wt} (**Fig 5.4A**). The calculated dissociation constant (K_{d1}) was approximately 53% lower than that of PLN^{wt}, suggesting the formation of more stable pentamers for the R9C mutant (**Table 5.S2**). Interestingly, the left-shift of the intrapentamer FRET curve for PLN^{R9C} corresponds to a right-shift of SERCA/PLN^{R9C} binding curve (**Fig 5.4B**), with the calculated apparent dissociation constant (K_{d2}) approximately 130% greater than that of PLN^{wt}. We conclude that the PLN^{R9C} has much lower affinity for SERCA than PLN^{wt} and SERCA is not able to deoligomerize PLN^{R9C} as efficiently as PLN^{wt} (18, 19). This explains the LOF character of PLN^{R9C} measured by ATPase activity (28). Notably, we did not observe a significant difference in $FRET_{max}$ for SERCA complexes with either PLN^{wt} or PLN^{R9C}, which suggests that both species probably bind SERCA in a similar manner.

Because patients with DCM carry both the wild-type and the mutant alleles, with the latter showing a dominant inheritance pattern (28, 182), we also tested the stability of mixed PLN^{wt}/PLN^{R9C} pentamers. We coexpressed Cer-PLN^{R9C} and YFP-PLN^{wt} and measured FRET between them. **Fig 5.4C** shows that $FRET_{max}$ is reduced for the mixed pentamers compared to PLN^{wt} homopentamers. This is consistent with a clustering of Cer-PLN^{R9C} cytoplasmic domains away from YFP-PLN^{wt} oligomers. Notably, mixed pentamers showed a small but reproducible reduction of K_{d1} compared to that PLN^{wt}, suggesting that the interactions between the R9C

mutants within the mixed pentamers prevent deoligomerization. To determine FRET specificity, we carried out competition assays with increasing amounts of a competitor PLN that cannot serve as a FRET acceptor. We found that by increasing the competitor concentration we obtained a reduction in $FRET_{max}$ to a minimum value of 4% (**Fig 5.4D**). This value represents the amount of nonspecific FRET that is subtracted from total FRET for interprobe distance calculations (**Table 5.S2**).

In vitro assays reported in the previous sections and work from other groups (184, 191) demonstrate that both PLN^{R9C} and PLN^{wt} are sensitive to oxidation. Therefore, we treated the AAV-293 cells with 100 μM H_2O_2. Upon addition of H_2O_2, Cer-PLN^{R9C} fluorescence decreased by approximately 4% over the course of 5 min (**Fig 5.4E**), with approximately 5% increase in the emission of YFP-PLN^{R9C}. The FRET ratio YFP/Cer increased by 10% for PLN^{R9C} (**Fig 5.4F** and **Movie 5.S1**), whereas no increase was detected for PLN^{wt} and AFA-PLN (**Fig 5.4F**). To quantify the relative contributions to the observed FRET ratio of protein oligomerization and changes in distance between the fluorescent probes, we measured $FRET_{max}$ at regular intervals and estimated K_{d1} after H_2O_2 treatment. **Fig 5.4G** shows that both $FRET_{max}$ and K_{d1} changed after addition of H_2O_2, with a ~40% reduction in K_{d1} and a ~10% increase in $FRET_{max}$. This suggests an increase in PLN oligomerization with a slightly more compact conformation of the pentameric assembly. Note that we did not detect any large-scale aggregation of PLN^{R9C} either before or after treatment with H_2O_2. Such aggregation would appear as fluorescent puncta, which would be visible by wide-field fluorescence microscopy (**Fig 5.4H**) or total internal reflection fluorescence (**Fig 5.S3**).

5.3 DISCUSSION

Based on coimmunoprecipitation experiments, Schmitt et al. (28) proposed that PLN^{R9C} binds PKA-C irreversibly, creating dead-end complexes that deplete the local reservoir of kinase. The latter would reduce phosphorylation levels of PLN, with concomitant dysregulation of SERCA, leading to DCM. This interpretation accounts for the observed weak adrenergic responsiveness and dominant effect of PLN^{R9C} in heterozygous patients (28). In the present study, we directly tested this hypothesis using both in vitro and in cell experiments. We found that PKA-C was able to phosphorylate both a truncated peptide and monomeric AFA-PLN^{R9C}, which is still able to reversibly inhibit SERCA, although with lower efficacy than PLN^{wt} or AFA-PLN. Most importantly, kinetic assays under reducing conditions show that PKA-C is able to

quantitatively phosphorylate $PLN^{R9C}_{1-20}$with the same catalytic efficiency of PLN^{wt}_{1-20}. Under oxidizing conditions, $PLN^{R9C}_{1-20}$is able to be phosphorylated in a similar manner to PLN^{wt}_{1-20}. Thus, we did not find evidence that this single mutation at the P-7 site of the recognition sequence of PKA-C interferes with the phosphorylation reaction. However, we found that phosphorylation of pentameric PLN^{R9C} is significantly impaired, which is consistent with previous reports (182). Therefore, the stabilization of the pentamer by this Arg to Cys substitution prevents PLN phosphorylation. This finding emphasizes the role of monomer-pentamer equilibrium in the SERCA regulatory mechanism by PLN. The latter is supported by in vivo studies carried out by Kranias and coworkers in mice models, which demonstrate the importance of PLN^{wt} over the monomeric mutant PLN^{C41F} for the optimal relaxation of cardiomyocytes (194).

Disulfide bridges in the cytoplasmic domains of PLN^{R9C} stabilize the pentamer, making it practically inaccessible to PKA-C and unable to deoligomerize and regulate SERCA. An important finding is the presence of dimers in oxidized PLN^{R9C}. The latter has been previously observed by Froehlich et al. upon PLN oxidation by nitroxyl radicals, which promote the formation of disulfide bonds in the transmembrane region, generating noninhibitory oligomers that prevent SERCA regulation (191). Under oxidative conditions, PLN^{R9C} oligomerization is enhanced. This is important given that ischemic oxidative stress conditions are prevailing features of pathological states such as heart failure (195, 196). Additionally, oxidative stresses are also frequent under acute β-adrenergic stimulation and even in nonpathological conditions, where transient oxidative stress could cause cumulative damage (197). Therefore, it is possible that deteriorating redox conditions in PLN^{R9C}-induced heart failure would reinforce anomalous PLN oligomerization and exacerbate the mutation's effects on calcium cycling. Furthermore, we found that for mixed PLN^{wt}/PLN^{R9C} pentamers enhanced oligomerization is a dominant effect. This is consistent with the observed R9C phenotypes for both heterozygous mice (182) and human patients (28).

Based on the above considerations, we propose a model for PLN-SERCA disruption by the R9C mutation (**Fig 5.5**). The principal effect of R9C is the formation of interprotomer disulfide bonds in the cytoplasmic domains, which is transient under reducing conditions and increases upon oxidation, stabilizing the PLN pentamer and rendering the recognition site for the kinase inaccessible. This also prevents PLN dissociation into monomers and formation of the regulatory complex (PLN:SERCA). These effects (enhanced SERCA activity and diminished phosphorylation) are reminiscent of ablation of PLN observed by Kranias and coworkers (198). The formation of the disulfide bridges in the pentamer hinders PLN phosphorylation by PKA,

and possibly induces conformational or topological changes in PLN. We propose that these combined effects are involved in the development of DCM. An important corollary of this study is the emerging role of the PLN pentamer and the monomer-pentamer equilibrium (199). This lethal mutation revealed that oligomerization and deoligomerization of the PLN pentamer within the membrane is directly involved in the SERCA regulatory process.

5.4 EXPERIMENTAL PROCEDURES

5.4.1 Sample Preparation and Kinetic Assays.

Recombinant PKA-C was expressed, purified, and assayed as previously reported (190, 200). All peptides (PLN^{wt}_{1-20} and PLN^{R9C}_{1-20}) were synthesized on a Liberty 12-channel Automated Microwave Synthesizer from CEM (Matthews, NC) (see Section 5.7.1 Supplementary Text). Phosphorylation reactions were performed at 25 °C and monitored by following coupled enzyme (12 units lactate dehydrogenase and 4 units pyruvate kinase) mediated consumption of NADH at 340 nm using a Spectromax microplate reader (Molecular Devices) (188) as previously reported (190, 200). Reaction solutions contained 50 mM 3-(N-morpholino) propanesulfonic acid (MOPS) (pH 7.0), 64 nM PKA-C, 5 mM ATP, and 10 mM $MgCl_2$, with substrate concentrations ranging between 20–300 μM (190, 200). Inhibitor studies were performed with the addition of phosphorylated PLN^{wt}_{1-20}or PLN^{R9C}_{1-20}(0.5 or 1.0 mM) to the reaction solution. For phosphorylation reactions in the presence of H_2O_2, 300 μM of substrate was incubated for 10 min in the reaction solution before initiating phosphorylation with 64 nM PKA-C. The reactions were stopped after 10 min by the addition of 0.5% TFA, and analyzed by EMSA (25% SDS-PAGE gels) stained by Coomassie Blue and ESI-MS after desalting with a C8 Zip-Tip (Millipore).

5.4.2 Thermostability of the Pentamer.

PLN pentamer thermostability was monitored by SDS-PAGE gels. For the reducing conditions, PLN^{wt} and PLN^{R9C} samples contained 100 mM Tris buffer, pH 6.8, 3% sodium dodecyl sulfate, 8% (v/v) glycerol, using a range of 5 to 10 mM DTT; whereas for oxidizing conditions the samples were incubated with 100 μM H_2O_2 for 20 min at each temperature. Each sample (3 μg total mass) was loaded into 5% Next Gels (Amresco) or a 14% Tris-tricine SDS-PAGE gels. The Coomassie-stained gels were quantitated using ImageJ software (201).

5.4.3 SERCA Activity Assays.

PLN variants were coreconstituted with purified SERCA (140, 167) in lipid bilayer membranes (1,2-dioleoyl-sn-glycero-3-phosphocholine: 1,2-dioleoyl-sn-glycero-3-

phosphoethanolamine, DOPC:DOPE, 4:1) at molar ratios of 10:1 PLN:SERCA and 700:1 lipids:SERCA. The Ca^{2+} dependence of the ATPase activity was measured using a coupled enzyme assay at 37 °C (167) and monitored as for the PKA-C assays. Initial rates of SERCA was measured as a function of calcium concentration (pCa), and data were fit to the Hill equation (167).

5.4.4 Cysteine Accessibility Measurements.

Free thiols were assayed via titrations with 5,5′-dithiobis(2-nitrobenzoic acid) (DTNB) (202). Samples (typically 100 μM) were dissolved in 60 mM Tris buffer (pH 8.0) and 1 mM EDTA and added to a reaction vessel containing 100 mM Tris and 0.3 mM DTNB. The reactions were monitored at a wavelength of 412 nm (202). For oxidized and reduced conditions, we incubated PLN samples for 20 min in 100 μM H_2O_2 and 1 mM DTT, respectively. The excess of reducing agent was eliminated with $NaAsO_2$ (203).

5.4.5 Dynamic FRET.

Transfected cells were washed with phosphate buffered saline (PBS) and imaged by epifluorescence imaging at 1 min time intervals with excitation at 427/10 nm and emission at 472/30 nm (for Cer) or 542/27 nm (for YFP). After 5 min of acquisition, the buffer was replaced with 100 μM H_2O_2 in PBS and acquisition continued for 15 min. Mean F/F_0 of all cells (± SE) at each time point was calculated for each filter configuration. The FRET ratio was calculated as the quotient of (Cer F/F_0)/(YFP F/F_0), with a combined error of $\sqrt{(se_{CFP})^2 + (se_{YFP})^2}$. Images of YFP fluorescence were divided by images of Cer fluorescence (both 427/10 nm excitation) using ImageJ software (201).

5.4.6 Quantitative FRET.

$FRET_{max}$ and dissociation constants for the complexes were determined as described previously (201). The observed FRET was calculated for each cell from the extent of donor fluorescence enhancement after acceptor photobleaching, according to $E = 1 - (F_{prebleach}/F_{postbleach})$. For repetitive, nondestructive measurements, FRET was quantified with a “3-cube” method (E-FRET) (192, 204). FRET efficiency of each cell was compared to that cell’s starting YFP fluorescence (an index of protein concentration). FRET concentration dependence was fit by a hyperbolic curve (192, 204). Regulatory complex probe separation distance was calculated using $R = (R_0)[(1/FRET_{max}) - 1)]^{1/6}$ (205). The distance between fluorescent probes in PLN pentamers was calculated according to a ring-shaped oligomer model as previously described (192, 204),

with a Förster radius (R_0) of 49.2 Å for Cer-YFP energy transfer (206, 207). Non-specific FRET between unbound donors and acceptors was determined by measuring the reduction in FRET from YFP - PLN^{wt} to mCherry - PLN^{wt} in cells coexpressing increasing amounts of competing CFP - PLN^{wt} (**Fig 5.S4**).

5.5 FOOTNOTES

Many thanks to Zhihong Hu, Eileen Kelly, Anthony Clementz for technical assistance, and Howard Young and Nathaniel Traaseth for helpful discussions. This work was supported by National Institutes of Health Grants HL80081 and GM072701 (G.V.), HL09536 (K.H.), T32DE007288 (L.R.M.), and HL092321 and EB006061 (S.L.R.).

5.6 SUPPLEMENTARY METHODS

5.6.1 Peptide synthesis. PLN^{wt}_{1-20} and PLN^{R9C}_{1-20} were synthesized using standard Fmoc synthesis on an 12-channel Automated Microwave Synthesizer from CEM (Matthews, NC), starting with Fmoc-Glu(O*t*Bu)-PEG-PS resin (0.4 g, 0.5 mmol/g). Pioneer synthesizer, starting with Fmoc-Glu(O*t*Bu)-PEG-PS resin (0.4 g, 0.5 mmol/g). Side chain protecting groups were 2,2,5,78-pentamethylchroman-6-sulfonyl (Pmc) for arginine, N^{ω}-triphenylmethyl (Trt) for asparagine and glutamine, *tert*-butyl etster (O*t*Bu) for glutamic acid, and *tert*-butyl ethers (tBu) for serine, threonine, and tyrosine. Deprotection of the resin-bound peptide was done using Reagent K (82.5% TFA, 5% phenol, 5% thioanisole, 2.5% 1,2-ethandiol, and 5% water) for 3 hours at 298 K. The resin mixture was washed three times (2 ml each) using the same solution and filtrate was collected. The peptide was precipitated overnight at 273 K in 80 ml of diethyl ether, then collected by centrifugation and washing the pellet 3 times with 30 ml of diethyl ether. The crude peptide was purified by preparative HPLC using a Waters C18 reversed-phase cartridge with 0.1% TFA and CH_3CN as mobile phase. The purity of pooled fractions was >97% as determined by analytical HPLC with C18 column (Vydac) and the identity was confirmed by ESI-TOF. Stock solutions of all the peptides were prepared in double distilled water and the concentrations were assayed by amino acid analysis.

5.6.2 Quantitative phosphorylation of AFA-PLN^{R9C} and PLN^{R9C}. Phosphorylation of recombinant AFA-PLN^{R9C} and PLN^{R9C} was carried out as previously described (105). The extent of phosphorylation was confirmed by mass spectrometry on a MALDI-TOF Bruker BiFlex

spectrometer (Center of Mass Spectrometry and Proteomics of the University of Minnesota) using α-cyano-4-hydroxycinnamic acid (CCA) as the sample matrix.

5.6.3 Cell culture. Transfection of AAV-293 cells with plasmids encoding cyan fluorescent protein (CFP), Cerulean (Cer), yellow fluorescent protein (YFP), or mCherry fusion constructs was performed as previously described (2, 3). Fusion protein constructs used in the experiments include: Cer-PLN^{wt}, Cer-PLN^{R9C}, YFP-PLN^{wt}, YFP-PLN^{R9C}, CFP-SERCA, mCherry-PLN^{wt}, and CFP-PLN^{wt}. The ratios of plasmids for donor- and acceptor-labeled proteins were 1:1 for dynamic, 1:5 for equilibrium measurements of intra-pentameric, and 1:20 for the CFP-SERCA:YFP-PLN^{wt} complex FRET measurements.

5.6.4 Quantitative FRET. To quantify changes in affinity and structure of PLN complexes we performed a live cell equilibrium binding assay as previously described (REF 2, 3). Briefly, FRET was quantified with the acceptor-photobleaching method for a heterogeneous population of transiently transfected cells. The FRET measured in each cell was compared that cell's YFP fluorescence intensity, which was taken as an index of protein concentration. The cell-by-cell concentration dependence of FRET was fit by a hyperbola to obtain estimates of K_{d1}/K_{d2} and $FRET_{max}$, comparing PLN^{R9C} with PLN^{wt} controls obtained on the same day. Sets of repeated experiments were compared using a paired, two-tailed Student's t-test. A value of $p < 0.05$ was considered statistically significant.

5.6.5 Dynamic FRET. Transfected cells were washed with phosphate buffered saline (PBS) and imaged by epifluorescence imaging at 1 minute time intervals with excitation at 427/10 nm (for Cer) or 504/12 (for YFP) and emission at 472/30 nm (for Cer) or 542/27 nm (for YFP). For each experiment, 6 different fields of cells were observed, using a computer-controlled motorized stage (Prior Scientific, Rockland, MA) to navigate to preset positions. Sample z-position was maintained by automatic focus (Nikon Perfect Focus System). After 5 minutes of acquisition, buffer was replaced with 100 μM H_2O_2 in PBS and acquisition continued for 15 minutes. The average fluorescence of each cell was quantified with Metamorph software (Molecular Devices Corp., Downingtown, PA) and normalized to that cell's starting fluorescence prior to H_2O_2 addition, yielding values of F/F_0. Mean F/F_0 of all cells (± SE) at each time point was calculated for each filter configuration. The FRET ratio was calculated as the quotient of (Cer F/F_0)/(YFP F/F_0), with a combined error of $\sqrt{(se_{CFP})^2 + (se_{YFP})^2}$. For visual presentation of FRET ratio changes, images of YFP fluorescence were divided by images of Cer fluorescence (both 427/10 nm

excitation) in ImageJ. Through-objective total internal reflection fluorescence (TIRF) microscopy was performed with a diode laser (449 nm) by way of a Nikon TIRF illuminator and a 100X 1.49 NA objective as previously described (39). For repetitive, non-destructive measurements, FRET was quantified with a "3-cube" method (E-FRET) (204) according to the relationship

$$E = \frac{I_{DA} - a(I_{AA}) - d(I_{DD})}{I_{DA} - a(I_{AA}) + (G-d)(I_{DD})} \quad (4)$$

where I_{AA} is the intensity of fluorescence emission detected in the donor channel (472/30 nm) with excitation of 427/10 nm; I_{AA} is acceptor channel (542/27 nm) emission with excitation of 504/12 nm; I_{DA} is the "FRET" channel, with 542/27 nm emission and excitation of 427/10 nm; *a* and *d* are cross-talk coefficients determined from acceptor-only or donor-only samples, respectively. We obtained values for *a* of 0.72 and 0.67 for ECFP and mCerulean respectively, and a value for *d* of 0.056 for EYFP. *G* is the ratio of the sensitized emission to the corresponding amount of donor recovery. The measured value of *G* was 2.6 for both mCerulean-EYFP and ECFP-EYFP pairs.

5.6.6 Quantification of Non-specific FRET. Non-specific FRET between unbound donors and acceptors was determined by measuring the reduction in FRET from YFP-PLN^{wt} to mCherry-PLN^{wt} in cells coexpressing various amounts of competing CFP-PLN^{wt} (Supplementary Figure 4). The dependence of YFP-mCherry FRET on the proportion of CFP-PLN^{wt} competitor was fit with an exponential decay to determine the minimum value of residual (non-specific) FRET. The measured value of non-specific FRET was subtracted from total FRET signals when calculating probe separation distances of protein complexes.

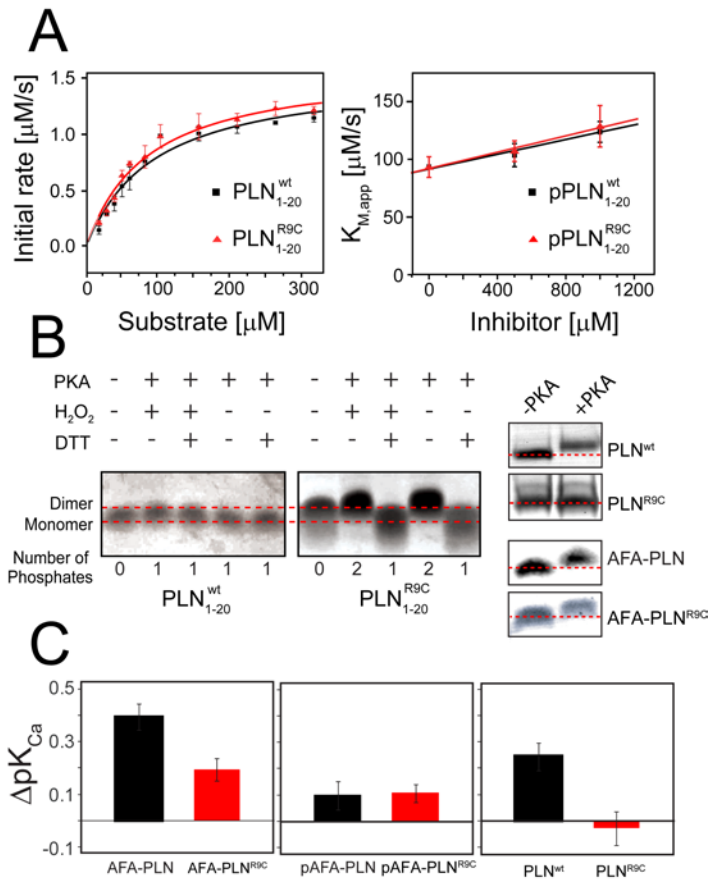

Fig 5.1 PKA-C phosphorylation reaction and SERCA inhibition assays for wild-type and R9C constructs of PLN. (*A*) Steady state phosphorylation kinetics of $\mathbf{PLN^{wt}_{1-20}}$and $\mathbf{PLN^{R9C}_{1-20}}$and competition assays. (*Left*) Plot of the initial rates as a function of substrate concentration. (*Right*) Plot of the apparent K_M as a function of phosphorylated products ($\mathbf{pPLN^{wt}_{1-20}}$ and $\mathbf{pPLN^{R9C}_{1-20}}$). (*B*) SDS-PAGE gels for the phosphorylation reactions of $\mathbf{PLN^{wt}_{1-20}}$, $\mathbf{PLN^{R9C}_{1-20}}$, AFA-PLN, AFA-PLN^{R9C}, PLN^{wt}, and PLN^{R9C} carried out under oxidizing (100 μM H_2O_2) and reducing (10 mM DTT) conditions. The number of phosphates per peptide was detected by ESI mass spectrometry. (*C*) Histograms showing the change in apparent Ca^{2+} affinity (ΔpK_{Ca}) of SERCA in the presence of phosphorylated and unphosphorylated PLN monomers (AFA-PLN and AFA-PLN^{R9C}) and pentameric PLN^{wt} and PLN^{R9C} constructs.

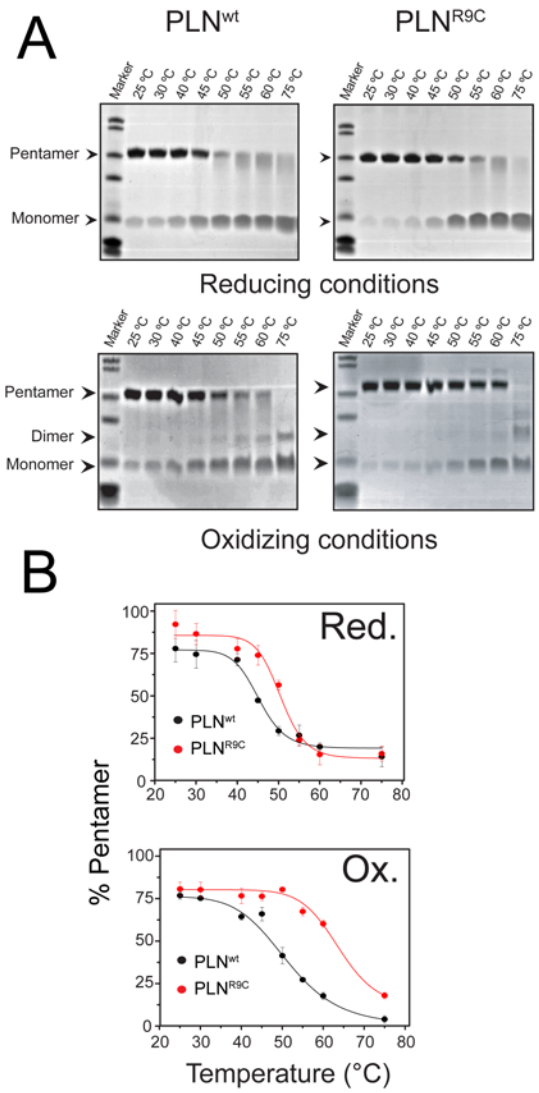

Fig 5.2 Thermostability of PLN^{wt} and PLN^{R9C} pentamers using electromobility shift assay. (*A*) SDS-PAGE gels for PLN^{wt} and PLN^{R9C} incubated at different temperatures under reducing (*Upper*) and oxidizing (*Lower*) conditions. (*B*) Plots of the percent pentamers obtained from densitometry analysis versus temperature for both PLN^{wt} and PLN^{R9C} under reducing (*Upper*) and oxidizing (*Lower*) conditions.

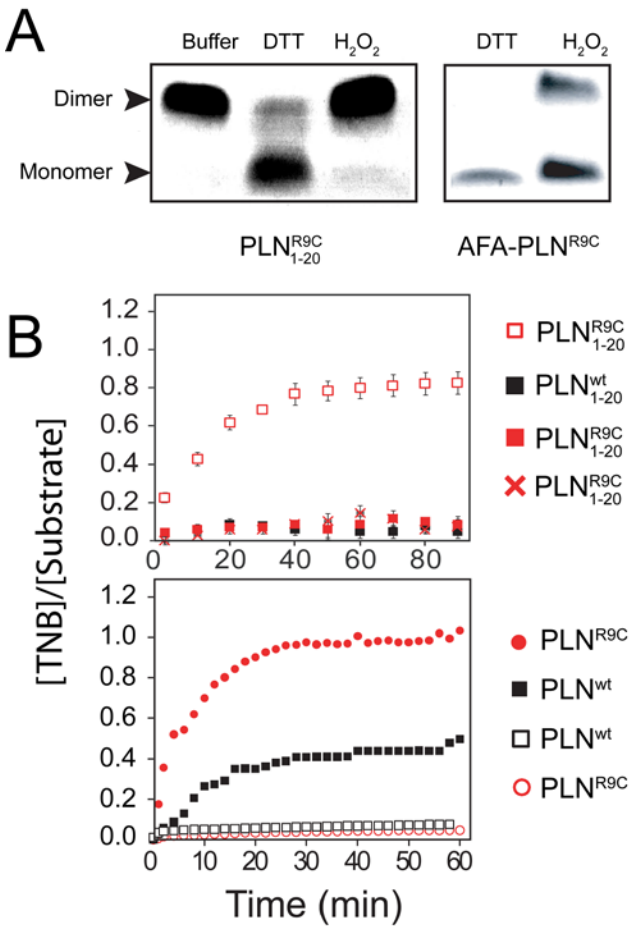

Fig 5.3 Electromobility shift and DTNB cysteine accessibility assays for wild-type and R9C constructs of PLN. (*A*) SDS-PAGE gels in Tris buffer, 1 mM DTT, and 100 μM H_2O_2 of PLN^{R9C}_{1-20} (*Left*), and AFA-PLN^{R9C} (*Right*). (*B*) Plots of cysteine reactivity over time. Cysteine reactivity is measured by moles TNB produced per peptide or full-length protomer from the reaction with DTNB under reducing and oxidizing conditions. (*Upper*) Black squares, PLN^{wt}_{1-20} in Tris buffer; red squares, PLN^{R9C}_{1-20} in Tris buffer; open red squares, PLN^{R9C}_{1-20} in 1 mM DTT; and red crosses, PLN^{R9C}_{1-20} in 100 μM H_2O_2. (*Lower*) Black squares, PLN^{wt} in Tris buffer; red squares, PLN^{R9C} in Tris buffer; open black squares, PLN^{wt} in 100 μM H_2O_2; and open red circles, PLN^{R9C} in 100 μM H_2O_2.

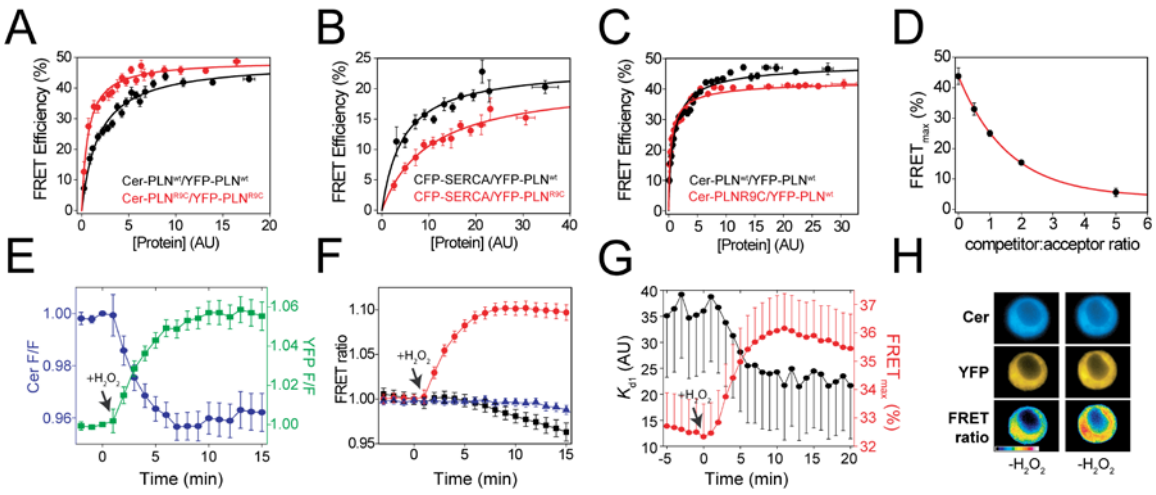

Fig 5.4 In cell FRET measurements of the pentamer stability and SERCA regulation for wild-type and R9C constructs of PLN. (*A*) Intrapentameric FRET versus protein expression level for Cer-PLN^{wt}/YFP-PLN^{wt} and Cer-PLN^{R9C}/YFP-PLN^{R9C} (*B*) Percent of FRET efficiency from CFP-SERCA to YFP-PLN^{wt} and YFP-PLN^{R9C}. (*C*) Percent of intrapentameric FRET efficiency for Cer-PLN^{wt}/YFP-PLN^{wt} homoligomers and Cer-PLN^{R9C}/YFP-PLN^{wt} heteroligomers. (*D*) Plot of $FRET_{max}$ versus competitor to quantify nonspecific FRET. (*E*). Plot of Cer F/F_0 versus time for YFP-PLN^{R9C} and Cer-PLN^{R9C}. Arrows indicate the time of addition of 100 μM H_2O_2. (*F*) YFP/Cer FRET ratio versus time. Arrows indicate the time of addition of 100 μM H_2O_2. (*G*) Plots of K_{d1} (arbitrary units) and $FRET_{max}$ upon addition of 100 μM H_2O_2 (arrow). (*H*) Fluorescence microscopy images of cells expressing Cer-PLN^{R9C} and YFP-PLN^{R9C}. Scale bar = 20 μm. Ratio color scale = 0.4–2.6.

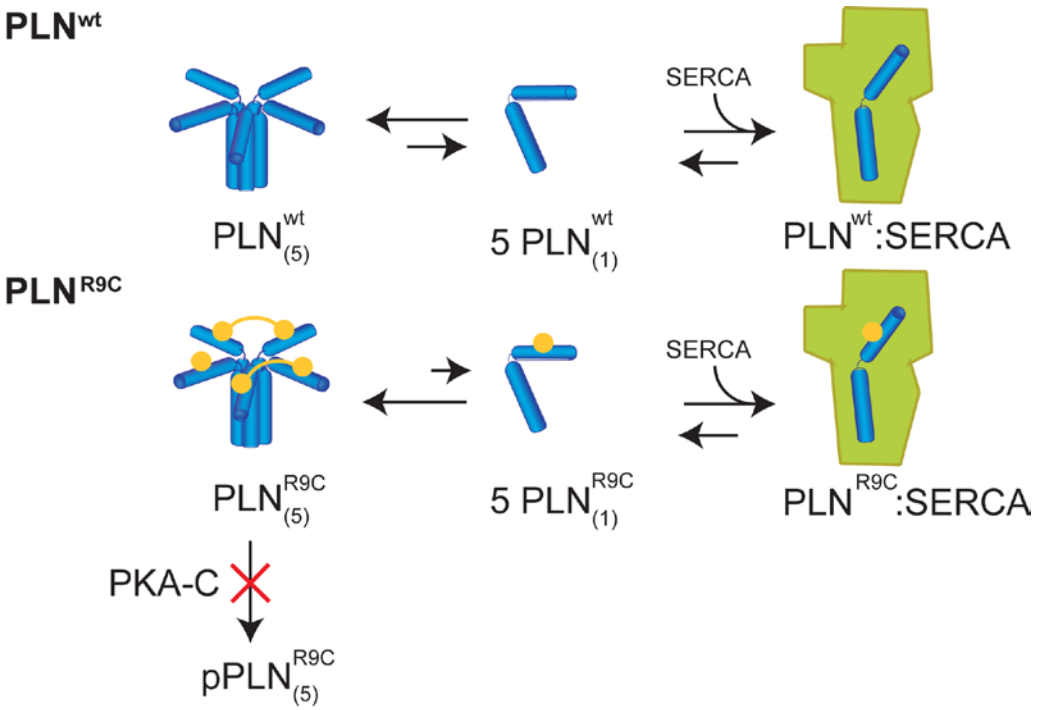

Fig 5.5 Proposed model of the effects of R9C mutation on the SERCA regulatory cycle. The cardiotoxic effects are due to the stability of the PLN^{R9C} pentameric assembly, which prevents deoligomerization, phosphorylation by PKA-C, and regulation of SERCA by the monomeric species. Oxidative stress pushes the equilibrium toward the pentamer, making the PLN^{R9C} pentamer more stable and causing the formation of dimeric species for both PLN^{wt} and PLN^{R9C} (not shown in the model) that are probably unable to regulate SERCA.

Substrate	k_{cat} (s^{-1})	K_M (μM)	k_{cat}/K_M (M^{-1} s^{-1})
$PLN^{wt}_{1–20}$	23.4 ± 1	93.3 ± 9	0.26 x 10^6
$PLN^{R9C}_{1–20}$	23.8 ± 1	82.5 ± 7	0.29 x 10^6
Inhibitor (0.5 mM)			
$pPLN^{wt}_{1–20}$	21.1 ± 1	103.6 ± 10	
$pPLN^{R9C}_{1–20}$	21.7 ± 1	107.1 ± 9	
Inhibitor (1.0 mM)			
$pPLN^{wt}_{1–20}$	19.8 ± 1	123.8 ± 9	
$pPLN^{R9C}_{1–20}$	22.1 ± 1	128.7 ± 18	

Table 5.S1 Kinetic parameters for PKA-C phosphorylation of PLN substrates and product inhibition.

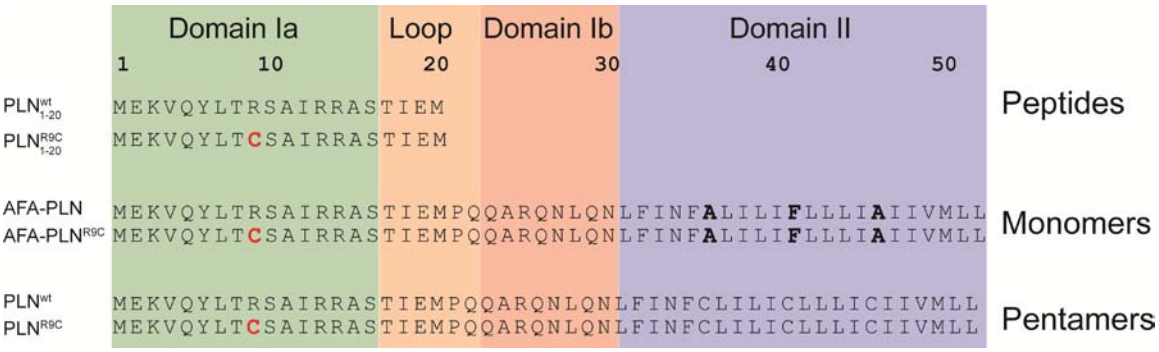

Abbreviations

PLN^{wt}: wild-type pentameric phospholamban

PLN^{R9C}: pentameric phospholamban with the R9C mutation

AFA-PLN: monomeric phospholamban with C36A, C41F, C46A

AFA-PLN^{R9C}: monomeric phospholamban with C36A, C41F, C46A carrying the R9C mutation

PLN^{wt}_{1-20} : PLN^{wt} peptide corresponding to residues 1-20

PLN^{R9C}_{1-20} : PLN^{R9C} peptide corresponding to residues 1-20

PKA-C: catalytic subunit of cAMP-dependent protein kinase A

Fig 5.S1 Primary sequences of all of the PLN constructs and abbreviations used in the text.

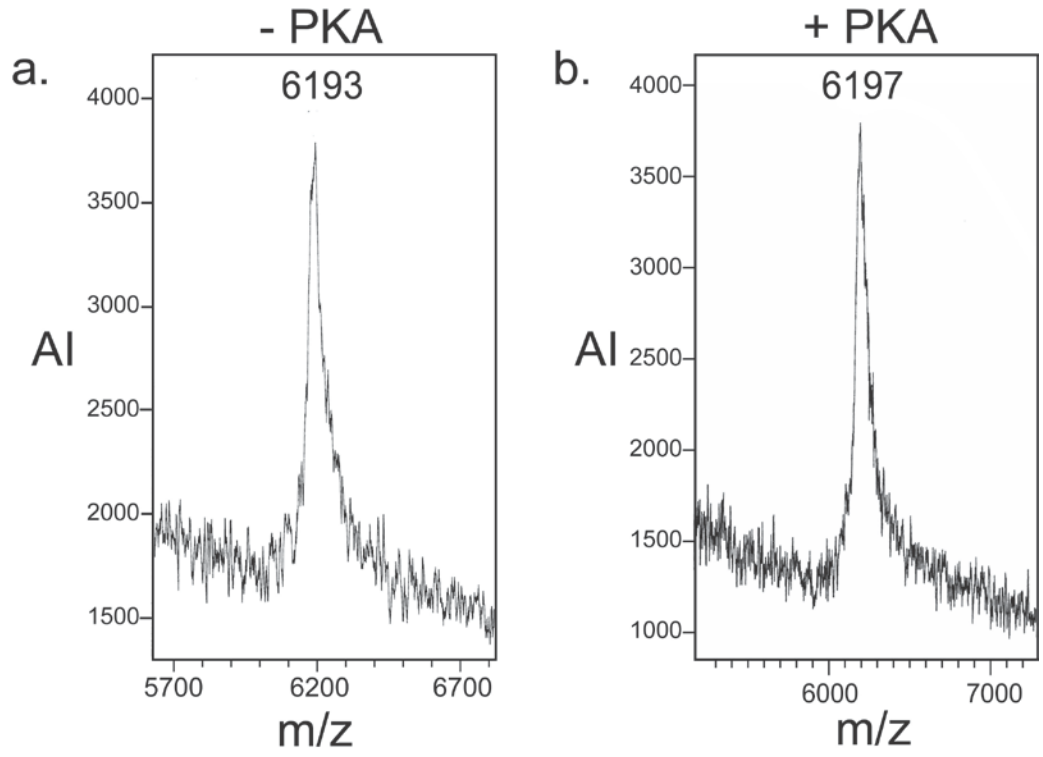

Fig 5.S2 MALDI-TOF spectra of PLN^{R9C} before (left) and after treatment with PKA-C. Note that the peptides are ^{15}N labeled for further NMR studies. The observed masses (6193 Da and 6197 Da) correspond to the expected m/z for PLN^{R9C} (6190 Da) within the error.

	Homo-oligomers		Hetero-oligomers	Regulatory Complex	
	PLN^{wt}	**PLN^{R9C}**	**PLN^{wt}-PLN^{R9C}**	**PLN^{wt}-SERCA**	**PLN^{R9C}-SERCA**
Mean FRET(%)	33.9±1.5	41.2±1.5*	29.9±1.2*	16.2±0.4	10.6±0.5*
$FRET_{max}$ (%)	42.5±1.5	47.1±1.3*	36.3±1.8*	22.8 ±1.2	21.3±2.1#
Acceptor mol fraction	0.93±0.001	0.93±0.001	0.86±0.003	0.97±0.002	0.95±0.003
Probe distance (Å)	61.5±0.6	59.7±0.5*	63.1±0.7*	62.9±0.8	63.9±1.6#
$K_{d1,d2}$ (AU)	0.90±0.11	0.52±0.06*	0.35±0.05*	4.2±0.8	9.7±2.2*
Sample size	2094	784	1341	103	68

* Significant

p<0.05

Not Significant

Table 5.S2 Measured FRET parameters.

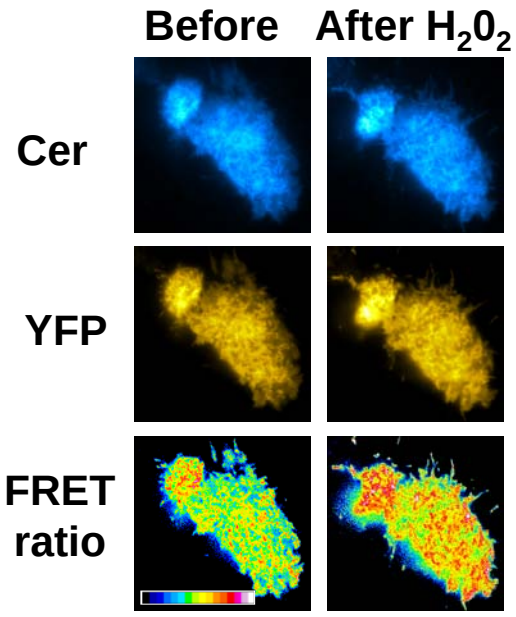

Fig 5.S3 Total internal reflection fluorescence (TIRF) microscopy images of AAV-293 cells expressing Cer- and YFP-PLN^{R9C}. FRET was increased by 100 μM H_2O_2. Scale bar = 20 μm. Ratio color scale = 0.3-0.9

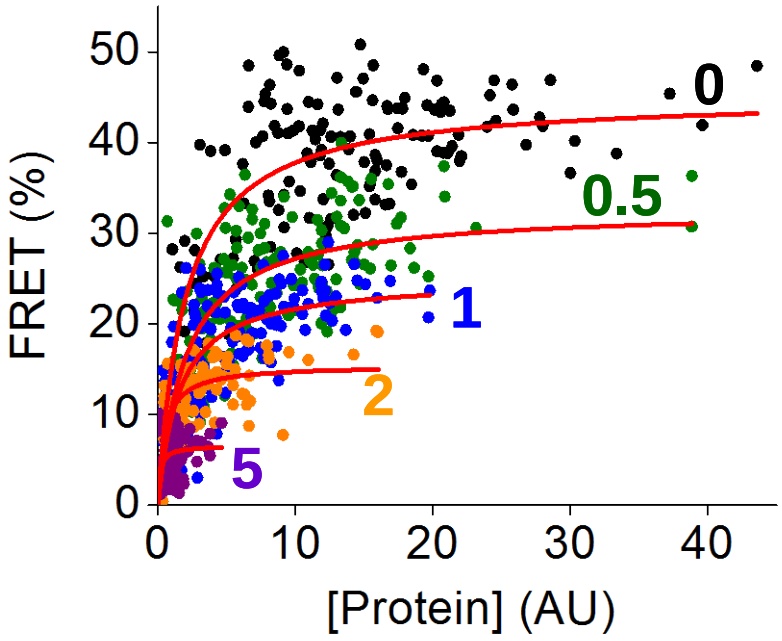

Fig 5.S4 FRET competition assays. YFP-PLN^{wt} to mCherry-PLN FRET decreased with increasing molar ratio of a competitor PLN^{wt} (CFP-PLN^{wt}) which cannot be a FRET acceptor for YFP.

Chapter 6

Tuning the Structural Coupling between the Transmembrane and Cytoplasmic Domains of Phospholamban to Control Sarcoplasmic Reticulum Ca^{2+}-ATPase (SERCA) Function

Kim N. Ha,[1] Martin Gustavsson,[1] and Gianluigi Veglia[1,2]

[1]*Department of Biochemistry, Molecular Biology and Biophysics and* ,[1,2]*Department of Chemistry, University of Minnesota*

Under review, Journal of Muscle Research and Cell Motility, 2012

This article is dedicated to the late Michael and Kate Bárány, in tribute to their outstanding contributions to understanding the biochemistry and biophysics of muscle proteins.

6.1 INTRODUCTION

Ca^{2+} flux is one of the main driving forces of muscle contraction and relaxation, coupling the membrane action potential and the mechanical contraction of muscle (12, 193). The interplay between the sarcoplasmic reticulum ATPase (SERCA) and phospholamban (PLN) is crucial to intracellular Ca^{2+} cycling and proper cardiac muscle contraction and relaxation, and dysfunction in their protein-protein interactions have been implicated in cardiac disease (27). SERCA is a 110 kDa integral membrane P-type ATPase, which utilizes ATP hydrolysis to transport ~70% of Ca^{2+} into the SR (14). SERCA comprises a large cytoplasmic domain that includes the actuator domain, the phosphorylation domain, and a nucleotide binding domain, along with 10 transmembrane helices constituting the Ca^{2+} channel (91). The cardiac isoform of SERCA (SERCA2a) is regulated by PLN, a single-pass membrane protein that binds the enzyme *via* intramembrane interactions, reducing its apparent Ca^{2+} affinity (13, 41, 142). β-Adrenergic stimulation unleashes protein kinase A (PKA) that phosphorylates PLN at Ser16, reversing its inhibition of SERCA and augmenting the diastolic phase (177).

Naturally occurring mutations in PLN have been discovered to be related to familial forms of cardiomyopathy: R9C (28), R9L and R9H (29), R14del (30), and L39stop (31). Though some deleterious mutants have been identified, PLN has also become an obvious target for gene therapy (32, 33, 133). The pathway to innovating genetic treatments to PLN:SERCA interaction dysfunction has recently become a new interest in the field, due to the success of S16E, a pseudo-phosphorylated form of PLN which was introduced to hamsters with a cardiomyopathy phenotype via rAAV gene therapy, and effectively reduced the progression of the cardiac failure (32). The model has also been introduced into large animal models with success (33).

Numerous mutagenesis studies of PLN have been carried out by the MacLennan and Jones groups, offering invaluable insight by identifying residues crucial to PLN's inhibitory ability (34, 125). Although these studies served as a crucial starting point to understanding the effect of point mutations in PLN have on SERCA activity, they often did not identify the reasons for observed functional effects, *i.e.* whether the mutation induced a change to structural dynamics, altered the binding surface, decreased SERCA binding, *etc*. What is clear from the data is that the transmembrane domain is *Janus*-faced, with one side of the helix primarily involved in oligomerization and the other side binding to SERCA. Mutagenesis studies show that domain Ia and the loop are the optimum targets for designing loss-of-function (LOF)

mutants. In contrast, mutations in domain Ib and domain II yield varying results, but all known gain-of-function (GOF) and super-inhibitors are concentrated in those two domains (**Fig 6.1B**).

PLN is a 52-amino acid integral membrane protein which is comprised of three structural domains (5, 6, 57) that are further subdivided into four dynamic domains (cytoplasm: domain Ia (residues 1-16), loop (residues 17-22), domain Ib (residues 23-30); transmembrane: domain II (residues 31-52)) (5, 6, 22) (**Fig 6.1A**). The transmembrane helix of PLN is the principle structural domain which inhibits SERCA (128, 185), while the regulatory phosphorylation Ser 16 site, which determines the inhibitory or non-inhibitory state, lies in the cytoplasmic helix (82). Despite its small size, PLN can populate several conformational states, and domain Ia and Ib participate in folding/unfolding equilibria, which are important for SERCA inhibition as well as recognition by PKA(21, 23, 24). The loop connecting these two domains also has functional relevance, in particular the Pro21 residue that lies in the center of the loop. Squier and co-workers report that mutation of Pro21 to Ala in a monomeric cysteine-null background led to partial inhibition of SERCA, increase in overall helicity, decreased dynamics at the C-terminus, and local structural changes at the loop, most notably diminished solvent accessibility of the loop (171). Additionally, our group has reported that the SERCA inhibition and binding could be tuned based on modulating the dynamics of the loop through mutation in the Pro21 site (25) and that the loop domain could act as a dynamics rheostat. Our studies identified the mutant species AFA-PLN^{P21G} to be a possible candidate for treatment of heart failure by delivery via rAAV gene therapy. AFA-PLN^{P21G} was found to have the same structural dynamics and functional characteristics as PLN^{S16E}, a PLN mutant already proven to be successful in reversing heart failure in animal models by Chien and coworkers (32, 33).

The rationale of this study is to build on our previous success tuning the structural dynamics of PLN to control SERCA function by *systematically* introducing a series of glycine residues to the loop domain. Our original hypothesis was that an increase of dynamics in the loop would interrupt the structural coupling between the transmembrane helix, which is primarily responsible for SERCA inhibition, and the cytoplasmic helix, which contains the phosphorylation sites that dictate the inhibition state. To test this hypothesis, we sought to introduce single Gly mutations at the M20 site and Q22 site to investigate whether the loss-of-function (LOF) rendered by the P21G mutation was site-specific (**Fig 6.2**). Secondly, we determined the SERCA inhibition of the phosphorylated species to see if post-translational control of these single Gly-mutants of PLN still remains intact, a property which has been suggested to be crucial for therapeutic success (25). Thirdly, we expanded the Gly mutations

into double and triple mutations: AFA-PLN$^{M20G\ P21G}$ and AFA-PLN$^{M20G\ P21G\ Q22G}$. Our results suggest that the structural dynamics of the glycine mutants can be tuned, resulting in varying degrees of fast timescale dynamics and degrees of SERCA inhibition. However, species where the mutation increased the dynamics past the threshold set by the phosphorylated species behave as the transmembrane helix alone.

6.2 MATERIALS AND METHODS

6.2.1 Cloning of PLN mutants

Primary sequences of the mutants cloned in this study are described in **Fig 6.2.** Cloning was performed using the Stratagene QuikChange protocol as previously described (25). For the AFA-PLN^{M20G}, AFA-PLN^{P21G}, and AFA-PLN^{Q22G} constructs, the pMal-c2E-TEV-AFA-PLN plasmid was used as a parental template, which expresses a maltose binding protein (MBP) PLN fusion protein with a tobacco etch virus (TEV) protease cleavage site encoded in-between. The forward primer for the AFA-PLN^{M20G} is as follows: 5' – ACC ATT GAA GGC CCG CAG CAG GCG CGC CAG AAC – 3". The forward primer for the AFA-PLN^{Q22G} is as follows: 5' – ACC ATT GAA ATG CCG GGC CAG GCG CGC CAG AAC – 3". The forward primer for the AFA-PLN$^{M20G\ P21G}$ is as follows: 5' – GGC AGC ACC ATT GAA GGC GGC CAG CAG GCG CGC CAG AAC CTG – 3". The cloning of GGG-PLN required two PCR reactions on the P21G PLN AFA background, first converting M20 to G and then Q22 to G. Pentameric mutants were cloned using the pMal-c2E-TEV-wtPLN plasmid as the parental template. PLN^{M20G}, PLN^{P21G}, PLN^{Q22G} were cloned using the same primers as for the AFA-PLN constructs. PLN$^{M20G\ P21G}$ was cloned stepwise, using PLN^{P21G} as the initial template. PLN$^{M20G\ P21G}$ was then used as the template for the PLN$^{M20G\ P21G\ Q22G}$ mutant. Stepwise mutagenesis was necessitated due to the high T_m values of primers containing codons encoding for glycine, because of their high GC content. After mutagenesis was confirmed from EtBr stained agarose gels, the PCR reaction was transformed into DH5α cells and grown on ampicillin-agarose plates. Subsequent colonies were grown overnight in 5 mL Luria-Bertani (LB) media with 0.1% ampicillin, and then spun down on a tabletop centrifuge at 13,000 RPM. The remaining pellet was resuspended and the plasmid was extracted from the pellet using the Qiagen Quick-Spin Miniprep kit. Constructs were confirmed through sequencing at the University of Minnesota Biomedical Genomics Center. Correct target constructs were then transformed into BL21(DE3) *Escherichia coli* cells.

6.2.2 Protein Preparations and ATPase Activity Assays

Protein expression and purification were performed on all constructs as previously described(41, 101). Phosphorylation of PLN samples at Ser16 was performed as previously described (23, 25, 105) using recombinantly expressed protein kinase A purified by an established protocol (200). Phosphorylation was confirmed by a band shift in the SDS-PAGE, and by MALDI-TOF mass spectrometry. The degree of SERCA inhibition by PLN analogs was determined using a coupled enzyme assay correlating the depletion in NADH absorbance to ATPase activity as previously described (25, 145). SERCA inhibition was measured in reconstituted lipid samples according to Reddy et al. (167). PLN variants were co-reconstituted with purified SERCA in lipid bilayer membranes (DOPC:DOPE, 4:1) at molar ratios of 10:1 PLN:SERCA and 700:1 lipids:SERCA. The calcium dependence of the ATPase activity was measured at 37 °C using a coupled enzyme assay, monitoring the consumption of NADH by the decrease in absorbance at 340 nm using a Spectromax microplate reader (Molecular Devices). Initial rate of SERCA (*V)* was measured as a function of calcium concentration (pCa), and data was fit to the Hill equation (167).

6.2.3 NMR Studies

Unless otherwise noted, NMR samples were prepared with a buffer containing 20 mM Na_2HPO_4 (J.T. Baker), 120 mM NaCl (Malinkrodt), 0.1% NaN_3, and 300 mM dodecylphosphocholine (DPC) (Avertec). Lyophilized PLN was weighed and added in increments to 300 μL buffer until the sample reached an approximate concentration of 1 to 1.5 mM protein. After addition of HPLC purified protein, all samples were adjusted to pH 6.0 with dilute NaOH to neutralize residual trifluoroacetic acid remaining in the protein powder. All heteronuclear single quantum coherence (HSQC) spectra were collected on a Varian spectrometer operating at a ^1H Larmor frequency of 600 MHz. Sample quality was assessed by signal-to-noise and resolution in the 2D spectrum with between 32 to 64 increments in the indirect dimension. Heteronuclear steady-state NOE spectra were collected as previously described (22, 25). Briefly, two spectra were collected using the established pulse sequence based on Farrow, *et al.* (79) with a spectral width of 6000 Hz in the direct proton dimension. 128 scans were done with 64 points in the indirect dimension. The saturation spectrum was collected with a 3 s presaturation period on the proton frequency. Peak intensities were analyzed using NMRView5 software (164).

6.3 RESULTS

Single Gly mutations were successfully cloned on a monomeric AFA-PLN background, yielding AFA-PLN^{M20G}, AFA-PLN^{P21G}, and AFA-PLN^{Q22G}. The species were expressed in *E. coli,* and subsequently isolated by affinity and HPLC chromatography. SERCA activity measurements served as the initial screen to assess the effects of the mutations. Functional assays were performed with SERCA reconstituted in lipids alone as the negative control, and also in the presence of AFA-PLN or the super-inhibitor mutant AFA-PLN^{N27A} as a positive control, giving a consistent ΔpK_{Ca} shift of 0.3 and 0.5 pCa units, respectively. **Fig 6.3A** displays a representative normalized ATPase activity curve which yields the pK_{Ca} shifts. **Fig 6.3B** shows the average ΔpK_{Ca} values for the three mutants as compared to the control AFA-PLN (filled bars). Compared to the AFA-PLN species, the AFA-PLN^{M20G}, AFA-PLN^{P21G}, and AFA-PLN^{Q22G} analogs reduced the PLN inhibition by approximately one-third. Therefore, irrespective of their positioning in the dynamic loop, the single site mutations manifested an LOF character. The extent of this effect is variable, with a gradient of SERCA inhibition ranging from ΔpK_{Ca} of 0.23 ± 0.01 for M20G to ΔpK_{Ca} of 0.16 ± 0.02 for Q22G. Remarkably, previous studies showed that Ala mutations of M20 or Q22 do not render LOF characteristics (14, 34).

To test their propensity to be phosphorylated by protein kinase A (PKA-C) and thereby reverse SERCA inhibition, the Gly mutants of PLN were incubated with catalytic amounts of the kinase and analyzed by gel shift assays. We found that all of the single Gly PLN mutants were quantitatively phosphorylated *in vitro* by recombinant protein kinase A. Importantly, SERCA functional assays revealed that phosphorylation at Ser 16 for each single Gly mutant was sufficient to completely reverse inhibition (**Fig 6.3B, open bars**).

To investigate whether the combination of two or more Gly mutations would increase the LOF effect, we cloned a double mutant, AFA-PLN$^{M20G\ P21G}$, and a triple Gly mutant, AFA-PLN$^{M20G\ P21G\ Q22G}$. We found that (1) the AFA-PLN$^{M20G\ P21G}$ species was a complete LOF mutant, and (2) AFA-PLN^{M20GP21GQ22G} completely recovers the inhibitory function (**Fig 6.3B**). Based on these results, we speculate that combining the Gly at position M20 and P21 conferred even stronger LOF behavior, creating an additive effect in the double mutant. In contrast, a triple mutation eliminated the structural coupling between the cytoplasmic and transmembrane helix, resulting in a species that is similar to the transmembrane helix alone (185).

As just indicated, electrophoretic gel shift assays show that incubation of PKA with these mutants does result in a gel shift typically observed for the phosphorylated species, consistent

with quantitative phosphorylation. These results were confirmed by mass spectrometry**.** The cytoplasmic helix contains the phosphorylation site, while the transmembrane helix is the principal domain responsible for inhibition. We sought to test the hypothesis that phosphorylation of the Gly mutants would not reverse the effects of inhibition, due to the possible breaking of the conformational coupling between these domains. Results indicate that phosphorylation does indeed reverse the effects of inhibition for $PLN^{M20G\ P21G}$ and also $PLN^{M20G\ P21G\ Q22G}$. **Fig 6.3B** shows the averaged SERCA activity measurements of several different samples of unphosphorylated (closed bars) and phosphorylated (open bars) of the double and triple glycine AFA- PLN loop mutations. Values of ΔpK_{Ca} are reported in **Table 6.1**.

A critical issue in the design of possible therapeutic mutations for delivery through gene therapy is the effect the species will have *in vitro* versus *in vivo*, particularly when dealing with possible functional effects that are the result of unknown protein-protein interactions and also interactions with the endogenous species. Hence, we studied the function of mutant with the most LOF character, AFA-$PLN^{M20G\ P21G}$ by comparison to the endogenous wild-type background sequence in order to determine whether the functional results may be due to altered oligomeric states. Functional results with SERCA in the presence of the $PLN^{M20G\ P21G}$ mutant show that this is a strong LOF mutant, with a ΔpK_{Ca} of 0.095 ± 0.021 (**Fig 6.3A, right**), confirming that the M20G P21G mutation results in a LOF species regardless of its monomeric or pentameric state. To characterize the structural features of the mutations, AFA-PLN^{M20G}, AFA-$PLN^{M20G\ P21G}$, and AFA-$PLN^{M20G\ P21G\ Q22G}$ were expressed in ^{15}N isotopically labeled media, purified, and reconstituted in DPC micelles. The ^{1}H-^{15}N HSQC spectra of all three mutants were well resolved (**Fig. 6.S1A**) and assigned using ^{15}N edited NOESY-HSQC experiments at short (70 ms) mixing times to identify short-range NOEs. Amide resonance assignments were correlated to the ^{1}H-^{15}N HSQC assignment for AFA-PLN (**Fig 6.S1B**). Most changes are localized near the mutation site. However, some distal changes, especially in domain Ib, are detected, specifically residues Arg25 and Asn27.

The structural dynamics of these mutations were characterized using nuclear spin relaxation measurements (208). R_1, R_2, and NOE values were measured for AFA-PLN^{M20G}, AFA-$PLN^{M20G\ P21G}$, and AFA-$PLN^{M20G\ P21G\ Q22G}$ (**Fig 6.S2**) in DPC micelles. While the structure is largely intact, as evidenced by only minor perturbations in the ^{1}H-^{15}N HSQC spectrum compared to AFA-PLN, we do observe an increase in the fast (ps-ns) conformational dynamics of the backbone for all of the mutants examined. Increased motions are detected in the intervening loop and domains Ia and Ib. While domain Ib and the loop of the Gly mutants have conformational

dynamics similar to that of pSer16 AFA-PLN, the phosphorylated species is significantly more mobile in domain Ia. Thus, introduction of the single or multiple Gly mutants change only the local motion and does not mimic the conformational dynamics found in the phosphorylated species (pSer16-AFA-PLN). A possible explanation is that the negatively charged phosphoserine interacts with the positively charged side chains of Arg13 and 14, forming transient salt bridges that affect the folding and dynamics of the entire cytoplasmic regions including domain Ia. In fact, the presence of the phosphoryl group shifts the conformational equilibrium of domain Ia of PLN from a folded (T state) to an unfolded (R state) (23, 24). The ^{15}N relaxation data do not support a significant T to R state transition upon Gly mutations. The latter was confirmed by ^{1}H-^{13}C HSQC experiments that image the side chains bearing methyl groups. Indeed, we found that the Gly mutations in the loop do not affect the T to R state equilibrium substantially, i.e. we observed only minor chemical shift changes for the domain Ia methyl groups **(Fig 6.S3).** These findings indicate that the LOF character of the Gly mutants is not directly related to the T/R equilibrium of domain Ia, and that the Gly mutations in the intervening loop cause a local increase in backbone flexibility.

6.4 DISCUSSION

We sought to expand on previously published results on tuning the function of SERCA by altering the dynamics of the loop domain in PLN (25). Our previous results showed that AFA-PLN^{P21G} displayed similar structural dynamics to the pseudo-phosphorylated species PLN^{S16E}, which has shown promise in reversing heart failure in animal models upon delivery via rAAV-mediated gene therapy (133). In addition to mimicking the structural dynamics of the pseudo-phosphorylated form, AFA-PLN^{P21G} also has the additional characteristic of being able to be post-translationally-modified by phosphorylation at Ser16 by PKA, a regulatory feature which is crucial for maintaining Ca^{2+} homeostasis (173).

The functional results of AFA-PLN^{M20G}, AFA-PLN^{P21G}, and AFA-PLN^{Q22G} (**Fig 6.3, Table 6.1**) show that introduction of the Gly residue did not need to be specifically positioned at Pro 21 in order to have a LOF effect. Additionally phosphorylation results of the three species suggest that these mutants can still also be post-translationally modified *in vivo*. Remarkably, similar alanine mutations at M20 and Q22 did not show appreciable differences in SERCA inhibition (34, 130), demonstrating the sensitivity of SERCA activity on the PLN sequence. While all of the mutants resulted in LOF characteristics, they inhibited SERCA to different

degrees, resulting in a gradient of function. This is an important factor when designing mutations to alter contractility. While introducing PLN mutants which are completely LOF would increase SERCA activity and activate diastole in the short term, constitutive activation of SERCA is known to promote hypertrophy (209) and a PLN null genotype is found in humans to result in heart failure (29, 31). Hence, development of mutations of PLN for use in gene therapy would necessitate mutants which sampled a wide array of levels in SERCA inhibition.

The results of AFA-PLN$^{M20G\ P21G}$ show that the LOF effects for the M20 and P21 site were additive, resulting in the least inhibitory mutant of this study. Phosphorylation of this species AFA-PLN$^{M20G\ P21G}$ mutant resulted in a ΔpK_{Ca} similar to that of pSer16 AFA-PLN. The NMR results show minimal differences in the structures of the various mutants. In fact, comparison of the protein fingerprints ([^{1}H,^{15}N] HSQC spectra) of the AFA-PLN$^{M20G\ P21G}$ mutant and AFA-PLN show some slight differences, especially in residues near the mutation site in the primary sequence. A few differences are also evident for residues located in the juxtamembrane domain Ib (**Fig 6.1**). A map of the chemical shift changes upon increasing glycines in the loop did not follow the same trajectory that was seen for pseudo-phosphorylated mutants and the Ser16 phosphorylated species (23). Also, the NMR dynamic parameters (R_1, R_2 and heteronuclear NOE values) in domain Ia indicate that AFA PLN$^{M20G\ P21G}$ is significantly less dynamic than pSer16 AFA-PLN in this domain (**Fig 6.S2**). Still, AFA-PLN$^{M20G\ P21G}$ mimics pSer16-PLN functionally, which suggests that mutations in the loop leads to the reversal of SERCA inhibition by a different mechanism that an order-to-disorder transition of domain Ia, a mechanism that has been proposed for phosphorylated and pseudo-phosphorylated mutants of PLN (23). In contrast to domain Ia, the conformational dynamics of the loop and domain Ib of the Gly mutants are similar to that of pSer16 PLN and thus more mobile than AFA-PLN. Taken together with the chemical shift changes in domain Ib, this alteration of domain Ib conformational dynamics may be responsible for the functional effects associated with the Gly mutations.

Based on the data collected on these single, double, and triple Gly mutants, we hypothesize that the functional effects of the Gly mutations are related to a gradual structural uncoupling of the two helical domains of PLN: the inhibitory transmembrane domain and the regulatory cytoplasmic regions. A single Gly mutation increases the local dynamics and induces LOF character. Also, a double mutation augments the LOF character with concomitant increase of local dynamics. However, three sequential mutations cause a complete *loss of the structural coupling between the regulatory cytoplasmic domain and the inhibitory transmembrane domain*,

rendering the mutant similar to the isolated transmembrane domain, which has an inhibitory potency similar to that of PLN (185). To support this hypothesis, we showed that single and double Gly mutants have increasing LOF character, while the inhibitory potency of the triple Gly mutant is virtually identical to that of AFA-PLN.

Interestingly, AFA-PLN^{M20GP21GQ22G} can be still phosphorylated, reversing SERCA inhibition. The substitution of the three Gly residues in the loop does not prevent the signal of phosphorylation to be relayed from PLN to SERCA to reverse its inhibition. This suggests that phosphorylation is a more complex event that involve both structural and electrostatic changes in both binding partners, with a possible allosteric mechanism where interactions of the phosphorylated domain Ia lead to changes within SERCA that are relayed to domain II. The latter will be resolved when atomic resolution structural information on the SERCA/PLN will be available.

Although the original Ala-scanning experiments performed by MacLennan and coworkers (34) show Ala mutations in the loop region to be non-effectual on SERCA function (with the exception of P21A), Gly mutations in the same region reveal that fairly conservative alterations in the loop region can have a significant impact on SERCA function. **Fig 6.4** shows a structural dynamics and function correlation between different species of PLN, and the blue triangle highlights the optimum area to target when designing LOF mutants to improve cardiac contractility by improving SERCA function. The results of this study are promising in revealing the loop region as an area to target for development of therapeutic PLN mutants, since the phosphorylation site remains intact. The results of studying PLN mutations have established that for a mutant to maintain proper function: (a) it must be able to be phosphorylated in order to relieve inhibition, and (b) the dynamic changes throughout domain Ia, the loop, and domain Ib can mimic the order-to-disorder transition induced by phosphorylation, but they should not exceed the dynamics of pSer16 PLN.

	ΔpK_{Ca}	*Error*
AFA-PLN	0.31	0.02
pSer16 -AFA-PLN	0.025	0.012
AFA-PLN^{M20G}	0.23	0.01
pSer16-AFA-PLN^{M20G}	0.031	0.018
AFA-PLN^{P21G}	0.18	0.01
pSer16-AFA-PLN^{P21G}	0.042	0.013
AFA-PLN^{Q22G}	0.16	0.02
pSer16-AFA-PLN^{Q22G}	0.068	0.014
AFA-PLN$^{M20G\ P21G}$	0.047	0.009
pSer16- AFA-PLN$^{M20G\ P21G}$	0.015	0.010
AFA-PLN$^{M20G\ P21G\ Q22G}$	0.33	0.01
pSer16- AFA-PLN$^{M20G\ P21G\ Q22G}$	0.090	0.017

Table 6.1 ΔpK_{Ca} values for all PLN species averaged over 6 measurements. ΔpK_{Ca} values are calculated from as the difference in pK_{Ca} values from the fits of the SERCA activity curves in the absence and presence of PLN inhibitor.

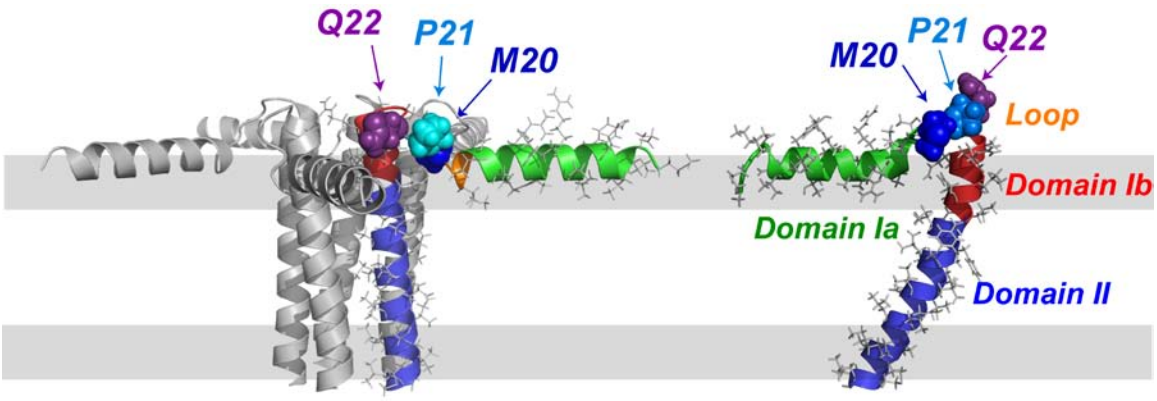

Fig 6.1 Hybrid solution and solid state NMR structures for pentameric wt-PLN (left) and monomeric AFA-PLN (center). The four dynamic domains of PLN are color-coded: domain Ia, green; loop, orange; domain Ib, red; domain II, blue. Sites of loop mutations are rendered in the space-filling motif.

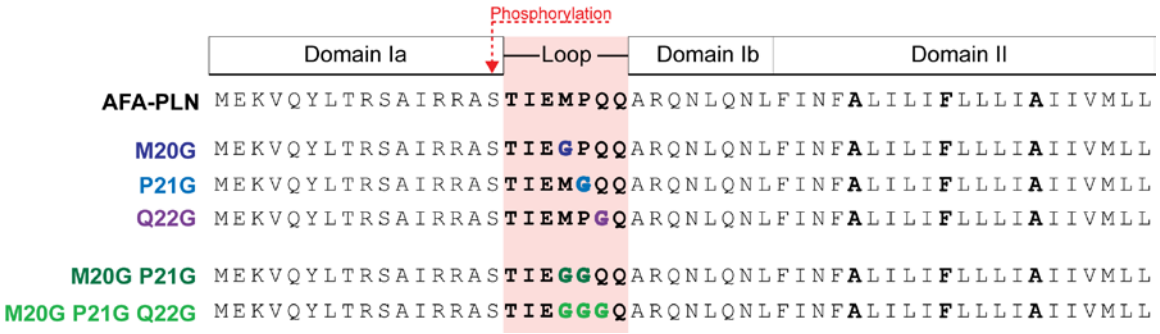

Fig 6.2 Primary sequences of glycine mutants in this study. The secondary structure motifs of PLN (helix, loop, helix) and dynamics domains are displayed above. Mutations are highlighted in the loop region.

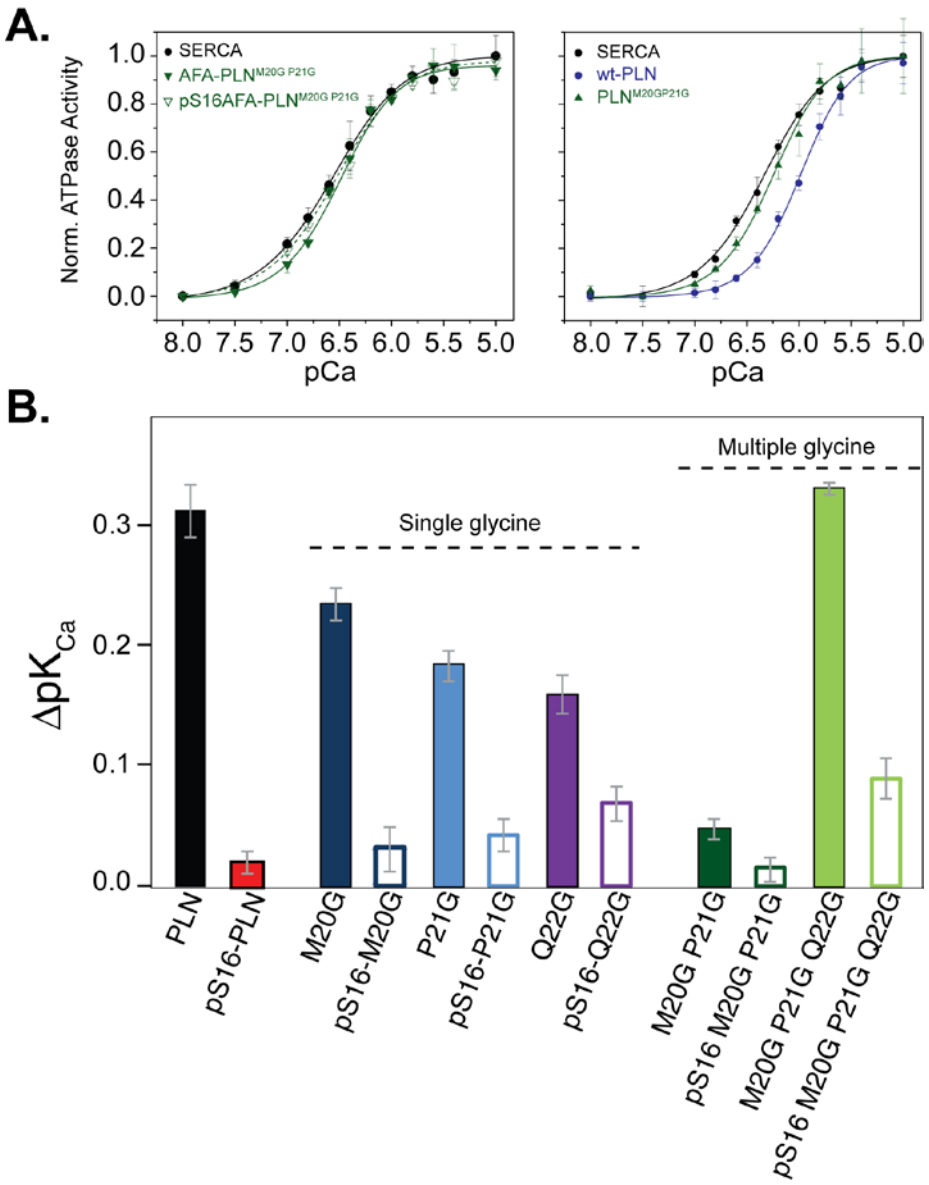

Fig 5.3 Functional measurements of SERCA in reconstituted lipids in the presence of PLN Gly loop mutants. **A**. Coupled enzyme activity assay measurement of SERCA in absence (black circles) and presence of PLN species. Left panel: unphosphorylated (closed green triangles) and phosphorylated (open green triangles) monomeric M20G P21G AFA-PLN. Right panel: wt-PLN (blue circles) and M20G P21G mutant on pentamer background (PLNM20GP21G , green triangles). As in the monomeric conditions, the M20G P21G mutation in pentameric conditions is still severe LOF. **B**. Histogram of ΔpKCa measurements of all PLN species. Error bars are indicative of standard deviation from averaged values of ΔpKCa.

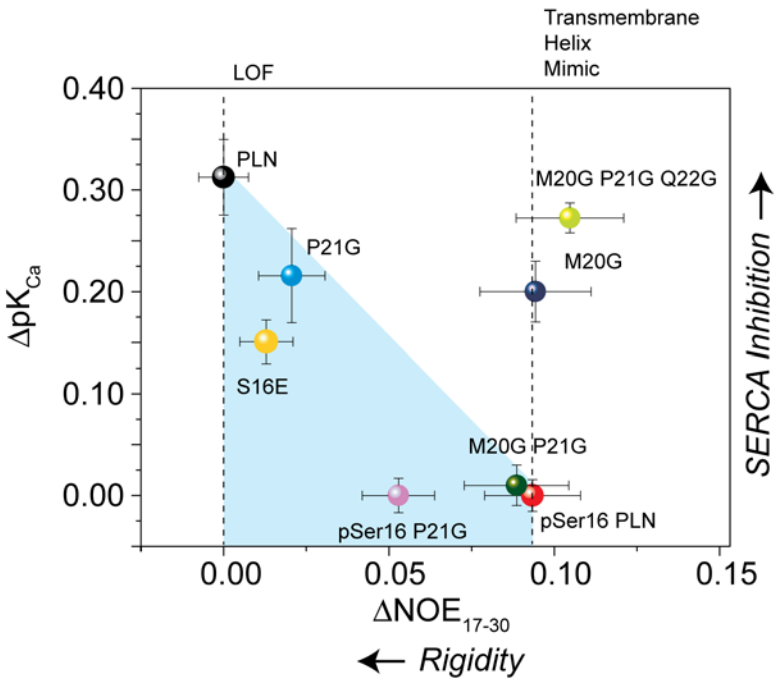

Fig 6.4 Stuctural dynamics-function correlation plot of PLN Gly mutants. Left axis is degree of SERCAinhibition, with a larger ΔpKCa indicating more SERCA inhibition. ΔNOE is difference in average NOE valuesfor each PLN species in the loop and domain Ib (residues 17-30) from AFA-PLN. Higher values in ΔNOE indicates more fast dynamics for that mutant. Red box highlights range of dynamics which results in a completely LOF PLN. Blue triangle highlights optimum region for designing PLN mutants to improve cardiac contractility.

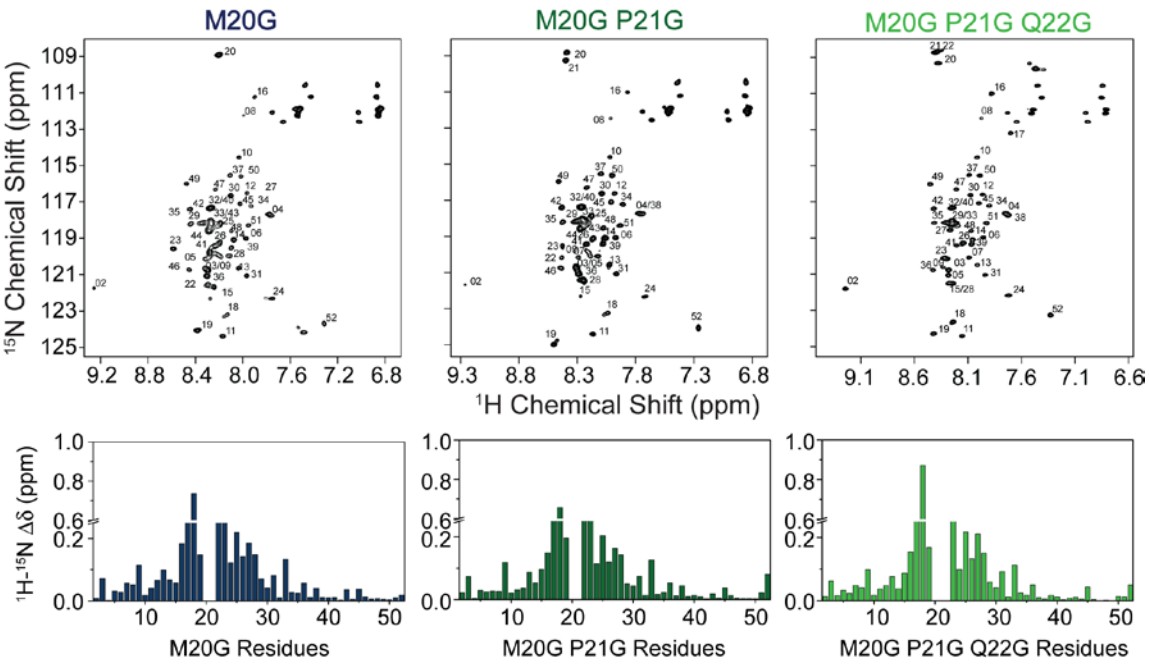

Fig 6.S1 ^{1}H-^{15}N HSQC spectra of AFA-PLN^{M20G} (top left), AFA-PLN$^{M20G\ P21G}$ (top middle), AFAPLN $^{M20G\ P21G\ Q22G}$ (top right) and combined chemical shift perturbations between AFA-PLN and the M20G mutant (bottom left, dark blue), M20G P21G mutant (bottom middle, evergreen), and M20G P21G Q22G mutant (bottom right, lime).

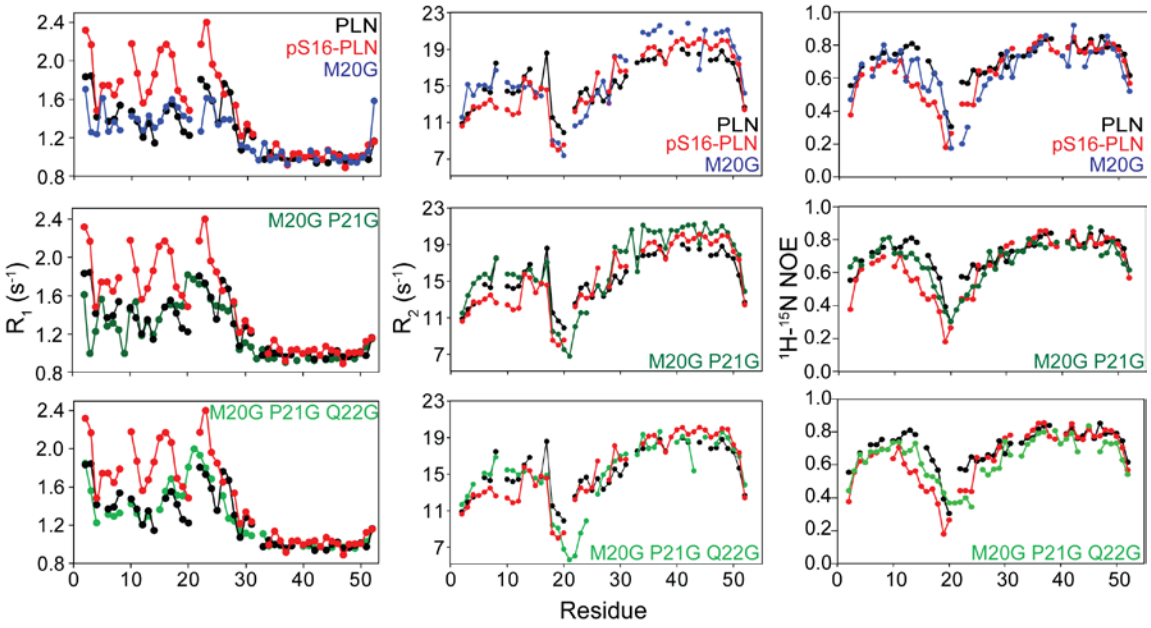

Fig 6.S2 Fast amide backbone dynamics measurements by solution state NMR of Gly PLN mutants. R_1(left), R_2 (middle), and {^{1}H-^{15}N} steady state NOE measurements were done in 300 mM DPC micelles. AFA-PLN (black) and pSer16-AFA-PLN (red) are plotted for comparison. Data for AFA-PLN and pSer16-AFA-PLN are taken from Metcalfe, *et. al.* 2003 and 2005. (22, 105).

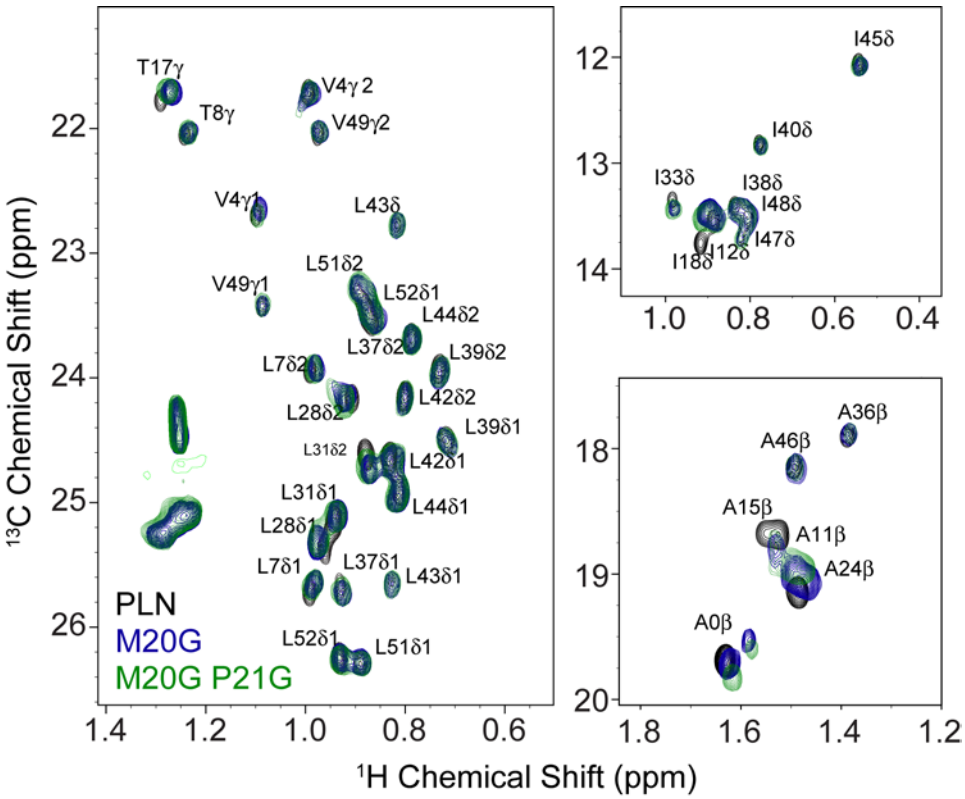

Fig 6.S3. Overlay of [^{1}H-^{13}C] HSQC spectra of AFA-PLN (black), AFA-PLN^{M20G} (navy), and AFA-PLN^{M20GP21G} (dark green) in 300 mM DPC at 37 °C.

BIBLIOGRAPHY

1. Torres, J., Stevens, T., and Samsó, M. (2003) Membrane Proteins: The 'Wild West' of Structural Biology. *Trends in Biochemical Sciences. 28*, 137-144.

2. Krueger-Koplin, R. D., Sorgen, P. L., Krueger-Koplin, S. T., Rivera-Torres, I. O., Cahill, S. M., Hicks, D. B., Grinius, L., Krulwich, T. A., and Girvin, M. E. (2004) An Evaluation of Detergents for NMR Structural Studies of Membrane Proteins. *J. Biomol. NMR. 28*, 43-57.

3. Carpenter, E. P., Beis, K., Cameron, A. D., and Iwata, S. (2008) Overcoming the Challenges of Membrane Protein Crystallography. *Curr. Opin. Struct. Biol. 18*, 581-586.

4. Shi, L., Traaseth, N. J., Verardi, R., Cembran, A., Gao, J., and Veglia, G. (2009) A Refinement Protocol to Determine Structure, Topology, and Depth of Insertion of Membrane Proteins using Hybrid Solution and Solid-State NMR Restraints. *J. Biomol. NMR. 44*, 195-205.

5. Traaseth, N. J., Shi, L., Verardi, R., Mullen, D. G., Barany, G., and Veglia, G. (2009) Structure and Topology of Monomeric Phospholamban in Lipid Membranes Determined by a Hybrid Solution and Solid-State NMR Approach. *Proc. Natl. Acad. Sci. U. S. A. 106*, 10165-10170.

6. Verardi, R., Shi, L., Traaseth, N. J., Walsh, N., and Veglia, G. (2011) Structural Topology of Phospholamban Pentamer in Lipid Bilayers by a Hybrid Solution and Solid-State NMR Method. *Proc. Natl. Acad. Sci. U. S. A. 108*, 9101-9106.

7. Veglia, G., and Ramamoorthy, A. (2010) Special Issue on "Membrane Protein Dynamics: Correlating Structure to Function". *Biochim. Biophys. Acta. 1798*, 65-67.

8. Ishima, R., and Torchia, D. A. (2000) Protein Dynamics from NMR. *Nat. Struct. Biol. 7*, 740-743.

9. AndrewAtkinson, R., and Kieffer, B. (2004) The Role of Protein Motions in Molecular Recognition: Insights from Heteronuclear NMR Relaxation Measurements. *Progress in Nuclear Magnetic Resonance Spectroscopy. 44*, 141-187.

10. Wang, C., and Palmer, A. G.,III. (2003) Solution NMR Methods for Quantitative Identification of Chemical Exchange in ^{15}N-Labeled Proteins. *Magn. Reson. Chem. 41*, 866-876.

11. Jarymowycz, V. A., and Stone, M. J. (2006) Fast Time Scale Dynamics of Protein Backbones: NMR Relaxation Methods, Applications, and Functional Consequences. *Chem. Rev. 106*, 1624-1671.

12. Bers, D. M. (2002) Cardiac Excitation-Contraction Coupling. *Nature. 415*, 198-205.

13. Simmerman, H. K., and Jones, L. R. (1998) Phospholamban: Protein Structure, Mechanism of Action, and Role in Cardiac Function. *Physiol. Rev. 78*, 921-947.

14. MacLennan, D. H., and Kranias, E. G. (2003) Phospholamban: A Crucial Regulator of Cardiac Contractility. *Nat. Rev. Mol. Cell Biol. 4*, 566-577.

15. Buffy, J. J., Buck-Koehntop, B. A., Porcelli, F., Traaseth, N. J., Thomas, D. D., and Veglia, G. (2006) Defining the Intramembrane Binding Mechanism of Sarcolipin to Calcium ATPase using Solution NMR Spectroscopy. *J. Mol. Biol. 358*, 420-429.

16. Colyer, J. (1998) Phosphorylation States of Phospholamban. *Ann. N. Y. Acad. Sci. 853*, 79-91.

17. Gramolini, A. O., Trivieri, M. G., Oudit, G. Y., Kislinger, T., Li, W., Patel, M. M., Emili, A., Kranias, E. G., Backx, P. H., and Maclennan, D. H. (2006) Cardiac-Specific Overexpression of Sarcolipin in Phospholamban Null Mice Impairs Myocyte Function that is Restored by Phosphorylation. *Proc. Natl. Acad. Sci. U. S. A. 103*, 2446-2451.

18. Reddy, L. G., Jones, L. R., and Thomas, D. D. (1999) Depolymerization of Phospholamban in the Presence of Calcium Pump: A Fluorescence Energy Transfer Study. *Biochemistry. 38*, 3954-3962.

19. Kimura, Y., Kurzydlowski, K., Tada, M., and MacLennan, D. H. (1997) Phospholamban Inhibitory Function is Activated by Depolymerization. *J. Biol. Chem. 272*, 15061-15064.

20. Gustavsson, M., Traaseth, N. J., and Veglia, G. (2012) Probing Ground and Excited States of Phospholamban in Model and Native Lipid Membranes by Magic Angle Spinning NMR Spectroscopy. *Biochim. Biophys. Acta. 1818*, 146-153.

21. Traaseth, N. J., and Veglia, G. (2010) Probing Excited States and Activation Energy for the Integral Membrane Protein Phospholamban by NMR CPMG Relaxation Dispersion Experiments. *Biochim. Biophys. Acta. 1798*, 77-81.

22. Metcalfe, E. E., Zamoon, J., Thomas, D. D., and Veglia, G. (2004) (1)H/(15)N Heteronuclear NMR Spectroscopy shows Four Dynamic Domains for Phospholamban Reconstituted in Dodecylphosphocholine Micelles. *Biophys. J. 87*, 1205-1214.

23. Gustavsson, M., Traaseth, N. J., Karim, C. B., Lockamy, E. L., Thomas, D. D., and Veglia, G. (2011) Lipid-Mediated Folding/Unfolding of Phospholamban as a Regulatory Mechanism for the Sarcoplasmic Reticulum Ca(2+)-ATPase. *J. Mol. Biol.*

24. Masterson, L. R., Yu, T., Shi, L., Wang, Y., Gustavsson, M., Mueller, M. M., and Veglia, G. (2011) CAMP-Dependent Protein Kinase A Selects the Excited State of the Membrane Substrate Phospholamban. *J. Mol. Biol. 412*, 155-164.

25. Ha, K. N., Traaseth, N. J., Verardi, R., Zamoon, J., Cembran, A., Karim, C. B., Thomas, D. D., and Veglia, G. (2007) Controlling the Inhibition of the Sarcoplasmic Ca2+-ATPase by Tuning Phospholamban Structural Dynamics. *J. Biol. Chem. 282*, 37205-37214.

26. *American Heart Association.*

27. Haghighi, K., Gregory, K. N., and Kranias, E. G. (2004) Sarcoplasmic Reticulum Ca-ATPase-Phospholamban Interactions and Dilated Cardiomyopathy. *Biochem. Biophys. Res. Commun. 322*, 1214-1222.

28. Schmitt, J. P., Kamisago, M., Asahi, M., Li, G. H., Ahmad, F., Mende, U., Kranias, E. G., MacLennan, D. H., Seidman, J. G., and Seidman, C. E. (2003) Dilated Cardiomyopathy and Heart Failure Caused by a Mutation in Phospholamban. *Science. 299*, 1410-1413.

29. Medeiros, A., Biagi, D. G., Sobreira, T. J., de Oliveira, P. S., Negrao, C. E., Mansur, A. J., Krieger, J. E., Brum, P. C., and Pereira, A. C. (2011) Mutations in the Human Phospholamban Gene in Patients with Heart Failure. *Am. Heart J. 162*, 1088-1095.e1.

30. Haghighi, K., Kolokathis, F., Gramolini, A. O., Waggoner, J. R., Pater, L., Lynch, R. A., Fan, G. C., Tsiapras, D., Parekh, R. R., Dorn, G. W.,2nd, MacLennan, D. H., Kremastinos, D. T., and Kranias, E. G. (2006) A Mutation in the Human Phospholamban Gene, Deleting

Arginine 14, Results in Lethal, Hereditary Cardiomyopathy. *Proc. Natl. Acad. Sci. U. S. A. 103*, 1388-1393.

31. Haghighi, K., Kolokathis, F., Pater, L., Lynch, R. A., Asahi, M., Gramolini, A. O., Fan, G. C., Tsiapras, D., Hahn, H. S., Adamopoulos, S., Liggett, S. B., Dorn, G. W.,2nd, MacLennan, D. H., Kremastinos, D. T., and Kranias, E. G. (2003) Human Phospholamban Null Results in Lethal Dilated Cardiomyopathy Revealing a Critical Difference between Mouse and Human. *J. Clin. Invest. 111*, 869-876.

32. Hoshijima, M., Ikeda, Y., Iwanaga, Y., Minamisawa, S., Date, M. O., Gu, Y., Iwatate, M., Li, M., Wang, L., Wilson, J. M., Wang, Y., Ross, J.,Jr, and Chien, K. R. (2002) Chronic Suppression of Heart-Failure Progression by a Pseudophosphorylated Mutant of Phospholamban Via in Vivo Cardiac rAAV Gene Delivery. *Nat. Med. 8*, 864-871.

33. Kaye, D. M., Preovolos, A., Marshall, T., Byrne, M., Hoshijima, M., Hajjar, R., Mariani, J. A., Pepe, S., Chien, K. R., and Power, J. M. (2007) Percutaneous Cardiac Recirculation-Mediated Gene Transfer of an Inhibitory Phospholamban Peptide Reverses Advanced Heart Failure in Large Animals. *J. Am. Coll. Cardiol. 50*, 253-260.

34. MacLennan, D. H., Kimura, Y., and Toyofuku, T. (1998) Sites of Regulatory Interaction between Calcium ATPases and Phospholamban. *Ann. N. Y. Acad. Sci. 853*, 31-42.

35. Afara, M. R., Trieber, C. A., Glaves, J. P., and Young, H. S. (2006) Rational Design of Peptide Inhibitors of the Sarcoplasmic Reticulum Calcium Pump. *Biochemistry. 45*, 8617-8627.

36. Mortishire-Smith, R. J., Pitzenberger, S. M., Burke, C. J., Middaugh, C. R., Garsky, V. M., and Johnson, R. G. (1995) Solution Structure of the Cytoplasmic Domain of Phopholamban: Phosphorylation Leads to a Local Perturbation in Secondary Structure. *Biochemistry. 34*, 7603-7613.

37. Oxenoid, K., and Chou, J. J. (2005) The Structure of Phospholamban Pentamer Reveals a Channel-Like Architecture in Membranes. *Proc. Natl. Acad. Sci. U. S. A. 102*, 10870-10875.

38. Karim, C. B., Zhang, Z., Howard, E. C., Torgersen, K. D., and Thomas, D. D. (2006) Phosphorylation-Dependent Conformational Switch in Spin-Labeled Phospholamban Bound to SERCA. *J. Mol. Biol. 358*, 1032-1040.

39. Robia, S. L., Campbell, K. S., Kelly, E. M., Hou, Z., Winters, D. L., and Thomas, D. D. (2007) Forster Transfer Recovery Reveals that Phospholamban Exchanges Slowly from Pentamers but Rapidly from the SERCA Regulatory Complex. *Circ. Res. 101*, 1123-1129.

40. Robia, S. L., Flohr, N. C., and Thomas, D. D. (2005) Phospholamban Pentamer Quaternary Conformation Determined by in-Gel Fluorescence Anisotropy. *Biochemistry. 44*, 4302-4311.

41. Veglia, G., Ha, K. N., Shi, L., Verardi, R., and Traaseth, N. J. (2010) What can we Learn from a Small Regulatory Membrane Protein? *Methods Mol. Biol. 654*, 303-319.

42. Case, D. A., Dyson, H. J., and Wright, P. E. (1994) Use of Chemical Shifts and Coupling Constants in Nuclear Magnetic Resonance Structural Studies on Peptides and Proteins. *Methods Enzymol. 239*, 392-416.

43. Oldfield, E. (1995) Chemical Shifts and Three-Dimensional Protein Structures. *J. Biomol. NMR. 5*, 217-225.

44. Wüthrich, K. (1986) *NMR of Proteins and Nucleic Acids.* New York : Wiley, New York.

45. Wishart, D. S., Sykes, B. D., and Richards, F. M. (1991) Relationship between Nuclear Magnetic Resonance Chemical Shift and Protein Secondary Structure. *J. Mol. Biol. 222*, 311-333.

46. Ikura, M., Kay, L., Tschudin, R., and Bax, A. (1990) 3-Dimensional NOESY-HMQC Spectroscopy of a C^1 Labeled Protein. *Journal of Magnetic Resonance. 86*, 204-209.

47. Marion, D., Driscoll, P. C., Kay, L. E., Wingfield, P. T., Bax, A., Gronenborn, A. M., and Clore, G. M. (1989) Overcoming the Overlap Problem in the Assignment of 1H NMR Spectra of Larger Proteins by use of Three-Dimensional Heteronuclear 1H-15N Hartmann-Hahn-Multiple Quantum Coherence and Nuclear Overhauser-Multiple Quantum Coherence Spectroscopy: Application to Interleukin 1 Beta. *Biochemistry. 28*, 6150-6156.

48. Bodenhausen, G., and Ruben, D. J. (1980) Natural Abundance Nitrogen-15 NMR by Enhanced Heteronuclear Spectroscopy. *Chem Phys Lett. 60*, 185.

49. Zwahlen, C., Vincent, S., Dibari, L., Levitt, M., and Bodenhausen, G. (1994) Quenching Spin-Diffusion in Selective Measurements of Transient Overhauser Effects in Nuclear-Magnetic-Resonance - Applications to Oligonucleotides Rid B-3746-2010. *J. Am. Chem. Soc. 116*, 362-368.

50. Marion, D., Kay, L. E., Sparks, S. W., Torchia, D. A., and Bax, A. (1989) Three-Dimensional Heteronuclear NMR of Nitrogen-15 Labeled Proteins. *J. Am. Chem. Soc. 111*, 1515-1517.

51. Zuiderweg, E. R., and Fesik, S. W. (1989) Heteronuclear Three-Dimensional NMR Spectroscopy of the Inflammatory Protein C5a. *Biochemistry. 28*, 2387-2391.

52. Cavanagh, J., Fairbrother, W., Palmer, A., and Skelton, N. (1996) *Protein NMR Spectroscopy Principles and Practice.* Academic Press, San Diego.

53. Roberts, G., and Lian, L. Y. (2011) *Protein NMR Spectroscopy: Practical Techniques and Applications.* John Wiley & Sons, .

54. Hartmann, S. R., and Hahn, E. L. (1962) Nuclear Double Resonance in the Rotating Frame. *Phys. Rev. 128*, 2042-2053.

55. Hore, P. J. (1995) *Nuclear Magnetic Resonance.* Oxford University Press, Oxford.

56. Claridge, T. (1999) *High-Resolution NMR Techniques in Organic Chemistry.* Pergamon, Oxford.

57. Zamoon, J., Mascioni, A., Thomas, D. D., and Veglia, G. (2003) NMR Solution Structure and Topological Orientation of Monomeric Phospholamban in Dodecylphosphocholine Micelles. *Biophys. J. 85*, 2589-2598.

58. Overhauser, A. W. (1953) Polarization of Nuclei in Metals. *Phys. Rev. 92*, 411-415.

59. Neuhaus, D., and Williamson, M. (2000) *The Nuclear Overhauser Effect in Structural and Conformational Analysis.* Wiley-VCH Inc, United States.

60. Levitt, M. (2001) *Spin Dynamics.* John Wiley & Sons Ltd, West Sussex.

61. Solomon, I. (1955) Relaxation Processes in a System of Two Spins. *Phys. Rev. 99*, 559-565.

62. Zuiderweg, E. R. (2002) Mapping Protein-Protein Interactions in Solution by NMR Spectroscopy. *Biochemistry. 41*, 1-7.

63. Mori, S., Abeygunawardana, C., Johnson, M. O., and van Zijl, P. C. (1995) Improved Sensitivity of HSQC Spectra of Exchanging Protons at Short Interscan Delays using a New Fast HSQC (FHSQC) Detection Scheme that Avoids Water Saturation. *J. Magn. Reson. B. 108*, 94-98.

64. Heisenberg, ,W. (1927) Ãœber Den Anschaulichen Inhalt Der Quantentheoretischen Kinematik Und Mechanik. *Zeitschrift fÃ¼r Physik A Hadrons and Nuclei.* , 172-198.

65. Frey, T., Anglister, J., and McConnell, H. M. (1988) Line-Shape Analysis of NMR Difference Spectra of an Anti-Spin-Label Antibody. *Biochemistry. 27*, 5161-5165.

66. Matsuo, H., Walters, K. J., Teruya, K., Tanaka, T., Gassner, G. T., Lippard, S. J., Kyogoku, Y., and Wagner, G. (1999) Identification by NMR Spectroscopy of Residues at Contact Surfaces in Large, Slowly Exchanging Macromolecular Complexes. *J. Am. Chem. Soc. 121*, 9903-9904.

67. Lompre, A. M., Hajjar, R. J., Harding, S. E., Kranias, E. G., Lohse, M. J., and Marks, A. R. (2010) Ca2+ Cycling and New Therapeutic Approaches for Heart Failure. *Circulation. 121*, 822-830.

68. Pieske, B., Sutterlin, M., Schmidt-Schweda, S., Minami, K., Meyer, M., Olschewski, M., Holubarsch, C., Just, H., and Hasenfuss, G. (1996) Diminished Post-Rest Potentiation of Contractile Force in Human Dilated Cardiomyopathy. Functional Evidence for Alterations in Intracellular Ca2+ Handling. *J. Clin. Invest. 98*, 764-776.

69. Kaye, D. M., Hoshijima, M., and Chien, K. R. (2008) Reversing Advanced Heart Failure by Targeting Ca2+ Cycling. *Annu. Rev. Med. 59*, 13-28.

70. Lipskaia, L., Chemaly, E. R., Hadri, L., Lompre, A. M., and Hajjar, R. J. (2010) Sarcoplasmic Reticulum Ca(2+) ATPase as a Therapeutic Target for Heart Failure. *Expert Opin. Biol. Ther. 10*, 29-41.

71. Vinge, L. E., Raake, P. W., and Koch, W. J. (2008) Gene Therapy in Heart Failure. *Circ. Res. 102*, 1458-1470.

72. Schwinger, R. H., Bohm, M., Schmidt, U., Karczewski, P., Bavendiek, U., Flesch, M., Krause, E. G., and Erdmann, E. (1995) Unchanged Protein Levels of SERCA II and Phospholamban but Reduced Ca2+ Uptake and Ca(2+)-ATPase Activity of Cardiac Sarcoplasmic Reticulum from Dilated Cardiomyopathy Patients Compared with Patients with Nonfailing Hearts. *Circulation. 92*, 3220-3228.

73. Tilemann, L., Ishikawa, K., Weber, T., and Hajjar, R. J. (2012) Gene Therapy for Heart Failure. *Circ. Res. 110*, 777-793.

74. Iwanaga, Y., Hoshijima, M., Gu, Y., Iwatate, M., Dieterle, T., Ikeda, Y., Date, M. O., Chrast, J., Matsuzaki, M., Peterson, K. L., Chien, K. R., and Ross, J.,Jr. (2004) Chronic Phospholamban Inhibition Prevents Progressive Cardiac Dysfunction and Pathological Remodeling After Infarction in Rats. *J. Clin. Invest. 113*, 727-736.

75. Vandecaetsbeek, I., Raeymaekers, L., Wuytack, F., and Vangheluwe, P. (2009) Factors Controlling the Activity of the SERCA2a Pump in the Normal and Failing Heart. *Biofactors. 35*, 484-499.

76. He, H., Meyer, M., Martin, J. L., McDonough, P. M., Ho, P., Lou, X., Lew, W. Y., Hilal-Dandan, R., and Dillmann, W. H. (1999) Effects of Mutant and Antisense RNA of Phospholamban on SR Ca(2+)-ATPase Activity and Cardiac Myocyte Contractility. *Circulation. 100*, 974-980.

77. Vangheluwe, P., Raeymaekers, L., Dode, L., and Wuytack, F. (2005) Modulating Sarco(Endo)Plasmic Reticulum Ca2+ ATPase 2 (SERCA2) Activity: Cell Biological Implications. *Cell Calcium. 38*, 291-302.

78. Zhang, O., Kay, L. E., Olivier, J. P., and Forman-Kay, J. D. (1994) Backbone 1H and 15N Resonance Assignments of the N-Terminal SH3 Domain of Drk in Folded and Unfolded States using Enhanced-Sensitivity Pulsed Field Gradient NMR Techniques. *J. Biomol. NMR. 4*, 845-858.

79. Farrow, N., Muhandiram, R., Singer, A., Pascal, S., Kay, C., Gish, G., Shoelson, S., Pawson, T., Forman-Kay, J., and Kay, L. (1994) Backbone Dynamics of a Free and a Phosphopeptide-Complexed Src Homology 2 Domain Studied by 15N NMR Relaxation. *Biochemistry. 33*, 5984-6003.

80. Wegener, A. D., Simmerman, H. K., Lindemann, J. P., and Jones, L. R. (1989) Phospholamban Phosphorylation in Intact Ventricles. Phosphorylation of Serine 16 and Threonine 17 in Response to Beta-Adrenergic Stimulation. *J. Biol. Chem. 264*, 11468-11474.

81. Mundina-Weilenmann, C., Vittone, L., Ortale, M., de Cingolani, G. C., and Mattiazzi, A. (1996) Immunodetection of Phosphorylation Sites Gives New Insights into the Mechanisms Underlying Phospholamban Phosphorylation in the Intact Heart. *J. Biol. Chem. 271*, 33561-33567.

82. Chu, G., Lester, J. W., Young, K. B., Luo, W., Zhai, J., and Kranias, E. G. (2000) A Single Site (Ser16) Phosphorylation in Phospholamban is Sufficient in Mediating its Maximal Cardiac Responses to Beta -Agonists. *J. Biol. Chem. 275*, 38938-38943.

83. Wawrzynow, A., Theibert, J. L., Murphy, C., Jona, I., Martonosi, A., and Collins, J. H. (1992) Sarcolipin, the "Proteolipid" of Skeletal Muscle Sarcoplasmic Reticulum, is a Unique, Amphipathic, 31-Residue Peptide. *Arch. Biochem. Biophys. 298*, 620-623.

84. Odermatt, A., Taschner, P. E., Scherer, S. W., Beatty, B., Khanna, V. K., Cornblath, D. R., Chaudhry, V., Yee, W. C., Schrank, B., Karpati, G., Breuning, M. H., Knoers, N., and MacLennan, D. H. (1997) Characterization of the Gene Encoding Human Sarcolipin (SLN), a Proteolipid Associated with SERCA1: Absence of Structural Mutations in Five Patients with Brody Disease. *Genomics. 45*, 541-553.

85. Gayan-Ramirez, G., Vanzeir, L., Wuytack, F., and Decramer, M. (2000) Corticosteroids Decrease mRNA Levels of SERCA Pumps, Whereas they Increase Sarcolipin mRNA in the Rat Diaphragm. *J. Physiol. 524 Pt 2*, 387-397.

86. Minamisawa, S., Wang, Y., Chen, J., Ishikawa, Y., Chien, K. R., and Matsuoka, R. (2003) Atrial Chamber-Specific Expression of Sarcolipin is Regulated during Development and Hypertrophic Remodeling. *J. Biol. Chem. 278*, 9570-9575.

87. Babu, G. J., Bhupathy, P., Carnes, C. A., Billman, G. E., and Periasamy, M. (2007) Differential Expression of Sarcolipin Protein during Muscle Development and Cardiac Pathophysiology. *J. Mol. Cell. Cardiol. 43*, 215-222.

88. Maclennan, D. H., Yip, C., Iles, C., and Seeman, P. (1972) Isolation of Sarcoplasmic Reticulum Proteins. *Cold Spring Harbor Symp. Quant. Biol. 37*, 469-478.

89. Odermatt, A., Becker, S., Khanna, V. K., Kurzydlowski, K., Leisner, E., Pette, D., and MacLennan, D. H. (1998) Sarcolipin Regulates the Activity of SERCA1, the Fast-Twitch Skeletal Muscle Sarcoplasmic Reticulum Ca2+-ATPase. *J. Biol. Chem. 273*, 12360-12369.

90. Uemura, N., Ohkusa, T., Hamano, K., Nakagome, M., Hori, H., Shimizu, M., Matsuzaki, M., Mochizuki, S., Minamisawa, S., and Ishikawa, Y. (2004) Down-Regulation of Sarcolipin mRNA Expression in Chronic Atrial Fibrillation. *Eur. J. Clin. Invest. 34*, 723-730.

91. Toyoshima, C., Nakasako, M., Nomura, H., and Ogawa, H. (2000) Crystal Structure of the Calcium Pump of Sarcoplasmic Reticulum at 2.6 A Resolution. *Nature. 405*, 647-655.

92. Toyoshima, C., and Nomura, H. (2002) Structural Changes in the Calcium Pump Accompanying the Dissociation of Calcium. *Nature. 418*, 605-611.

93. Toyoshima, C., Nomura, H., and Tsuda, T. (2004) Lumenal Gating Mechanism Revealed in Calcium Pump Crystal Structures with Phosphate Analogues. *Nature. 432*, 361-368.

94. Toyoshima, C., and Mizutani, T. (2004) Crystal Structure of the Calcium Pump with a Bound ATP Analogue. *Nature. 430*, 529-535.

95. Olesen, C., Sorensen, T. L., Nielsen, R. C., Moller, J. V., and Nissen, P. (2004) Dephosphorylation of the Calcium Pump Coupled to Counterion Occlusion. *Science. 306*, 2251-2255.

96. Sorensen, T. L., Moller, J. V., and Nissen, P. (2004) Phosphoryl Transfer and Calcium Ion Occlusion in the Calcium Pump. *Science. 304*, 1672-1675.

97. Young, H. S., Jones, L. R., and Stokes, D. L. (2001) Locating Phospholamban in Co-Crystals with Ca(2+)-ATPase by Cryoelectron Microscopy. *Biophys. J. 81*, 884-894.

98. Toyoshima, C., Asahi, M., Sugita, Y., Khanna, R., Tsuda, T., and MacLennan, D. H. (2003) Modeling of the Inhibitory Interaction of Phospholamban with the Ca2+ ATPase. *Proc. Natl. Acad. Sci. U. S. A. 100*, 467-472.

99. Asahi, M., Sugita, Y., Kurzydlowski, K., De Leon, S., Tada, M., Toyoshima, C., and MacLennan, D. H. (2003) Sarcolipin Regulates Sarco(Endo)Plasmic Reticulum Ca2+-ATPase (SERCA) by Binding to Transmembrane Helices Alone Or in Association with Phospholamban. *Proc. Natl. Acad. Sci. U. S. A. 100*, 5040-5045.

100. Hutter, M. C., Krebs, J., Meiler, J., Griesinger, C., Carafoli, E., and Helms, V. (2002) A Structural Model of the Complex Formed by Phospholamban and the Calcium Pump of Sarcoplasmic Reticulum obtained by Molecular Mechanics. *Chembiochem. 3*, 1200-1208.

101. Buck, B., Zamoon, J., Kirby, T. L., DeSilva, T. M., Karim, C., Thomas, D., and Veglia, G. (2003) Overexpression, Purification, and Characterization of Recombinant Ca-ATPase Regulators for High-Resolution Solution and Solid-State NMR Studies. *Protein Expr. Purif. 30*, 253-261.

102. Traaseth, N. J., Thomas, D. D., and Veglia, G. (2006) Effects of Ser16 Phosphorylation on the Allosteric Transitions of phospholamban/Ca(2+)-ATPase Complex. *J. Mol. Biol. 358*, 1041-1050.

103. Pollesello, P., Annila, A., and Ovaska, M. (1999) Structure of the 1-36 Amino-Terminal Fragment of Human Phospholamban by Nuclear Magnetic Resonance and Modeling of the Phospholamban Pentamer. *Biophys. J. 76*, 1784-1795.

104. Lamberth, S., Schmid, H., Muenchbach, M., Vorherr, T., Krebs, J., Carafoli, E., and Griesinger, C. (2000) NMR Solution Structure of Phospholamban. *HCA. 83*, 2141-2152.

105. Metcalfe, E. E., Traaseth, N. J., and Veglia, G. (2005) Serine 16 Phosphorylation Induces an Order-to-Disorder Transition in Monomeric Phospholamban. *Biochemistry. 44*, 4386-4396.

106. Schmidt, A. G., Zhai, J., Carr, A. N., Gerst, M. J., Lorenz, J. N., Pollesello, P., Annila, A., Hoit, B. D., and Kranias, E. G. (2002) Structural and Functional Implications of the Phospholamban Hinge Domain: Impaired SR Ca2+ Uptake as a Primary Cause of Heart Failure. *Cardiovasc. Res. 56*, 248-259.

107. Traaseth, N. J., Verardi, R., Torgersen, K. D., Karim, C. B., Thomas, D. D., and Veglia, G. (2007) Spectroscopic Validation of the Pentameric Structure of Phospholamban. *Proc. Natl. Acad. Sci. U. S. A. 104*, 14676-14681.

108. Mascioni, A., Karim, C., Barany, G., Thomas, D. D., and Veglia, G. (2002) Structure and Orientation of Sarcolipin in Lipid Environments. *Biochemistry. 41*, 475-482.

109. Opella, S. J., Ma, C., and Marassi, F. M. (2001) Nuclear Magnetic Resonance of Membrane-Associated Peptides and Proteins, in *Methods in Enzymology* (Thomas L. James,Volker Dotsch and Uli Schmitz, Ed.) pp 285-313, Academic Press, .

110. Baldus, M. (2006) Molecular Interactions Investigated by Multi-Dimensional Solid-State NMR. *Curr. Opin. Struct. Biol. 16*, 618-623.

111. Mascioni, A., Karim, C., Zamoon, J., Thomas, D. D., and Veglia, G. (2002) Solid-State NMR and Rigid Body Molecular Dynamics to Determine Domain Orientations of Monomeric Phospholamban. *J. Am. Chem. Soc. 124*, 9392-9393.

112. Wu, C. H., Ramamoorthy, A., and Opella, S. J. (1994) High-Resolution Heteronuclear Dipolar Solid-State NMR Spectroscopy. *Journal of Magnetic Resonance, Series A. 109*, 270-272.

113. Traaseth, N. J., Buffy, J. J., Zamoon, J., and Veglia, G. (2006) Structural Dynamics and Topology of Phospholamban in Oriented Lipid Bilayers using Multidimensional Solid-State NMR. *Biochemistry. 45*, 13827-13834.

114. Grage, S. L., Wang, J., Cross, T. A., and Ulrich, A. S. (2002) Solid-State 19F-NMR Analysis of 19F-Labeled Tryptophan in Gramicidin A in Oriented Membranes. *Biophys. J. 83*, 3336-3350.

115. Aisenbrey, C., and Bechinger, B. (2004) Investigations of Polypeptide Rotational Diffusion in Aligned Membranes by 2H and 15N Solid-State NMR Spectroscopy. *J. Am. Chem. Soc. 126*, 16676-16683.

116. Park, S. H., Mrse, A. A., Nevzorov, A. A., De Angelis, A. A., and Opella, S. J. (2006) Rotational Diffusion of Membrane Proteins in Aligned Phospholipid Bilayers by Solid-State NMR Spectroscopy. *J. Magn. Reson. 178*, 162-165.

117. Andronesi, O. C., Becker, S., Seidel, K., Heise, H., Young, H. S., and Baldus, M. (2005) Determination of Membrane Protein Structure and Dynamics by Magic-Angle-Spinning Solid-State NMR Spectroscopy. *J. Am. Chem. Soc. 127*, 12965-12974.

118. Hughes, E., Clayton, J. C., and Middleton, D. A. (2005) Probing the Oligomeric State of Phospholamban Variants in Phospholipid Bilayers from Solid-State NMR Measurements of Rotational Diffusion Rates. *Biochemistry. 44*, 4055-4066.

119. Karp, E. S., Tiburu, E. K., Abu-Baker, S., and Lorigan, G. A. (2006) The Structural Properties of the Transmembrane Segment of the Integral Membrane Protein Phospholamban Utilizing (13)C CPMAS, (2)H, and REDOR Solid-State NMR Spectroscopy. *Biochim. Biophys. Acta. 1758*, 772-780.

120. Buffy, J. J., Traaseth, N. J., Mascioni, A., Gor'kov, P. L., Chekmenev, E. Y., Brey, W. W., and Veglia, G. (2006) Two-Dimensional Solid-State NMR Reveals Two Topologies of Sarcolipin in Oriented Lipid Bilayers. *Biochemistry. 45*, 10939-10946.

121. Stokes, D. L., Pomfret, A. J., Rice, W. J., Glaves, J. P., and Young, H. S. (2006) Interactions between Ca2+-ATPase and the Pentameric Form of Phospholamban in Two-Dimensional Co-Crystals. *Biophys. J. 90*, 4213-4223.

122. Tatulian, S. A., Jones, L. R., Reddy, L. G., Stokes, D. L., and Tamm, L. K. (1995) Secondary Structure and Orientation of Phospholamban Reconstituted in Supported Bilayers from Polarized Attenuated Total Reflection FTIR Spectroscopy. *Biochemistry. 34*, 4448-4456.

123. Arkin, I. T., Rothman, M., Ludlam, C. F., Aimoto, S., Engelman, D. M., Rothschild, K. J., and Smith, S. O. (1995) Structural Model of the Phospholamban Ion Channel Complex in Phospholipid Membranes. *J. Mol. Biol. 248*, 824-834.

124. Smith, S. O., Kawakami, T., Liu, W., Ziliox, M., and Aimoto, S. (2001) Helical Structure of Phospholamban in Membrane Bilayers. *J. Mol. Biol. 313*, 1139-1148.

125. Simmerman, H. K., Kobayashi, Y. M., Autry, J. M., and Jones, L. R. (1996) A Leucine Zipper Stabilizes the Pentameric Membrane Domain of Phospholamban and Forms a Coiled-Coil Pore Structure. *J. Biol. Chem. 271*, 5941-5946.

126. Karim, C. B., Stamm, J. D., Karim, J., Jones, L. R., and Thomas, D. D. (1998) Cysteine Reactivity and Oligomeric Structures of Phospholamban and its Mutants. *Biochemistry. 37*, 12074-12081.

127. Zamoon, J., Nitu, F., Karim, C., Thomas, D. D., and Veglia, G. (2005) Mapping the Interaction Surface of a Membrane Protein: Unveiling the Conformational Switch of Phospholamban in Calcium Pump Regulation. *Proc. Natl. Acad. Sci. U. S. A. 102*, 4747-4752.

128. Karim, C. B., Kirby, T. L., Zhang, Z., Nesmelov, Y., and Thomas, D. D. (2004) Phospholamban Structural Dynamics in Lipid Bilayers Probed by a Spin Label Rigidly Coupled to the Peptide Backbone. *Proc. Natl. Acad. Sci. U. S. A. 101*, 14437-14442.

129. Wagner, G., Pardi, A., and Wuethrich, K. (1983) Hydrogen Bond Length and Proton NMR Chemical Shifts in Proteins. *J. Am. Chem. Soc. 105*, 5948-5949.

130. Kimura, Y., Asahi, M., Kurzydlowski, K., Tada, M., and MacLennan, D. H. (1998) Phospholamban Domain Ib Mutations Influence Functional Interactions with the Ca2+-ATPase Isoform of Cardiac Sarcoplasmic Reticulum. *J. Biol. Chem. 273*, 14238-14241.

131. Inesi, G., Lewis, D., Ma, H., Prasad, A., and Toyoshima, C. (2006) Concerted Conformational Effects of Ca2+ and ATP are Required for Activation of Sequential Reactions in the Ca2+ ATPase (SERCA) Catalytic Cycle. *Biochemistry. 45*, 13769-13778.

132. Kranias, E. G., and Bers, D. M. (2007) Calcium and Cardiomyopathies. *Subcell. Biochem. 45*, 523-537.

133. Hoshijima, M., Knoll, R., Pashmforoush, M., and Chien, K. R. (2006) Reversal of Calcium Cycling Defects in Advanced Heart Failure Toward Molecular Therapy. *J. Am. Coll. Cardiol. 48*, A15-23.

134. Toyoshima, C., and Inesi, G. (2004) Structural Basis of Ion Pumping by Ca2+-ATPase of the Sarcoplasmic Reticulum. *Annu. Rev. Biochem. 73*, 269-292.

135. Inesi, G., Prasad, A. M., and Pilankatta, R. (2008) The Ca2+ ATPase of Cardiac Sarcoplasmic Reticulum: Physiological Role and Relevance to Diseases *Biochem. Biophys. Res. Commun. 369*, 182-187.

136. Negash, S., Yao, Q., Sun, H., Li, J., Bigelow, D. J., and Squier, T. C. (2000) Phospholamban Remains Associated with the Ca2+- and Mg2+-Dependent ATPase Following Phosphorylation by cAMP-Dependent Protein Kinase. *Biochem. J. 351*, 195-205.

137. Negash, S., Sun, H., Yao, Q., FAU, G., S.Y., Bigelow, D. J., and Squier, T. C. (1998) Cytosolic Domain of Phospholamban Remains Associated with the Ca-ATPase Following Phosphorylation by cAMP-Dependent Protein Kinase. *Ann. N. Y. Acad. Sci. 853*, 288-291.

138. Negash, S., Che, L. T., Bigelow, D. J., and Squier, T. C. (1996) *Phosphorylation of Phospholamban by cAMP-Dependent Protein Kinase Enhances Interactions between Ca-ATPase Polypeptide Chains in Cardiac Sarcoplasmic Reticulum Membranes.* 35(35):11247-59.

139. Kirby, T. L., Karim, C. B., and Thomas, D. D. (2004) Electron Paramagnetic Resonance Reveals a Large-Scale Conformational Change in the Cytoplasmic Domain of Phospholamban upon Binding to the Sarcoplasmic Reticulum Ca-ATPase. *Biochemistry.* 43(19):5842-52

140. Stokes, D. L., and Green, N. M. (1990) Three-Dimensional Crystals of CaATPase from Sarcoplasmic Reticulum. Symmetry and Molecular Packing. *Biophys. J. 57*, 1-14.

141. Mueller, B., Karim, C. B., Negrashov, I. V., Kutchai, H., and Thomas, D. D. (2004) Direct Detection of Phospholamban and Sarcoplasmic Reticulum Ca-ATPase Interaction in Membranes using Fluorescence Resonance Energy Transfer. *Biochemistry. 43*, 8754-8765.

142. Traaseth, N. J., Ha, K. N., Verardi, R., Shi, L., Buffy, J. J., Masterson, L. R., and Veglia, G. (2008) Structural and Dynamic Basis of Phospholamban and Sarcolipin Inhibition of Ca(2+)-ATPase. *Biochemistry. 47*, 3-13.

143. Douglas, J. L., Trieber, C. A., Afara, M., and Young, H. S. (2005) Rapid, High-Yield Expression and Purification of Ca2+-ATPase Regulatory Proteins for High-Resolution Structural Studies. *Protein Expr. Purif. 40*, 118-125.

144. Madden, T. D., Chapman, D., and Quinn, P. J. (1979) Cholesterol Modulates Activity of Calcium-Dependent ATPase of the Sarcoplasmic Reticulum. *Nature. 279*, 538-541.

145. Fabiato, A., and Fabiato, F. (1978) Calcium-induced Release of Calcium from the Sarcoplasmic Reticulum of Skinned Cells from Adult Human, Dog, Cat, Rabbit, Rat, and Frog Hearts and from Fetal and New-Born Rat Ventricles. *Ann. N. Y. Acad. Sci. 307*, 491-522.

146. Kay, L., Keifer, P., and Saarinen, T. (1992) Pure Absorption Gradient Enhanced Heteronuclear Single Quantum Correlation Spectroscopy with Improved Sensitivity. *J. Am. Chem. Soc. 114*, 10663-10665.

147. Ramamoorthy, A., Wei, Y., and Lee, D. PISEMA Solid-State NMR Spectroscopy, in *Annual Reports on NMR Spectroscopy* pp 1-52, Academic Press, .

148. Bennett, A. E., Rienstra, C. M., Auger, M., Lakshmi, K. V., and Griffin, R. G. (1995) Heteronuclear Decoupling in Rotating Solids. *J. Chem. Phys. 103*, 6951-6958.

149. Vinogradov, E., Madhu, P. K., and Vega, S. (1999) High-Resolution Proton Solid-State NMR Spectroscopy by Phase-Modulated Lee–Goldburg Experiment. *Chemical Physics Letters. 314*, 443-450.

150. Gor'kov, P. L., Chekmenev, E. Y., Li, C., Cotten, M., Buffy, J. J., Traaseth, N. J., Veglia, G., and Brey, W. W. (2007) Using Low-E Resonators to Reduce RF Heating in Biological Samples for Static Solid-State NMR Up to 900 MHz. *J. Magn. Reson. 185*, 77-93.

151. Opella, S. J., and Marassi, F. M. (2004) Structure Determination of Membrane Proteins by NMR Spectroscopy. *Chem. Rev. 104*, 3587-3606.

152. Gao, F. P., and Cross, T. A. (2005) Recent Developments in Membrane-Protein Structural Genomics. *Genome Biol. 6*, 244.

153. Schwieters, C. D., Kuszewski, J. J., Tjandra, N., and Clore, G. M. (2003) The Xplor-NIH NMR Molecular Structure Determination Package. *J. Magn. Reson. 160*, 65-73.

154. MacLennan, D. H. (2000) Ca2+ Signalling and Muscle Disease. *Eur. J. Biochem. 267*, 5291-5297.

155. Bers, D. M., Despa, S., and Bossuyt, J. (2006) Regulation of Ca2+ and Na+ in Normal and Failing Cardiac Myocytes. *Ann. N. Y. Acad. Sci. 1080*, 165-177.

156. MacLennan, D. H., Abu-Abed, M., and Kang, C. (2002) Structure-Function Relationships in Ca(2+) Cycling Proteins. *J. Mol. Cell. Cardiol. 34*, 897-918.

157. James, P., Inui, M., Tada, M., Chiesi, M., and Carafoli, E. (1989) Nature and Site of Phospholamban Regulation of the Ca2+ Pump of Sarcoplasmic Reticulum. *Nature. 342*, 90-92.

158. Simmerman, H. K., Collins, J. H., Theibert, J. L., Wegener, A. D., and Jones, L. R. (1986) Sequence Analysis of Phospholamban. Identification of Phosphorylation Sites and Two Major Structural Domains. *J. Biol. Chem. 261*, 13333-13341.

159. Hagemann, D., and Xiao, R. P. (2002) Dual Site Phospholamban Phosphorylation and its Physiological Relevance in the Heart. *Trends Cardiovasc. Med. 12*, 51-56.

160. Mattiazzi, A., Mundina-Weilenmann, C., Vittone, L., Said, M., and Kranias, E. G. (2006) The Importance of the Thr17 Residue of Phospholamban as a Phosphorylation Site Under Physiological and Pathological Conditions. *Braz. J. Med. Biol. Res. 39*, 563-572.

161. Schmidt, A. G., Edes, I., and Kranias, E. G. (2001) Phospholamban: A Promising Therapeutic Target in Heart Failure? *Cardiovasc. Drugs Ther. 15*, 387-396.

162. Asahi, M., Kimura, Y., Kurzydlowski, K., Tada, M., and MacLennan, D. H. (1999) Transmembrane Helix M6 in Sarco(Endo)Plasmic Reticulum Ca(2+)-ATPase Forms a Functional Interaction Site with Phospholamban. Evidence for Physical Interactions at Other Sites. *J. Biol. Chem. 274*, 32855-32862.

163. Delaglio, F., Grzesiek, S., Vuister, G. W., Zhu, G., Pfeifer, J., and Bax, A. (1995) NMRPipe: A Multidimensional Spectral Processing System Based on UNIX Pipes. *J. Biomol. NMR. 6*, 277-293.

164. Johnson, B. A. (2004) *Using NMRView to Visualize and Analyze the NMR Spectra of Macromolecules.*

165. Casella, G. (2002) *Statistical Inference.* Pacific Grove, CA : Duxbury Thomson Learning, Pacific Grove, CA.

166. Karim, C. B., Zhang, Z., and Thomas, D. D. (2007) Synthesis of TOAC Spin-Labeled Proteins and Reconstitution in Lipid Membranes. *Nat. Protoc. 2*, 42-49.

167. Reddy, L. G., Cornea, R. L., Winters, D. L., McKenna, E., and Thomas, D. D. (2003) Defining the Molecular Components of Calcium Transport Regulation in a Reconstituted Membrane System. *Biochemistry. 42*, 4585-4592.

168. Cornea, R. L., Jones, L. R., Autry, J. M., and Thomas, D. D. (1997) Mutation and Phosphorylation Change the Oligomeric Structure of Phospholamban in Lipid Bilayers. *Biochemistry. 36*, 2960-2967.

169. Meiler, J., and Baker, D. (2003) Coupled Prediction of Protein Secondary and Tertiary Structure. *PNAS. 100*, 12105-12110.

170. Palmer, A. 3., Kroenke, C., and Loria, J. (2001) *Nuclear Magnetic Resonance Methods for Quantifying Microsecond-to-Millisecond Motions in Biological Macromolecules.*

171. Li, J., Boschek, C. B., Xiong, Y., Sacksteder, C. A., Squier, T. C., and Bigelow, D. J. (2005) Essential Role for Pro21 in Phospholamban for Optimal Inhibition of the Ca-ATPase. *Biochemistry. 44*, 16181-16191.

172. Chien, K. R. (2006) Beyond Small Molecule Drugs for Heart Failure: Prospects for Gene Therapy. *Novartis Foundation symposium JID - 9807767. 274*, 259.

173. Ha, K. N., Masterson, L. R., Hou, Z., Verardi, R., Walsh, N., Veglia, G., and Robia, S. L. (2011) Lethal Arg9Cys Phospholamban Mutation Hinders Ca2+-ATPase Regulation and Phosphorylation by Protein Kinase A. *Proc. Natl. Acad. Sci. U. S. A. 108*, 2735-2740.

174. Jefferies, J. L., and Towbin, J. A. (2010) Dilated Cardiomyopathy. *Lancet. 375*, 752-762.

175. Dellefave, L., and McNally, E. M. (2010) The Genetics of Dilated Cardiomyopathy. *Curr. Opin. Cardiol.*

176. Alves, M. L., Gaffin, R. D., and Wolska, B. M. (2010) Rescue of Familial Cardiomyopathies by Modifications at the Level of Sarcomere and Ca2+ Fluxes. *J. Mol. Cell. Cardiol. 48*, 834-842.

177. Bers, D. M. (2007) Calcium Cycling and Signaling in Cardiac Myocytes. *Annu. Rev. Physiol.*

178. Hill, T. L., and Inesi, G. (1982) Equilibrium Cooperative Binding of Calcium and Protons by Sarcoplasmic Reticulum ATPase. *Proc. Natl. Acad. Sci. U. S. A. 79*, 3978-3982.

179. Zhao, W., Uehara, Y., Chu, G., Song, Q., Qian, J., Young, K., and Kranias, E. G. (2004) Threonine-17 Phosphorylation of Phospholamban: A Key Determinant of Frequency-Dependent Increase of Cardiac Contractility. *J. Mol. Cell. Cardiol. 37*, 607-612.

180. Abu-Baker, S., Lu, J. X., Chu, S., Shetty, K. K., Gor'kov, P. L., and Lorigan, G. A. (2007) The Structural Topology of Wild-Type Phospholamban in Oriented Lipid Bilayers using 15N Solid-State NMR Spectroscopy. *Protein Sci. 16*, 2345-2349.

181. Gramolini, A. O., Kislinger, T., Alikhani-Koopaei, R., Fong, V., Thompson, N. J., Isserlin, R., Sharma, P., Oudit, G. Y., Trivieri, M. G., Fagan, A., Kannan, A., Higgins, D. G., Huedig, H., Hess, G., Arab, S., Seidman, J. G., Seidman, C. E., Frey, B., Perry, M., Backx, P. H., Liu, P. P., MacLennan, D. H., and Emili, A. (2008) Comparative Proteomics Profiling of a Phospholamban Mutant Mouse Model of Dilated Cardiomyopathy Reveals Progressive Intracellular Stress Responses. *Mol. Cell. Proteomics. 7*, 519-533.

182. Schmitt, J. P., Ahmad, F., Lorenz, K., Hein, L., Schulz, S., Asahi, M., Maclennan, D. H., Seidman, C. E., Seidman, J. G., and Lohse, M. J. (2009) Alterations of Phospholamban Function can Exhibit Cardiotoxic Effects Independent of Excessive Sarcoplasmic Reticulum Ca2+-ATPase Inhibition. *Circulation. 119*, 436-444.

183. Zima, A. V., and Blatter, L. A. (2006) Redox Regulation of Cardiac Calcium Channels and Transporters. *Cardiovasc. Res. 71*, 310-321.

184. Bigelow, D. J., and Squier, T. C. (2005) Redox Modulation of Cellular Signaling and Metabolism through Reversible Oxidation of Methionine Sensors in Calcium Regulatory Proteins. *Biochim. Biophys. Acta. 1703*, 121-134.

185. Karim, C. B., Marquardt, C. G., Stamm, J. D., Barany, G., and Thomas, D. D. (2000) Synthetic Null-Cysteine Phospholamban Analogue and the Corresponding Transmembrane Domain Inhibit the Ca-ATPase. *Biochemistry. 39*, 10892-10897.

186. Boraso, A., and Williams, A. J. (1994) Modification of the Gating of the Cardiac Sarcoplasmic Reticulum Ca(2+)-Release Channel by H2O2 and Dithiothreitol. *Am. J. Physiol. 267*, H1010-6.

187. Sahin, A. S., Gormus, N., and Duman, A. (2007) Preconditioning with Levosimendan Prevents Contractile Dysfunction due to H2O2-Induced Oxidative Stress in Human Myocardium. *J. Cardiovasc. Pharmacol. 50*, 419-423.

188. Cook, P. F. (1982) Kinetic Studies to Determine the Mechanism of Regulation of Bovine Liver Glutamate Dehydrogenase by Nucleotide Effectors. *Biochemistry. 21*, 113-116.

189. Szmigielski, A., Guidotti, A., and Costa, E. (1977) Endogenous Protein Kinase Inhibitors. Purification, Characterization, and Distribution in Different Tissues. *J. Biol. Chem. 252*, 3848-3853.

190. Yonemoto, W. M., McGlone, M. L., Slice, L. W., and Taylor, S. S. (1991) Prokaryotic Expression of Catalytic Subunit of Adenosine Cyclic Monophosphate-Dependent Protein Kinase. *Methods Enzymol. 200*, 581-596.

191. Froehlich, J. P., Mahaney, J. E., Keceli, G., Pavlos, C. M., Goldstein, R., Redwood, A. J., Sumbilla, C., Lee, D. I., Tocchetti, C. G., Kass, D. A., Paolocci, N., and Toscano, J. P. (2008) Phospholamban Thiols Play a Central Role in Activation of the Cardiac Muscle Sarcoplasmic Reticulum Calcium Pump by Nitroxyl. *Biochemistry. 47*, 13150-13152.

192. Hou, Z., Kelly, E. M., and Robia, S. L. (2008) Phosphomimetic Mutations Increase Phospholamban Oligomerization and Alter the Structure of its Regulatory Complex. *J. Biol. Chem. 283*, 28996-29003.

193. Kelly, E. M., Hou, Z., Bossuyt, J., Bers, D. M., and Robia, S. L. (2008) Phospholamban Oligomerization, Quaternary Structure, and Sarco(Endo)Plasmic Reticulum Calcium ATPase Binding Measured by Fluorescence Resonance Energy Transfer in Living Cells. *J. Biol. Chem. 283*, 12202-12211.

194. Chu, G., Li, L., Sato, Y., Harrer, J. M., Kadambi, V. J., Hoit, B. D., Bers, D. M., and Kranias, E. G. (1998) Pentameric Assembly of Phospholamban Facilitates Inhibition of Cardiac Function in Vivo. *J. Biol. Chem. 273*, 33674-33680.

195. Choudhary, G., and Dudley, S. C.,Jr. (2002) Heart Failure, Oxidative Stress, and Ion Channel Modulation. *Congest Heart Fail. 8*, 148-155.

196. Randhawa, A. K., and Singal, P. K. (1992) Pressure Overload-Induced Cardiac Hypertrophy with and without Dilation. *J. Am. Coll. Cardiol. 20*, 1569-1575.

197. Zhang, G. X., Kimura, S., Nishiyama, A., Shokoji, T., Rahman, M., Yao, L., Nagai, Y., Fujisawa, Y., Miyatake, A., and Abe, Y. (2005) Cardiac Oxidative Stress in Acute and Chronic Isoproterenol-Infused Rats. *Cardiovasc. Res. 65*, 230-238.

198. Luo, W., Grupp, I. L., Harrer, J., Ponniah, S., Grupp, G., Duffy, J. J., Doetschman, T., and Kranias, E. G. (1994) Targeted Ablation of the Phospholamban Gene is Associated with Markedly Enhanced Myocardial Contractility and Loss of Beta-Agonist Stimulation. *Circ. Res. 75*, 401-409.

199. Glaves, J. P., Trieber, C. A., Ceholski, D. K., Stokes, D. L., and Young, H. S. (2010) Phosphorylation and Mutation of Phospholamban Alter Physical Interactions with the Sarcoplasmic Reticulum Calcium Pump. *J. Mol. Biol.*

200. Masterson, L. R., Mascioni, A., Traaseth, N. J., Taylor, S. S., and Veglia, G. (2008) Allosteric Cooperativity in Protein Kinase A. *Proc. Natl. Acad. Sci. U. S. A. 105*, 506-511.

201. Abramoff, M. D., Magelhaes, P. J., and Ram, S. J. (2004) Image Processing with ImageJ. *Biophotonics International. 11*, 36-42.

202. Habeeb, A. F. S. A. (1972) Reaction of Protein Sulfhydryl Groups with Ellman's Reagent. *Methods in Enzymology. 25*, 457-464.

203. Le, M., and Means, G. E. (1995) A Procedure for the Determination of Monothiols in the Presence of Dithiothreitol--an Improved Assay for the Reduction of Disulfides. *Anal. Biochem. 229*, 264-271.

204. Zal, T., and Gascoigne, N. R. (2004) Photobleaching-Corrected FRET Efficiency Imaging of Live Cells. *Biophys. J. 86*, 3923-3939.

205. Förster, T. (1948) Zwischenmolekulare Energiewanderung Und Fluoreszenz. *Annalen der Physik. 437*, 55-75.

206. Patterson, G. H., Piston, D. W., and Barisas, B. G. (2000) Forster Distances between Green Fluorescent Protein Pairs. *Anal. Biochem. 284*, 438-440.

207. Rizzo, M. A., Springer, G., Segawa, K., Zipfel, W. R., and Piston, D. W. (2006) Optimization of Pairings and Detection Conditions for Measurement of FRET between Cyan and Yellow Fluorescent Proteins. *Microsc. Microanal. 12*, 238-254.

208. Palmer, A. G.,3rd, and Massi, F. (2006) Characterization of the Dynamics of Biomacromolecules using Rotating-Frame Spin Relaxation NMR Spectroscopy. *Chem. Rev. 106*, 1700-1719.

209. Shanmugam, M., Gao, S., Hong, C., Fefelova, N., Nowycky, M. C., Xie, L. H., Periasamy, M., and Babu, G. J. (2011) Ablation of Phospholamban and Sarcolipin Results in Cardiac Hypertrophy and Decreased Cardiac Contractility. *Cardiovasc. Res. 89*, 353-361.